The first Hi-GAL observations of the outer Galaxy: a look to star formation in the third Galactic quadrant in the longitude range $216.5^\circ \leq \ell \leq 225.5^\circ$

D. Elia[1], S. Molinari[1], Y. Fukui[2], E. Schisano[3,1], L. Olmi[4,5], M. Veneziani[3], T. Hayakawa[2], M. Pestalozzi[1], N. Schneider[6], M. Benedettini[1], A. M. Di Giorgio[1], D. Ikhenaode[7], A. Mizuno[8], T. Onishi[9], S. Pezzuto[1], L. Piazzo[6], D. Polychroni[10], K. L. J. Rygl[1], H. Yamamoto[2], Y. Maruccia[11]

davide.elia@iaps.inaf.it

ABSTRACT

We present the first Herschel PACS and SPIRE photometric observations in a portion of the outer Galaxy ($216.5^\circ \lesssim \ell \lesssim 225.5^\circ$ and $-2^\circ \lesssim b \lesssim 0^\circ$) as a part of the Hi-GAL survey. The maps between 70 and 500 μm, the derived column density and temperature maps, and the compact source catalog are presented. NANTEN CO(1-0) line observations are used to derive cloud kinematics and distances, so that we can estimate distance-dependent physical parameters of the compact sources (cores and clumps) having a reliable spectral energy distribution, that we separate in 255 proto-stellar and 688 starless. Both typologies are found in association with all the distance components observed in the field, up to $\sim$ 5.8 kpc, testifying the presence of star formation beyond the Perseus arm at these longitudes. Selecting the starless gravitationally bound sources we identify 590 pre-stellar candidates. Several sources of both proto- and pre-stellar nature are found to exceed the minimum requirement for being compatible with massive star formation, based on the mass-radius relation. For the pre-stellar sources belonging to the Local arm ($d \lesssim 1.5$ kpc) we study the mass function, whose high-mass end shows a power-law $N(\log M) \propto M^{-1.0\pm0.2}$. Finally, we use a luminosity vs mass diagram to infer the evolutionary status of the sources, finding that most of the proto-stellar are in the early accretion phase (with some cases compatible with a Class I stage), while for pre-stellar sources, in general, accretion has not started yet.

Subject headings: Galaxy: structure — ISM: clouds — ISM: molecules — Infrared: ISM — Stars: formation

[1]Istituto di Astrofisica e Planetologia Spaziali - INAF, Via Fosso del Cavaliere 100, I-00133 Roma, Italy

[2]Department of Physics, Nagoya University, Furo-cho, Chikusa-ku, Nagoya 464-8602, Japan

[3]Infrared Processing and Analysis Center, California Institute of Technology, Pasadena, CA, 91125, USA

[4]Osservatorio Astrofisico di Arcetri - INAF, Largo E. Fermi 5, 50125 Firenze, Italy

[5]University of Puerto Rico, Rio Piedras Campus, Physics Dept., Box 23343, UPR station, San Juan, Puerto Rico, USA

[6]IRFU/SAp CEA/DSM, Laboratoire AIM CNRS, Universit Paris Diderot, F-91191 Gif-sur-Yvette, France

[7]DIET Dipertimento di Ingegneria dell'Informazione, Elettronica e Telecomunicazioni, Università di Roma La Sapienza, via Eudossina 18, 00184 Roma, Italy

[8]Solar-Terrestrial Environment Laboratory, Nagoya University, Furo-cho, Chikusa-ku, Nagoya 464-8601, Japan

[9]Department of Physical Science, Osaka Prefecture University, Sakai, Osaka 599-8531, Japan

[10]University of Athens, Department of Astrophysics, Astronomy and Mechanics, Faculty of Physics, Panepistimiopolis, 15784 Zografos,Athens, Greece

[11]Dipartimento di Matematica e Fisica - Università del Salento, CP 193, 73100, Lecce, Italy

1. Introduction

Looking at star formation across the Milky Way, a large variety of different conditions is encountered, in many cases leading to observed different modalities. One of the most relevant differences is found in the amount of star formation activity between the inner and the outer Galaxy. The smaller content of star formation in the outer Galaxy is mainly related to the lower density of atomic and molecular hydrogen compared with inner Galaxy (Wouterloot et al. 1990).

Nevertheless the outer Galaxy offers the chance to study the interstellar clouds and possible ongoing processes of star formation with a lower degree of confusion, also close to the Galactic plane. Furthermore, reconstructing the structure of the velocity field from line observations is easier in this case, compared to the inner Galaxy, thanks to the lack of distance ambiguities at any observed radial velocity.

In this paper we present the first photometric study of a portion of the outer Galaxy surveyed by the Herschel Space Observatory (Pilbratt et al. 2010) as part of the Hi-GAL key-project (Molinari et al. 2010b), selecting a range of longitudes ($216.5^\circ \lesssim \ell \lesssim 225.5^\circ$) in the third Galactic quadrant (hereafter TGQ), covered also by a CO(1-0) line map obtained with the NANTEN radiotelescope. This combination of FIR/sub-mm dust continuum maps at unprecedented resolution and sensitivity and the information about kinematics provided by the line observations allow us to investigate the first stages of the star formation in this portion of the Milky Way, by estimating and discussing in statistical sense the physical properties of the compact sources (cores and clumps) detected in the Herschel maps. With this analysis we aim at shedding more light on the star formation in the TGQ, to which a relatively little amount of literature has been devoted so far.

The first extensive surveys of the the TGQ were carried out by May et al. (1988, 1993), at an angular resolution of 0.5° and $8'.8$, respectively. They confirmed the warping of the disk at these longitudes (Burton & te Lintel Hekkert 1986) and the presence of weak emission from molecular cloud located at Galactocentric distances larger than $R = 12$ kpc. The latter survey was then drawn on by May et al. (1997) to derive the properties of the clouds located beyond 2 kpc from the Sun. A relevant finding of this analysis is that no grand design spiral pattern is seen in the distribution of the clouds on the Galactic disk. The warp of the Galaxy in the TGQ has been observed also by Wouterloot et al. (1990) and Dobashi et al. (2005) through the distribution of the IRAS sources and of the visual extinction maps derived from the Digitized Sky Survey I, respectively.

To assess the spiral structure of the Galaxy in the TGQ other techniques have been also adopted. Carraro et al. (2005) and Moitinho et al. (2006) have studied the distribution of young star clusters, tracing the Local, the Perseus and the Norma-Cygnus (Outer) arms. This latter is not detected at these longitudes by Nakanishi & Sofue (2006) based on the Dame et al. (2001) CO survey (which is taken, for most of the TGQ, from that of May et al. 1993). Instead, the Moitinho et al. (2006) results were confirmed by Vázquez et al. (2008), who attribute to the Outer arm a grand design feature extending from $\ell = 190^\circ$ to 255° (reaching heliocentric distances $d = 6$ and 12 kpc at the two extreme longitudes, respectively), expanding the sample of clusters of Moitinho et al. (2006) and combining this information with kinematics extracted from new CO observations (still unpublished at present).

Focusing on the vicinity of the region analyzed in this work, the most important star-forming region is CMa R1, dominated by the presence of the CMa OB1 association (Ruprecht 1966) located at $d = 1150$ pc, i.e. in the Local arm, and with an age of 3×10^6 yr (Clariá 1974) and of the Sh2-296 (S296 in the simplified notation we adopt hereafter) HII region (Sharpless 1959). The population of young stars in CMa R1 has been studied by Gregorio-Hetem et al. (2009) based on X-ray data, and its typical age has been estimated as older than 10^7 yr. However, only a very small fraction of the investigated proto-stars lie in the area surveyed in the present paper.

This area was fully covered, instead, by the survey of molecular clouds in the Monoceros and Canis Major regions carried out with the NANTEN telescope in the ^{13}CO(1-0) line (Kim et al. 2004), spanning an area of 560 square degrees. The two most massive giant molecular clouds found are the aforementioned CMa OB1 and G220.8-1.7

(Maddalena et al. 1986), this latter located at $d = 1050$ pc. These authors also studied the relation between the gas emission morphology and the star formation signatures have been observed in this region, as several IRAS young stellar object candidates and HII regions (Sharpless 1959; Blitz et al. 1982). The low level of extinction ($A_V < 3$) found by Dobashi et al. (2005) in the entire region, however, seems to exclude the possibility of encountering massive star formation (MSF hereafter, cf, e.g., Krumholz & McKee 2008). The western part of our survey corresponds, instead, to the north-eastern corner of G216-2.5 (or Maddalena's cloud, $d = 2200$ pc), mapped in both CO(1-0) and ^{13}CO(1-0) by Lee et al. (1994). These authors claim the non-star-forming nature for this cloud, partially controverted by more recent Spitzer observations of Megeath et al. (2009), while recognize the star forming character of a nearby filamentary cloud associated with the S287 HII region, fully covered by our observations.

In this framework, the new Hi-GAL observations in the crucial range $70 - 500$ μm will permit to obtain a more exhaustive description of the star forming activities or capabilities in this region. In particular, both the early stages of the protostellar core evolution and the properties of their pre-stellar progenitors can be studied, being in both cases the peak of the cold dust emission lying in this range of wavelengths (e.g., Molinari et al. 2010a; Elia et al. 2010).

Thanks to NANTEN CO(1-0) data, we are also able to estimate kinematic distances for those sources, needed to derive masses and luminosities and then to depict a possible evolutionary scenario for the region. This allows us to carry out a complete study of cold dust and gas properties at unprecedented resolution and sensitivity in a significant portion of the outer Galaxy.

This analysis is structured and presented as follows. In Section 2 the details about Herschel and NANTEN observations are reported, together with data reduction strategy. In Section 3, and also in Appendix A, the obtained maps are presented, and used to provide an overall description of the column density and temperature distributions in the surveyed area. Starting from Section 4 the discussion revolves about the compact sources that are extracted from the Hi-GAL maps and from the ancillary CO(1-0) observations through cloud decomposition techniques. In Section 5 the main properties of the Hi-GAL compact sources are derived from photometric data by means of a modified black body fit and then discussed in the framework of the differences between pre- and proto-stellar sources. In Section 6, in particular, these quantities are exploited to situate the Hi-GAL sources into an evolutionary picture. Finally, in Section 7 a summary of the obtained results is reported.

2. Observations and data reduction

2.1. Hi-GAL observations

The *Herschel Infrared Galactic plane survey* (Hi-GAL, Molinari et al. 2010b) is a Herschel open-time key-project that initially aimed at covering the inner Galaxy ($|\ell| < 60°, |b| < 1°$), and was subsequently extended to the entire Galactic disc.

In this paper we publish the first four "tiles" observed in the TGQ as part of this survey, spanning the range of Galactic longitudes $216.5° \lesssim \ell \lesssim 225.5°$ and the range of latitudes $-2° \lesssim b \lesssim 0°$, because in this portion of the Galactic plane the Hi-GAL observations do not straddle the latitude $b = 0°$, but follow the warped midplane.

The $2.3° \times 2.3°$ fields presented in this paper were observed between May 5 and 9, 2011. As in the case of all the Hi-GAL survey, the maps were obtained with the Herschel fast scan parallel mode, i.e., using simultaneously PACS at 70 and 160 μm (Griffin et al. 2010) and SPIRE at 250, 350, and 500 μm (Poglitsch et al. 2010) at the scan speed of $60''$/s, and performing two scan maps of each field, one with nominal coverage and the other with orthogonal coverage, in order to increase data redundancy. Due to the $21'$ separation of the PACS and SPIRE focal plane footprints on the sky, the areas covered by these two instruments result slightly different, namely shifted each other of this angular quantity. The diffraction limits at the five bands are 5.0, 11.4, 17.6, 23.9, and $35.1''$, respectively. However, due to the PACS onboard data averaging and the use of the fast speed mode a degradation of the PACS PSF is produced along the scan direction, up to 12.2 and $15.7''$at 70 and 160 μm, respectively (PACS manual, available from the ESA Herschel Science Centre). The Hi-GAL observation name convention consists in

naming the tiles using the approximated value of the central longitude, then in the following we will designate these four tiles as $\ell 217$ [1], $\ell 220$, $\ell 222$, $\ell 224$. Hereafter, we will call $\ell 217 - 224$ the entire region composed by these four tiles and analyzed in this paper.

The data reduction strategy followed the Hi-GAL pipeline described in Traficante et al. (2011). Briefly, we used scripts written in the Herschel interactive processing environment (HIPE, Ott 2010) to reduce archival data to the Level 1. The obtained time-ordered data (TODs) of each bolometer were then processed further by means of dedicated IDL routines to remove spurious instrumental effects and glitches due to cosmic rays, and maps were obtained using the FORTRAN code ROMAGAL based on Generalized Least Square (GLS: e.g., Tegmark 1997) approach, able to reduce the influence of the $1/f$ noise in the TODs. Since the GLS technique is known to introduce artifacts in the maps, namely crosses and stripes in correspondence of the brightest sources, a weighted post-processing of the GLS maps (WGLS, Piazzo et al. 2012) has been applied to finally obtain images in which artifacts are removed or heavily attenuated.

The pixel sizes of the maps are $3.2''$, $4.5''$, $6.0''$, $8.0''$, and $11.5''$at 70, 160, 250, 350, 500 μm, respectively. The astrometry of the maps has been checked comparing the positions of several compact sources in the 70 μm maps with those of their possible WISE (Wright et al. 2010) counterparts at 22 μm, and the calculated rigid offset applied for correction. Finally, the absolute calibration has been definitively performed by applying a linear transform of the maps adopting the coefficients determined by comparing Herschel with IRAS and Planck, following Bernard et al. (2010).

All the single tile images obtained at the five Hi-GAL wavelengths are reported in APPENDIX A. In Figure 1, instead, we show a composite RGB image of the region, assembled combining the mosaics of the four tiles at 160, 250 and 500 μm. The 70 μm observations have not been used because the diffuse emission they contain appears dominated by the noise and only the brightest regions are well recognizable. The mosaics have been produced in the same way as the single tiles, combining together the TODs of the four tiles to obtain an overall map. The common science area, i.e. the area covered by PACS and SPIRE, highlighted with a cyan contour in Figure 1, amounts to ~ 20.5 deg^2.

[1] In this case, the value $\ell = 218^\circ$ would be closer to the center of the map, but we use the conventional name already reported in the Herschel Data Archive.

2.2. NANTEN CO(1-0) observations

The NANTEN CO(J=1-0) Galactic Plane Survey data set (Mizuno & Fukui 2004) was used in the present analysis. At the time of the observations, carried out in a period from 1996 to 2003, 4-m NANTEN millimeter-wave telescope of Nagoya University was installed at Las Camapans Observatory in Chile. The half-power beamwidth was $2'.6$. The data were gathered using the position switching mode. The pointing accuracy was better than $20''$. The observations covered a region of $\sim 23^\circ$ (the coordinates of the bottom-left and top-right pixels are $[\ell, b] = [225.60^\circ, -2.53^\circ]$ and $[\ell, b] = [216.53^\circ, 0^\circ]$, respectively), and the observed grid consists of 136×38 points located every $4'$.

The spectrometer used was acousto-optical with 2048 channels providing a frequency resolution of 250 kHz. The spectral intensities were calibrated by employing the standard room-temperature chopper wheel technique (Kutner & Ulich 1981). An absolute intensity calibration was achieved by taking the absolute peak antenna temperature, $T_{\rm R}^*$, of Orion KL (R.A. = $5^h32^m47.^s0$, Dec. = $-5^\circ24'21''$ for the equinox of 1950.0) to be 65 K. The rms noise fluctuations were typically 0.2 K with about 5 seconds integration for an on-position. A first order degree polynomial was subtracted from the line spectra to account for instrumental baseline effects. Finally, antenna temperatures were divided by the main beam efficiency factor $\eta_{\rm mb} = 0.89$ (Ogawa et al. 1990) to obtain main beam temperatures.

The integrated intensity maps obtained from these line observations are presented in Section 3.1.

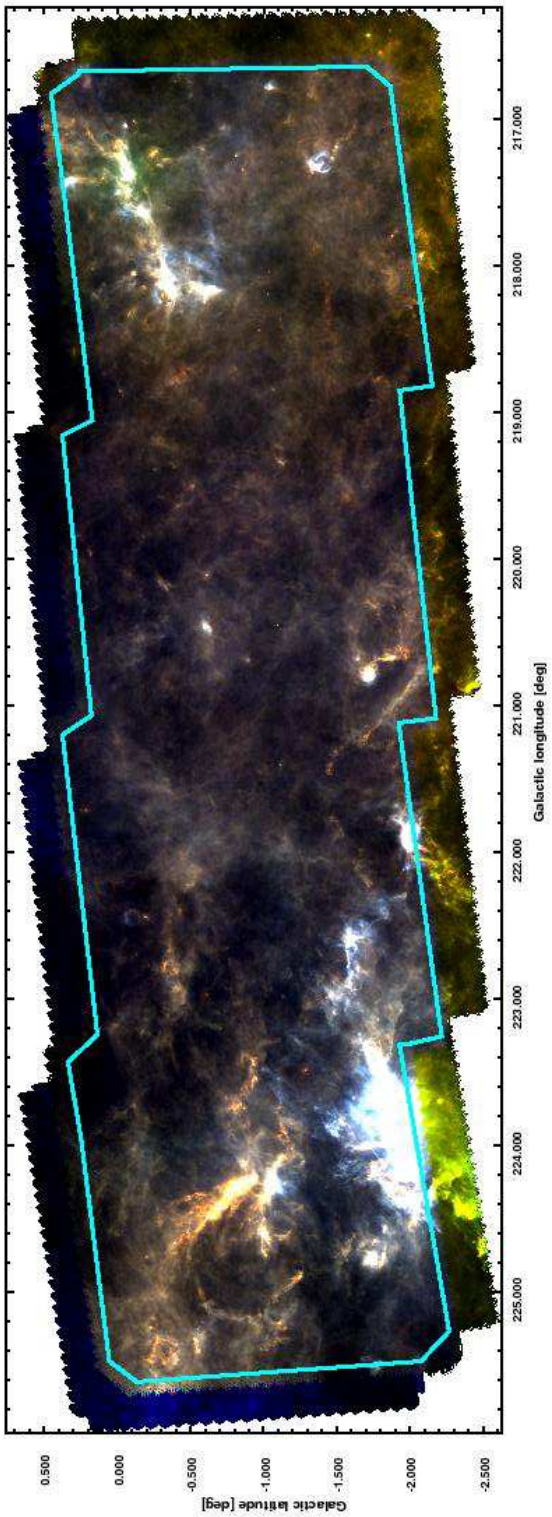

Fig. 1.— RGB composite of $\ell 217 - 224$ (blue: PACS 160 μm, green: SPIRE 250 μm, red: SPIRE 500 μm). The color scaling is linear. The cyan contour delimits the common science area covered by both PACS and SPIRE.

3. The overall distribution of gas and dust

3.1. ^{12}CO(1-0) line

A first look at the spectra in the reduced CO(1-0) data cube reveals that the structure of the velocity field is relatively clear due to the small number of spectral components detected and to the infrequent presence of more than one along the same line of sight.

A global view of the velocity field is provided in Figure 2 in which we show the sum of all the spectra composing the cube, where at least three main components are found, peaking at the 17, 28, and 40 km s^{-1} velocity channels, respectively. A secondary peak of the second component also appears around 33 km s^{-1}. Finally, a further weak component, the most red-shifted, is present around 54 km s^{-1}. These indications can be exploited to determine opportune velocity ranges $[v_0, v_1]$ to build meaningful channel maps, rather than blindly choosing equally spaced ranges of channels.

The maps have been obtained by integrating the line emission (main beam temperature) in those lines of sight where a feature with a signal-to-noise better than 3 has been found (the average baseline rms noise of the data cube is $\sigma_{\rm rms} = 0.23$ K:

$$I_{CO} = \int_{v_0}^{v_1} T^*_{\rm mb}\, dv \qquad (1)$$

In Figure 3 we show both the map of the ^{12}CO(1-0) intensity integrated over the whole range from -0.5 to 60.5 km K s^{-1} (panel *a*), and the set of the maps corresponding to the ranges highlighted in Figure 2 (panels *b*-*e*).

The first and the second velocity components (sorted from the bluest to the reddest) are evidently predominant in the total budget of the emission. To quantify this, in Table 1 the contribution of each component to the integrated intensity map in panel *a* is quoted, together with the average distance calculated at a characteristic longitude for each component. A gross estimate of the masses of these four components can be obtained, given the information on the global distance. First, the local column density map is derived directly from the maps in Figure 3 through the empirical relation

$$N(H_2)_{i,j} = X \times I_{CO\,i,j}\ , \qquad (2)$$

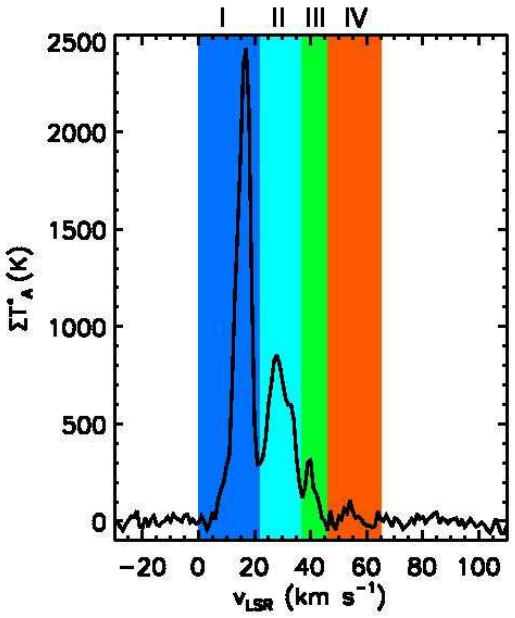

Fig. 2.— Sum of all the ^{12}CO(1-0) spectra. A rescaled *y*-axis is also reported on the right to give the equivalent interpretation as average spectrum. The four velocity ranges delimited by -0.5, 20.5, 36.5, 44.5, and 65.5 km s^{-1} are labelled with Roman numerals and highlighted with a blue, cyan, green and red background, respectively.

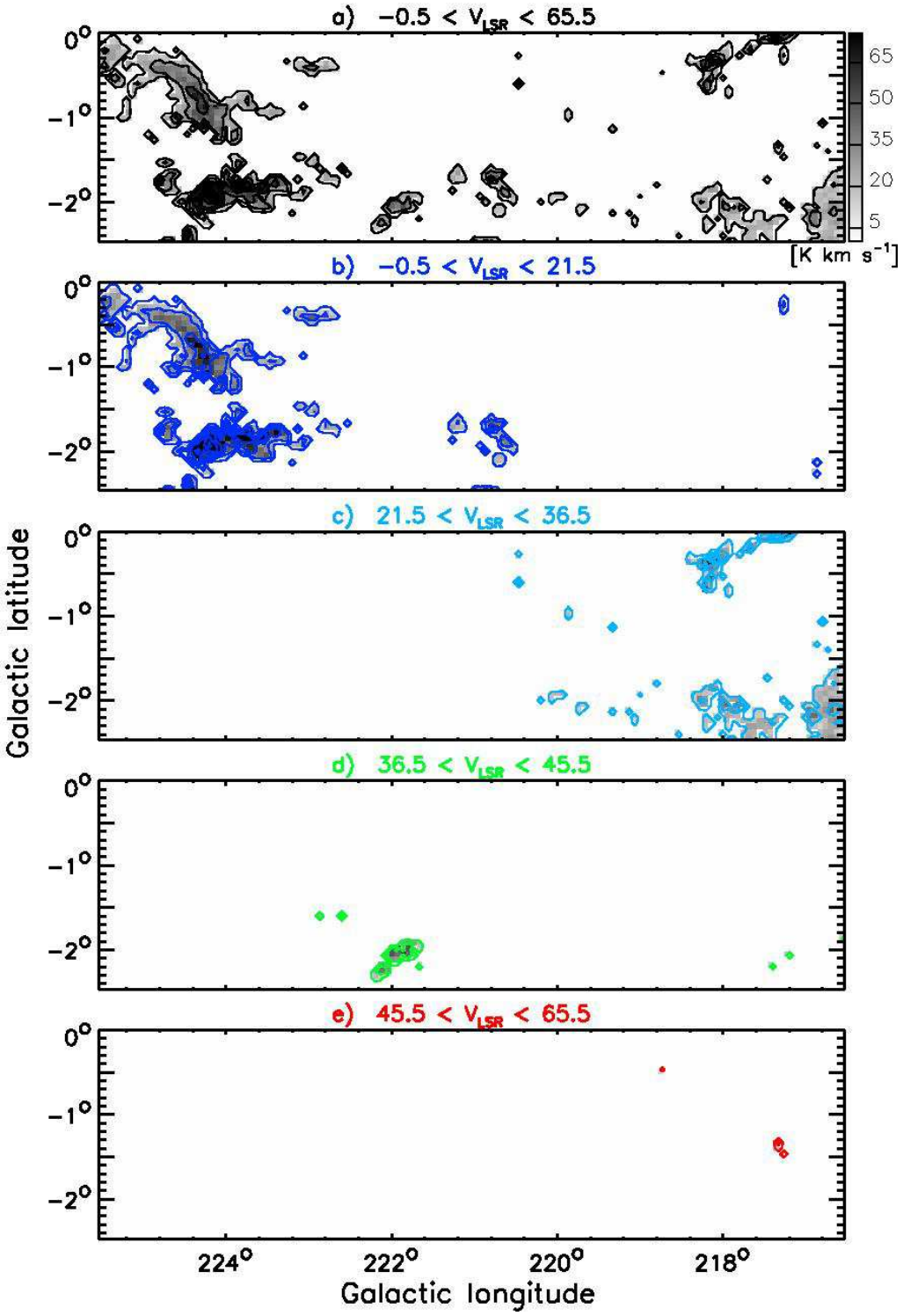

Fig. 3.— CO(1-0) integrated intensity maps of the $\ell 217-224$ region, in units of K km s^{-1}. The correction for the $\eta_{\rm mb}$ factor is taken into account. In panel *a*, the map obtained integrating over in the entire considered velocity range is shown, while panels *b*-*e* contain the intensity integrated over the ranges specified in the title of each panel. For all panels, contours start from 5 K km s^{-1} and are in steps of 15 K km s^{-1}.

TABLE 1
OVERALL PROPERTIES OF THE ^{12}CO(1-0) EMISSION IN ℓ217-224

Component	v_{peak} (km s^{-1})	v_0 (km s^{-1})	v_1 (km s^{-1})	Ref. longitude (deg)	Distance (kpc)	% of total emission	X $\times 10^{-20}$(cm^{-2} K^{-1} km^{-1} s)	Mass (10^5 M$_\odot$)
I	17	29.5	51.5	223	1.1	69.2	3.2	1.1
II	28	51.5	66.5	218	2.2	26.2	3.3	1.9
III	40	66.5	75.5	222	3.3	4.3	3.5	0.7
IV	54	75.5	94.5	217	5.8	0.4	4.0	0.2

where the conversion coefficient value adopted in this case is calculated as a function of the Galactocentric radius R through the relation of Nakanishi & Sofue (2006):

$$X[\mathrm{cm^{-2}\,K^{-1}\,km^{-1}\,s}] = 1.4 \times 10^{20} \exp(R/\ 11\mathrm{kpc})\ . \quad (3)$$

Then, for the each component the mass is obtained integrating the column density over the area occupied in the sky: $M = \sum_{i,j} N(H_2)_{i,j}\, d^2\, \Delta\vartheta^2\, \mu\, m_H$, where $\Delta\vartheta$ indicates the pixel scale of the CO(1-0) map (in radiants).

Nevertheless, the value of the X conversion coefficient is matter of debate and strong variations of the obtained mass values are expected if another estimate of X is adopted. For instance, Nakanishi & Sofue (2006) make a twofold analysis using both the approach described by the Equation 2 and the constant value $X = 1.8 \times 10^{20}$cm^{-2} K^{-1} km^{-1} s of Dame et al. (2001). In our case, this latter value would lead to underestimate of the masses Table 1 of a factor from 1.8 to 2.2, depending on the distance.

The overall distribution of the column density derived from these maps is presented in Section 3.2, while the correspondence with Hi-GAL maps and with previous CO(1-0) surveys is discussed in Section 3.3. Here we just highlight the low degree of complexity of the velocity field, as it emerges from these line observations. In Figure 4 the CO(1-0) contours of Figure 3, $b-e$, are overlapped on the SPIRE 250 μm mosaic. The degree of overlap among components appears relatively low: the eastern part of the region is dominated by the first (bluest) component, the western one is dominated by the second component, whereas the third and fourth component are basically associated to few small and bright features of the SPIRE map.

3.2. Herschel temperature and column density maps

Both the Herschel and NANTEN observations give the possibility of deriving maps of the column density in the region. Possible differences between the resulting maps are expected, due to the assumptions made on the considered component of the ISM. Therefore, any comparison requires care and must be accompanied with some caveats.

We obtained the maps of column density and temperature for $\ell 217-224$ from the mosaics of the four Hi-GAL tiles, using the wavelengths from 160 to 500 μm, being the emission at 70 μm generally contaminated by warmer dust components as circumstellar matter and HII regions (cf. Schneider et al. 2012). This implies, of course, that these maps basically represent the properties of the cold component of the dust (large grains). From the practical point of view, considering only the common science area, all the maps have been rebinned onto the grid of the 500 μm one, and a pixel-to-pixel grey-body fit has been performed, according to the usual expression

$$F_\nu = N(H_2)\, \mu\, m_H\ \Delta\vartheta^2_{500}\ k_0\ \left(\frac{\nu}{\nu_0}\right)^\beta\ B_\nu(T)\ , \quad (4)$$

where F_ν represents the spectral energy distribution (SED) of the pixel, $\Delta\vartheta_{500}$ is the map pixel scale at 500 μm in sr, $k_0 = 0.1$ cm^2 g^{-1} at $\nu_0 = 1200$ GHz ($\lambda_0 = 250$ μm) already accounting for a gast-to-dust ratio of 100 (Hildebrand 1983), m_H is the atomic hydrogen mass, and μ the mean molecular weight, assumed to be equal to 2.8 to take into account a relative helium abundance of 25% in mass. We imposed $\beta = 2$ in order to reduce the number of free parameters in the fit (see also Sadavoy et al. 2012).

The obtained column density and temperature

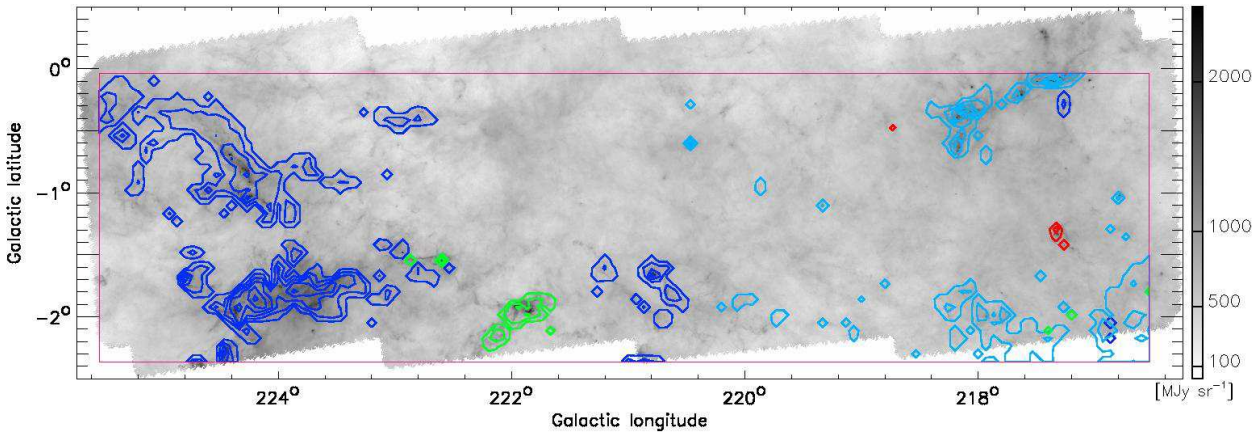

Fig. 4.— Structure of the velocity field in $\ell 217 - 224$. The contours of Figure 3, panels *b*-*e*, are overplotted, with the same color convention, on the the SPIRE 250 μm mosaic, while the magenta box represents the boundaries of the area surveyed in the CO(1-0) line. The dynamics of the SPIRE image has been compressed between 20 and 2500 MJy/sr, and the scale is logarithmic.

maps are shown in Figures 5 and 6. Combining the information contained in these maps and in that of Figure 4 with the global impression provided by Figure 1, we are now able to provide an overall description of the $\ell 217 - 224$ region.

The eastmost tile, namely $\ell 224$, is by far the richest in bright features and, apparently, in star formation activity. All these regions belong to the CMa OB1 giant molecular cloud, located at $d =$ 1150 pc (Kim et al. 2004, and references therein), and are encircled by the HII region S296 (Sharpless 1959), as illustrated in Figure 5.

A large cavity centered at about $[\ell, b] = [224.8°, -0.9°]$ is well recognizable, with a filamentary ridge that turns out to be particularly massive and cold ($11 \lesssim T \lesssim 13$ K) in the western part. Another bright filament aligned with the East-West direction seems to connect, in perspective, the center with the ridge of the cavity. This corresponds to the massive ($M = 1.2 \times 10^3 M_\odot$) cloud 4 of the paper of Kim et al. (2004) ([KKY2004]4 according to the SIMBAD nomenclature). The southern part of $\ell 224$ is dominated by another extended, bright and warmer region corresponding to S292 and [KKY2004]3; this latter is the most massive cloud ($M = 1.9 \times 10^3 M_\odot$) of those identified by Kim et al. (2004) in the area considered in this paper. Cold filaments coexist with warm ($T < 20$ K) diffuse emission or star forming sites, as S292. The young cluster NGC2335, located north of this region ($[\ell, b] = [223.62°, -1.26°]$) and with distance and age estimated in 1.79 pc and 79 Myr, respectively (Moitinho et al. 2006) is not detected at any of the Herschel wavelengths.

In the $\ell 222$ tile another small cloud is found, [KKY2004]1, still belonging to CMa OB1. In the southern part, the BFS64 HII region (Blitz et al. 1982) is associated with the velocity component III. The emission in $\ell 220$, again, is mostly associated with the velocity component I. Two HII regions, BFS61 and BFS62, represent the signature of recent high-mass star formation activity, albeit much less dramatic than in $\ell 224$.

In $\ell 217$ a filamentary cloud already mentioned in Section 1 is prominent in the northern part. It belongs to the velocity component II and is associated with the S287 HII region and other minor ones, and with four molecular clouds of Kim et al. (2004). The angular size of the whole filament is approximately 1.6°, corresponding to an extent of 59 pc at a distance of $d = 2.1$ kpc. It is considered an active site of star formation by Lee et al. (1994), who justify its filamentary shape with the action of stellar winds of the O-B stars driving the HII regions. A peak of dust temperature at $T = 25.8$ K is found right by the position of

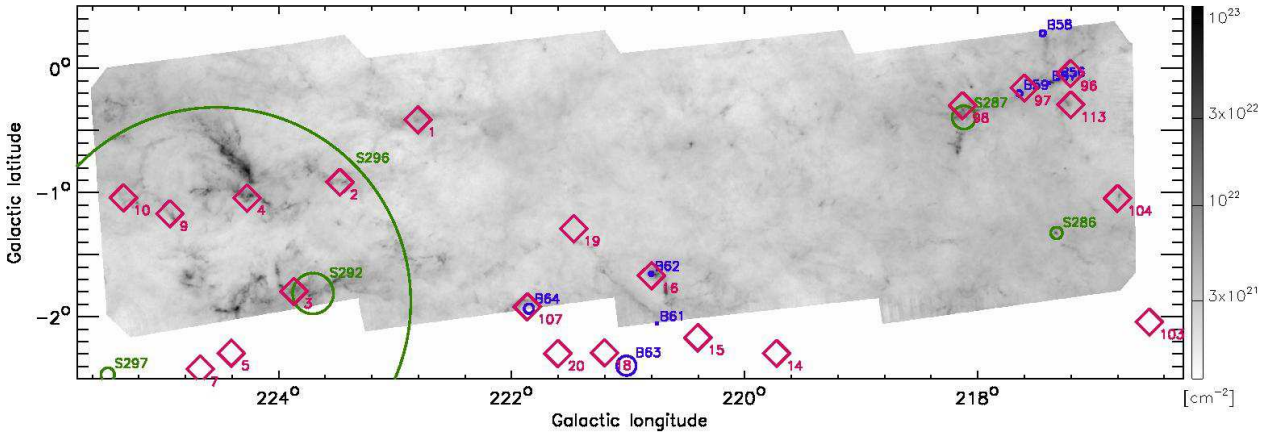

Fig. 5.— Column density map of $\ell 217 - 224$ in cm^{-2}, determined using the 160, 250, 350, 500 μm Herschel bands. The displacement of HII regions is also shown: green circles are from Sharpless (1959), blue circles from Blitz et al. (1982), respectively. The object names, labeled at the top right of each region have been shortened to avoid confusion in the figure (only those of BFS56 and BFS57 are partially overlapped in the North-West part of the map). Finally, the molecular clouds of Kim et al. (2004) are overlapped as magenta diamonds, simply labeled with their running number at the bottom-right.

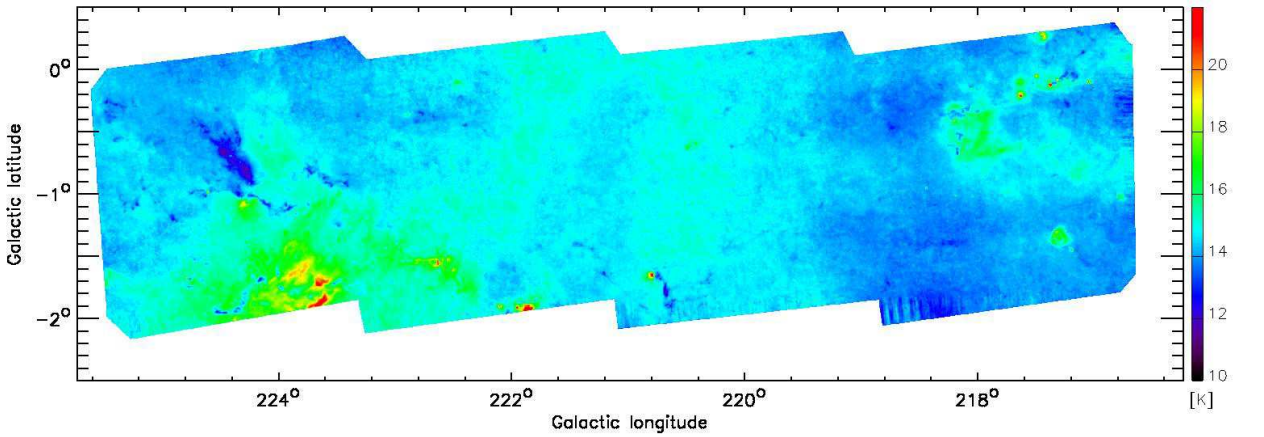

Fig. 6.— Temperature map of $\ell 217 - 224$, determined using the 160, 250, 350, 500 μm Herschel bands.

the BFS57 HII region. The L1649 cloud (Lynds 1962), indicated as [KKY2004]113, is well visible below the filament, but physically unrelated with it, being instead the only prominent feature of the velocity component I in the $\ell 217$ field. Finally, two dense and relatively compact regions are seen in the South. The first one corresponds to S286 and belongs to the velocity component IV (d = 5.3 kpc, R = 10.0 kpc), representing the farthest unconfused region detected in this portion of the Hi-GAL survey; in the dust temperature map it appears warmer ($15 \lesssim T \lesssim 19$ K) than the portion of sky it is projected on. The second one (also IRAS06522-0350) is quoted as a satellite star-forming cloud (Megeath et al. 2009) of the G216-2.5 cloud (Lee et al. 1994).

As a global remark, we notice that, invoking the theoretical result of Krumholz & McKee (2008) about a column density threshold for having massive star formation (MSF hereafter), namely $\Sigma = 1$ g cm^{-2} which assuming a mean molecular mass of 2.8 corresponds to $N(\mathrm{H_2}) = 2.1 \times 10^{23}$ cm^{-2}, there are no pixels exceeding this value in our column density map. However, this result cannot be considered resolutive against the presence of MSF in $\ell 217 - 224$, for at least three main reasons: *i*) mainly for distant components, possible column density peaks might be diluted in the solid angle subtended by a pixel, because of the original instrumental angular resolution and/or the subsequent regridding of the maps for calculating the column density; *ii*) these column densities and temperatures are derived using the total emission measured along the whole line of sight; however, as it is described below in the paper, if the compact source emission is separated from the background, lower temperatures and higher masses are found for those cores, making it possible to find higher values of the column density; *iii*) as shown by Kauffmann & Pillai (2010), and also suggested by Hi-GAL observations (Elia et al. 2010), the Krumholz & McKee (2008) critical value probably constitutes a too severe threshold for MSF; this point will be further discussed in Section 5.5.

3.3. Comparison of the two techniques

The availability of both the CO(1-0) and Herschel column density estimates allow us to compare the performance of an optically thick spectral line and of the dust as density tracers of the clouds, and to check the validity of the empirical relation 2 in this portion of the Galactic plane. We consider the Herschel-based map (Figure 5) the most reliable of the two, being the cold dust a truly optically thin tracer of the ISM density. Instead, the empirical CO-based method may fail in single cases, mainly in the densest parts of the clouds, as recently further demonstrated by Shetty et al. (2011) by means of radiative transfer models. Also, it is sensitive to the excitation conditions of the gas. A systematic characterization of these factors affecting the CO-derived column densities will be reported in the forthcoming paper of Carlhoff et al. (submitted).

In Figure 7, panel *a*, the histogram of this map is reported. It is characterized by a peak well described by a log-normal behavior (the log-normal fit is also shown), followed by a power-law-like extension at higher column densities. This situation is commonly found in regions forming low mass (Kainulainen et al. 2011) and high mass (Hill et al. 2011; Schneider et al. 2012) stars, being the log-normal shape attributed to turbulence, and the deviation at large densities due to strongly self-gravitating systems, a typical signature of star formation activity (e.g., Klessen 2000; Federrath et al. 2008). A more quantitative analysis of the power-law tail of this requires separating the different components along the line of sight. however, this is beyond the scope of this present paper and will be presented in another study focusing on the probability density functions.

The CO-based column density has been derived for the four distance components through the Equation 2, adopting the corresponding X factor values reported in Table 1; subsequently, these four maps have been co-added to obtain the total column density map. To better compare the two maps, we considered only the portion corresponding to the common coverage area (Figure 7, panel *b*, green dotted line), and then reprojected the Herschel-based map onto the grid of the CO(1-0) map, considering only the pixels with meaningful values in both maps (zeroes can be found, especially in the CO-based map). The histograms obtained in this way (Figure 7, panel *b*, solid lines) become directly comparable, being derived from the same amounts of pixels.

It is possible to appreciate that the histogram of the CO-based column density appears quite

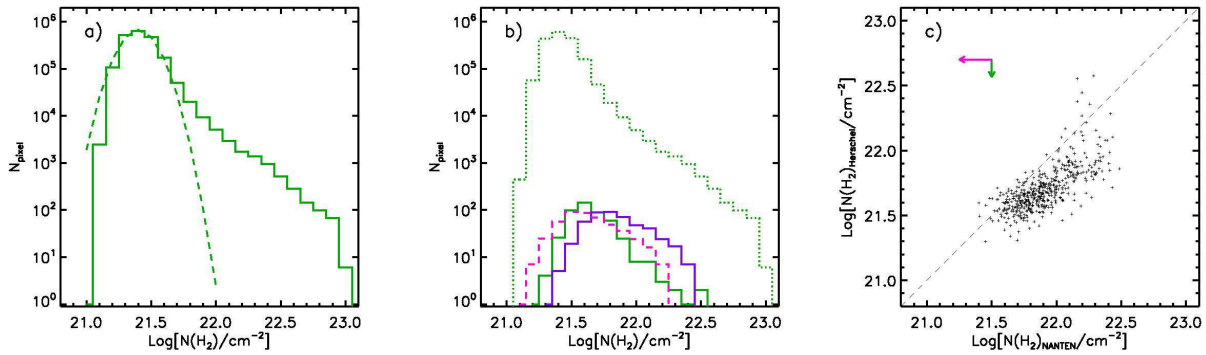

Fig. 7.— Comparison between the Herschel- and CO-based column densities. Panel *a*: Pixel distribution of the original Herschel-based map. The green dashed curve represents the log-normal fit to the Herschel histogram. Panel *b*: The green dotted histogram is calculated as in panel *a*, but considering only the pixels belonging to the area also covered by the CO(1-0) map. The green solid histogram is the pixel distribution of the Herschel-based column density map once reprojected on the CO map grid. The purple solid histogram is the distribution of the pixels of CO-based column density map belonging to the common coverage area. The magenta dashed histogram is the same distribution as the previous one, but calculated using the X coefficient of (Dame et al. 2001). Panel *c*: Pixel-to-pixel plot of the values composing the dotted histograms of panel *a*. The dashed line represents the 1:1 relation. The green and magenta arrows represent the shift to be applied to the plotted points if different k_0 and X coefficients are employed to compute the column density from the Herschel and the CO maps, respectively (see text). The x axes of all panels and the y axis of the panel *c* are the same for comparison.

different from those both the original Herschel-based map and its regridded version. In the first case, the largest values CO-based density values are more than half order of magnitude lower than those revealed in the Herschel-based map. This can be due to the combination of different concomitant effects. First, the CO(1-0) is not ideal tracer of the high-density gas distribution. This mainly affects the histogram shape, as a lack of the tail that, for instance, we observe in the Herschel-based one (e.g., Shetty et al. 2011). Second, the The significant pixel size difference between the SPIRE and NANTEN beams ($11.5''$ against $4'$) produces in the latter case a much higher degree of dilution of the local bright peaks in the final pixels, removing from the histogram the high-density tail that is seen instead in the former. This effect can be assessed by considering the histogram of the reprojected Herschel-based map: in this case the two histograms have a more similar peak position and ranges of variability. However, the regridding of the Herschel-based column density map produces a strong attenuation of both the low- and the high-density tail of its histogram, where now the CO-based one appears to be more populated. This can be seen also in the plot of the Herschel-based column density (reprojected) vs the CO-based one, built pixel-to-pixel and shown Figure 7, panel *c*. In the majority of cases ($\sim 92\%$) the former is smaller than the latter and, the ratio of the sums of the involved pixels is ~ 0.6. This is just a global indication that cannot be simply taken as a sort of further correction of the adopted X factors, since the relation between the two distributions does not appear linear. The X factor is also known to depend strongly on local variations of the physical conditions, because it is expected to be lower in zones of star formation activity (Pineda et al. 2008). Furthermore, the CO line intensity depends on the temperature of the gas. However, we can at least evaluate how the choice of the X factor might affect the conclusions achievable by the comparison of the two column density maps. Adopting $X = 1.8 \times 10^{20} \mathrm{cm}^{-2}\,\mathrm{K}^{-1}\,\mathrm{km}^{-1}\,\mathrm{s}$ (Dame et al. 2001, see Section 3.1), the original CO map histogram is shifted towards lower densities, and its shape gets sligthly modified because of different coefficients initially adopted for the components

I-IV (magenta dashed histogram in panel b). In this case, the distribution peaks at a value smaller than that of the Herschel-based one. On the other hand, a different choice of the k_0 constant in the Equation would produce a rigid shift of the Herschel-based column density histogram. For example, the constant of Preibisch et al. (1993) ($k_0 = 0.005$ cm^2 g^{-1} at 230 GHz) can be translated, for $\beta = 2$ as in our case, to 0.14 cm^2 g^{-1} at 1200 GHz, producing 40% lower column densities. These possible corrections are represented in panel c as arrows, showing that the choice of a smaller X coefficient would generally produce a better agreement between the two distributions, while a larger dust opacity would obtain the opposite effect.

4. Cores and clumps

In this section we start to focus on the distribution and the properties of the compact sources detected in the Hi-GAL observations of $\ell 217-224$. The distance estimate for these sources is performed exploiting the kinematic distances of CO clumps.

4.1. Photometry of Herschel compact sources

The compact source detection and photometry have been performed at each of the five available bands following the procedure described in previous Hi-GAL articles (Molinari et al. 2010a; Elia et al. 2010). We used the Curvature Threshold Extractor package (CuTEx, Molinari et al. 2011), which detects the sources as local maxima in the second-derivative images and then fits an elliptical Gaussian to the source brightness profile to estimate the integrated flux of the source. The parameters of the best fit (the peak position and strength, the minimum and maximum FWHM, and the integral of the Gaussian) are used to estimate the source position, the peak flux, the angular size and the total flux. The flux uncertainties have been derived from the best fit as well. Using this approach, five independent lists of photometry have been obtained at the five Hi-GAL wavebands.

The completeness limits have been estimated evaluating the CuTEx ability of recovering synthetic compact sources randomly dispersed on the original maps. Both the size and the flux of the generated sources mirror the distributions contained in the original CuTEx lists. The completeness limit at each waveband is then estimated as the flux value at which the histogram of the fraction of the recovered sources exceeds the threshold of 90% of the total number of injected synthetic sources having fluxes in that bin. The procedure is illustrated in Figure 8, and the obtained values are 1.75, 1.06, 0.60, 0.53, and 0.56 Jy at 70, 160, 250, 350, 500 μm, respectively.

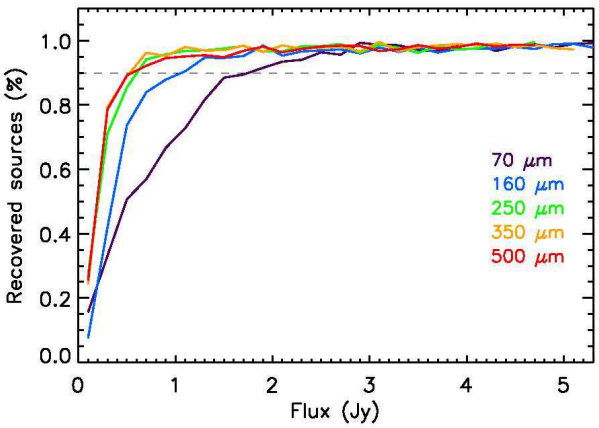

Fig. 8.— Completeness limit calculation for Hi-GAL photometry. The curves represent the percentage of recovered artificial sources as a function of their fluxes in the five Herschel bands. The dashed horizontal line represents the 90% limit.

Subsequently the sources extracted in each waveband have been associated by means of a simple spatial criterium (Elia et al. 2010) in order to obtain a band-merged catalog. The total number of entries in this catalog is 3476, composed by sources having at least a detection in one band. In Section 5 the further selection of a sub-sample of reliable SEDs eligible for the fit through a model is reported.

4.2. Cloud decomposition

Similarly to the source extraction performed on the Herschel maps, a search for spatially and kinematically coherent overdense structures has been carried out in the CO(1-0) $l-b-v$ cube, using cloud decomposition techniques. Doing this we do not aim at finding exactly the counterparts of the Herschel sources and at establishing a some

biunivocal correspondence between the two populations. Rather, due to the coarser spatial resolution of the CO(1-0) observations and to the different source extraction techniques adopted, the CO(1-0) coherent sources (hereafter "CO clumps", although in some cases they could not match exactly the definition of clump having typical cloud sizes) are expected to be generally more extended than the Herschel ones, and thus to be found in association with more than one of them in general.

For the cloud decomposition we used the CLOUDPROPS package[2] (Rosolowsky & Leroy 2006, 2011), which is also able to derive a set of the basic morphological and physical properties of found the clumps. We tested both the native clump finding algorithm present in the package, and the widely used cloud decomposition algorithm CLUMPFIND (Williams et al. 1994), that is also implemented in the package as alternative option. Although CLUMPFIND is known to be strongly depending on the initial parameter setup, as discussed in detail, e.g., by Brunt et al. (2003), Rosolowsky & Blitz (2005), Rosolowsky & Leroy (2006), and Elia et al. (2007), in this case it turned out to be more able than the native CLOUDPROPS search engine to detect structures with the same efficiency across the whole map, probably due to different rms noise conditions throughout the data cube [3].

The list of the detected clumps is reported in Table 2 in Appendix B, complemented with the following quantities provided by CLOUDPROPS and calculated as described in Rosolowsky & Leroy (2006), with some further tuning of the default settings:

- *Velocity dispersion.* It is derived as the second moment of the intensity distribution along the velocity dimension.
- *Distance.* To derive the heliocentric distances, the Galactic rotation curve of Brunthaler et al. (2011) (R_0 = 8.3 kpc, Θ_0 = 239 km s^{-1}) has been used instead of the default one of Reid et al. (2009) implemented in CLOUDPROPS.
- *Radius.* The deconvolved radius r is estimated as the geometric mean of the deconvolved major and minor axes of the clump, given in units of pc once the clump distance is known.
- *Mass.* The mass of the clump M is obtained as in Section 3.1, i.e. integrating the column density over the solid angle of the clump. The column density is derived by CLOUDPROPS as in Equation 2 with a X factor constant for all clumps. We then rescaled the mass considering a X factor varying with the Galactocentric distance as in Equation 3.
- *Virial mass.* The virial mass is calculated as $M_{\rm vir}[M_\odot] = 1040\sigma_v^2[\mathrm{km\ s^{-1}}]\ r[\mathrm{pc}]$, under the assumption that each clump is spherical and virialized with a density profile of the form $\rho \propto r^{-1}$ (Solomon et al. 1987). Density power laws with exponent 0 and -2 would require, instead, a constant of 1150 and 690 M$_\odot$ (km s^{-1})$^{-1}$ pc^{-1}, respectively.
- *Luminosity.* The clump luminosity in the CO(1-0) line is provided in units of K km s^{-1} pc^2. The conversion factor to solar luminosities for this transition is $4.9 \times 10^{-5} L_\odot[\mathrm{K\ km\ s^{-1}\ pc^2}]^{-1}$ (Solomon et al. 1992).

After ruling oututput sources having meaningless physical parameters (as not-a-number masses, luminosities, etc.) the final list is composed by 321 clumps.

5. Herschel sources: physical properties

5.1. SED building

In this section we derive the basic physical properties of the Hi-GAL compact sources from their spectral energy distributions (SEDs). However, first of all a selection has to be performed in order to obtain a reliable sample of SEDs eligible for the modified black body fit.

Where present, the flux at 70 μm is not considered in this fit, being generally affected by

[2]The CLOUDPROPS package is available at `https://people.ok.ubc.ca/erosolo/cprops/index.html`.

[3]In more detail, the native engine of CLOUDPROPS has not been able to detect evident structures in some portions of the map even at very low detection thresholds, that included a number of false detections in other locations. Instead, CLUMPFIND managed to recover all the main features of the data cube using a global and reasonable value of the global threshold (3σ, see Williams et al. 1994)

the direct contribution of a proto-stellar component; for this reason, its presence can be used as a signature to distinguish a proto-stellar from a starless core/clump (e.g. Bontemps et al. 2010; Giannini et al. 2012). We searched also for possible WISE 22 μm counterparts (detected at $S/N > 5\sigma$) within a searching radius of $12.6''$(corresponding to the WISE resolution at that wavelength and to the WISE and Herschel positional uncertainties combined in quadrature) around the Hi-GAL source coordinates. The low signal-to-noise ratio in our PACS 70 μm maps, responsible of the large flux completeness limit at this band, can result in an association between a WISE source and a Herschel one lacking emission at 70 μm. In these cases, the association is considered genuine and the source is classified as proto-stellar if at least the flux at 160 μm is available. In this way, 236 out of 943 Hi-GAL sources with a selected SED (see below) are found to be associated with a WISE counterpart.

To estimate which fraction of the WISE-Herschel associations could be spurious, we generated a random distribution of coordinate pairs having the same number and spatial coverage of the WISE sources in our field, and run the same procedure of matching with the Hi-GAL sources. Only 18 of the aforementioned 943 Hi-GAL sources are associated with a source generated in such a way, i.e. less than 8% if compared with the number of the WISE counterparts found. This percentage represents the occurrence of spurious matches that should be expected to affect our WISE-Herschel association.

At the longer wavelengths, we deal with the frequent case of the increase of the beam-deconvolved diameter, as estimated by CuTEx ($\theta_\lambda = \sqrt{FWHM_{maj,\lambda} \times FWHM_{min,\lambda} - HPBM_\lambda^2}$), at increasing wavelengths, already discussed by Motte et al. (2010) and Giannini et al. (2012). Due to this increase of the area over which the emission is integrated, many SEDs flatten or even rise longwards $\lambda \geq 250\mu$m.

Here we adopt the strategy of Motte et al. (2010), consisting in assuming a reference wavelength to estimate the source angular size, and scaling the fluxes at a larger wavelength λ by the ratio between the deconvolved sizes at the reference wavelength and at λ, respectively. Due to the further selection to identify SEDs eligible for the fit, described at the end of this section, the shortest wavelength always available is 250 μm, that we adopt as reference wavelength

$$\overline{F}_\lambda = F_\lambda \times \frac{\theta_{250}}{\theta_\lambda}, \qquad \lambda \geq 350\mu\text{m} \, . \tag{5}$$

This is based on the assumptions that *i*) the source is optically thin at $\lambda \geq 250$ μm; *ii*) the temperature gradient is weak (Motte & André 2001); *iii*) the radial density profile of the source is described by $\rho(r) \propto r^2$, then $M(r) \propto r$.

It is noteworthy that scaling fluxes in this way corresponds to consider fluxes emitted by the same volume of dust, that is more compatible with fitting a modified black body to a SED. On the other hand, hereafter it must be kept in mind that the physical properties derived from the fit of the scaled SEDs describe the average conditions of the source inside a volume delimited by the size detected at the reference wavelength. Finally, considering a smaller volume, we reduce the influence of possible multiplicities (i.e. shorter wavelength counterparts that appear confused in an unresolved source at 350-500 μm) on the fluxes composing the final SED.

A further selection has been performed on the SEDs built as described above, accepting only those: *i*) being composed by consecutive fluxes (at least three); *ii*) showing no dips (e.g. concave shape); *iii*) not peaking at 500 μm; *iv*) having a distance estimate, as described in Section 5.2.

After applying these constraints, we finally obtained a sample of 943 SEDs eligible for the fit, 255 of which are proto-stellar (184 of which with detected at both 22 μm and 70 μm, 52 only at 22 μm, and 19 only at 70 μm), and 688 starless.

The positions of these sources in the surveyed region are reported in Figure 9, where we introduce the color convention blue for proto-stellar objects, and red for the starless ones. We remark that some bright sources might have been ruled out from the present statistical analysis by the constraints we applied to deal with regular SEDs.

Furthermore we draw attention on the fact that many sources appear to lie on the most prominent filaments present in the maps. Although these filaments appear uniform in figures like those shown in Appendix A due to the choice of the intensity scale, in actual fact they possess a complex internal structure revealed by Herschel and character-

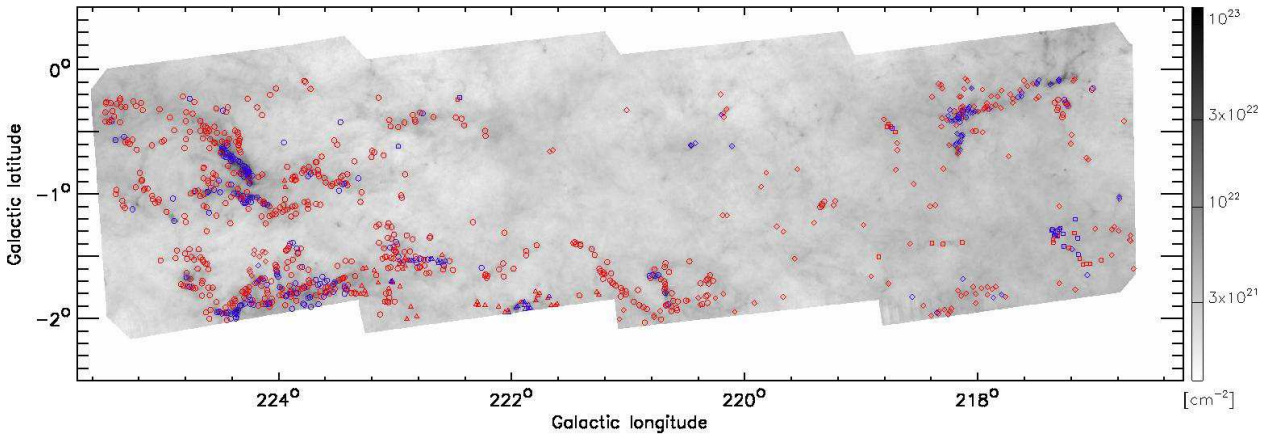

Fig. 9.— Spatial distribution of the Hi-GAL compact sources considered for the analysis in this paper (see text), overplotted on the column density map of Figure 5. Different symbols are used for sources associated to the four CO components identified in Section 3.1: circles, triangles, diamonds and squares correspond to the component I, II, III, IV, respectively. The blue and red colors are used to indicate proto-stellar and starless sources, respectively.

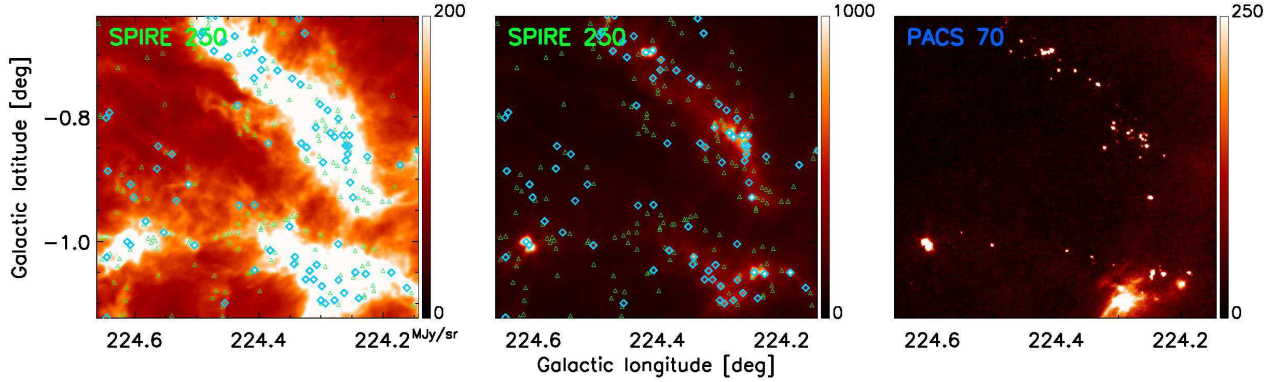

Fig. 10.— Positions of the sources detected in the Hi-GAL 250 μm map in the neighborhoods of [KKY2004]4. ***Left***: the map is rendered using the same intensity scale as in Figure 18, so that the brightest filaments appear as white uniform regions in which many compact sources are found (big cyan diamonds: sources admitted in the final sample; green small triangles: detections rejected for subsequent analysis). *Center*: to appreciate how these sources actually correspond to local intensity peaks also along the filaments, the same map is rendered using a less compressed intensity scale. *Right*: the Hi-GAL 70 μm map, in which both diffuse emission and filaments are typically much fainter than the sources, is shown to highlight the correspondence of the on-filament sources across the different bands, as an indication of their genuineness.

ized by the presence of numerous compact sources (see, e.g., Molinari et al. 2010a). This aspect is well exemplified by the Figure 10, where the positions of the sources extracted at 250 μm in the neighborhoods of the [KKY2004]4 cloud are superimposed on the map of this wavelength rendered by means of two different intensity scales. The first one is appropriate to show the appearance of the diffuse emission, while the second one is needed to reveal the internal structure of the bright filaments, where it is possible to find compact sources whose genuineness is confimred, for example, by the comparison with the 70 μm map. **The occurrence of false positives in our extraction can not be excluded a priori. However, since the detection is performed independently at each waveband, it is unlikely to systematically find counterparts of them at the other wavelengths. In any case the source selection described in this section, based on the regularity of the collected SED, ensures the reliability of the sources considered for the subsequent analysis.**

5.2. Distance assignment

The problem of the distance estimation of the Hi-GAL sources is a crucial point that has to be faced to derive a complete and meaningful set of physical properties for these objects. Fortunately in the portion of the Galactic plane hosting the $\ell 217-224$ field this issue turns out to be less problematic, thanks to both the low degree of confusion along the line of sight and the absence of the near/far ambiguity on the kinematic distance, as pointed out in Section 3.1.

A possible approach might consist in examining the line of sight in the CO(1-0) data cube corresponding to an Hi-GAL source, and to take the v_{lsr} of the brightest component encountered, as done for example in Russeil et al. (2011). Here however we want to exploit the additional information offered by the CO(1-0) data cube decomposition in clumps (Section 4.2): in the CO(1-0) line of sight containing the source, we consider the spectral channels assigned by CLOUDPROPS/CLUMPFIND to one or more clumps, and associate to the source the distance of the clump, if any, having the closest centroid. There is a double advantage in adopting this strategy: first, the distance assigned to all the sources associated to a given clump is the same, without finding a different distance at each spatial/spectral position in the CO(1-0) cube, perhaps affected by the clump internal kinematics unrelated with Galactic rotation. Second, this strategy acts quite efficiently in cases of presence, along the same line of sight, of a peripheral CO(1-0) feature of a large and bright clump and of a weaker but central feature of a smaller clump: in this case we believe that the Herschel source is more likely associated with the small clump being centered on it, rather than with the outer part of a large clump. Taking into account only the brightest line in this example, instead, would have lead to a completely different association.

The distance information can be exploited to generate a view of the spatial distribution of the sources in the Galactic plane (Figure 11, upper panel). In this figure we notice a certain degree of continuity in the distribution of the heliocentric distances, without significant gaps between the components I and II. To better illustrate how this classification works, the isotachs corresponding to the velocities conventionally separating the four components are also plotted. According to the spiral arm loci from Cordes & Lazio (2002)[4], in the longitude range we consider in this paper the Local arm should be encountered at $d \sim 0.8$ kpc, the Perseus arm at $d \sim 3$ kpc, and the Outer arm at $d > 9$ kpc, respectively.

Our results, in the limit of the reliability of the adopted rotation curve in this part of the Galaxy, partially confirm this view. Looking at the lower panel of Figure 11, the highest concentration of component I sources is found in the bins centered at 0.8 and 1 kpc. Instead, the distance distribution of the component II sources peaks around 2, 2.6, and 3.2 kpc, suggesting instead the presence of an inter-arm bridge of matter similar to those found by Carraro et al. (2005) in other locations of the TGQ. The 0.7-1.1, 2.0, 2.6 and and 3.2 kpc distances also correspond with the global distances (photometric or kinematic) assigned by Kim et al. (2004) to their clouds present in our field. The Outer arm is not detected in this portion of the TGQ, in agreement with Carraro et al. (2005) and

[4]In this case we cannot invoke the careful and more recent spiral arm determinations by Vallée (2005), because they were obtained based on a Galactic rotation curve very different ($R_0 = 7.9$ kpc) from the one we adopt here.

Xu et al. (2009). Finally, we notice that none of the sources we found at the farthest Galactocentric distances can be classified as belonging to the far outer Galaxy ($d > 15$ kpc Heyer et al. 1998).

5.3. SED fitting

As said above, a modified black body (described by the Equation 3.3, but with the terms $N(H_2)\,\Delta\vartheta^2_{500}$ replaced by M/d^2) has been fitted to the SEDs, to obtain concomitant estimates of the mass and the temperature for each individual source.

In Table 3 the astrometric, photometric and physical properties of the analyzed sources are resumed. Here we start discussing the physical diameter and the temperature (Figure 12). For sources provided with a distance estimate, the diameter D is easily obtained from the source deconvolved FWHM estimated at 250 μm. The histogram in panel *a* shows that our sample is composed by a mixture of cores ($D < 0.1$ pc) and clumps ($D > 0.1$ pc), according to the typical definitions of these object classes based on their size (e.g., Bergin & Tafalla 2007). It is important, therefore, to keep in mind that a relevant fraction of the compact sources analyzed in this work do not correspond to progenitors of single star sytems but, rather, to distant complex and large structures we cannot resolve (in particular, 153 out of 255 proto-stellar sources must be classified as clumps).

The two size distributions do not appear much different each other ($\langle D \rangle = 0.16$ pc in both cases), unlike in Giannini et al. (2012), where proto-stellar sources were found to be on average smaller that the starless ones. To better discuss this point, we notice that sources spread on a wide range of distances are used all together to build the histograms for both the samples, so that some large proto-stellar clumps located at long distances are obviously larger than closer pre-stellar cores. For this reason we show also the distributions of the diameters as they would appear if placed at a distance of 1000 pc (panel *b*). Also in this case, there is no clear indication of significant size differences. In fact, Giannini et al. (2012) adopted a more flexible criterium to decide the reference wavelength at which the source size is estimated: 160 μm when a detection at this wavelength were available, and 250 μm otherwise. Since many starless

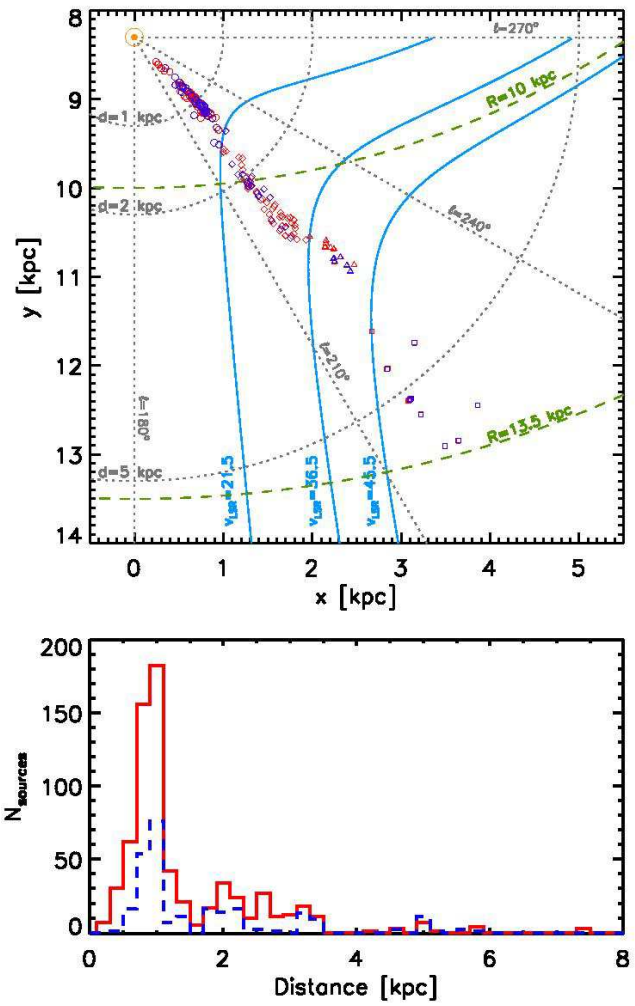

Fig. 11.— Top: sketch of the the TGQ containing the positions of the $\ell 217-224$ sources selected for the SED fit. The origin of the axes is in the Galactic center, and x and y designate the components of the Galactocentric distance (with x and y increasing towards the direction of $\ell = 270°$ and $\ell = 180°$, respectively. The symbol and color conventions are the same of Figure 9. The orange $\odot$ symbol represents the Galactic position of the Sun. The grey dotted lines indicate relevant longitude values, reported in the labels of the same color. The grey dotted and green dashed arcs represent relevant values of heliocentric and Galactocentric distance, respectively. Finally, the cyan solid lines are isotachs corresponding to the three v_{lsr} values separating the four main CO(1-0) components we identified in this paper for convenience. Bottom: histograms of the source heliocentric distances of the sources shown in the upper panel (blue for protostellar and red for starless, respectively). The bin width is of 200 pc.

sources are not detected at 160 μm, their size was estimated at 250 μm, where it appears generally larger (Section 5.1), thus favoring the observed segregation in size, while in our case the reference wavelength is the same in all cases.

Concerning the temperature distributions of the two classes, also in this case the dichotomy proto-stellar-warmer against starless-colder is not evident as in Giannini et al. (2012), again due to different reference size adopted in that case implying a more consistent flux scaling at the SPIRE wavelengths for the proto-stellar sources, finally leading to higher temperature and lower mass estimates. In our case, the uniform choice of the size at 250 μm as reference reduces the differences of the two distributions, that can be found in the presence of a significant high-temperature tail for the proto-stellar sources, and in the average temperatures ($\langle T_{ps} \rangle$ = 13.6 K, $\langle T_{sl} \rangle$ = 11.1 K). It is worthy of notice that the temperature is estimated on the range 160-500 μm: this implies that the difference between proto-stellar and starless sources is independent from the presence of a flux at 70 μm, i.e. the constraint we impose to classify the proto-stellar sources. Finally note that, unlike the size distribution, in this case there is no distance effect biasing the observed trend of the temperature.

5.4. An estimate of the clump and star formation efficiency

The combination of Hi-GAL and NANTEN data allow us to provide an estimate of the clump and star formation efficiency (CFE and SFE, respectively) for the four distance components seen towards $\ell 217 - 224$. Indicating the total mass of the compact sources (both proto-stellar and starless) with M_{cl} and the total cloud mass with M_{gas}, the CFE is expressed by $CFE = \frac{M_{cl}}{M_{cl}+M_{gas}}$. The cloud masses can be easily derived from the column density map of Figure 5, resolving the infrequent cases of overlap of two distance components along a CO line of sight by adopting the distance corresponding to the brightest feature in the spectrum. Due to the different spatial coverage of the Hi-GAL and NANTEN observations, for each component we derive again the cloud mass only in the lines of sight falling inside the common area. For the same reason, to compute M_{cl} we must consider only the Hi-GAL sources lying in the area surveyed in the CO(1-0) line, but all the sources considered for the present analysis fulfill this requirement because they are required to have an associated kinematic distance. Since the column density and the compact sources masses have been computed using the same opacity k_0, our CFE will not be affected by the large uncertainties associated to the choice of this constant. The obtained CFEs for the four components are 0.055 ± 0.008, 0.024 ± 0.003, 0.07 ± 0.01, and 0.027 ± 0.004, respectively. The uncertainties have been estimated assuming a conservative error of 10% on both the source masses and pixel-to-pixel column density, combined in quadrature.

In the same way, if M_* is the total mass of the formed stars, the SFE is expressed by $SFE = \frac{M_*}{M_*+M_{gas}}$. To compute M_* we consider only the Hi-GAL proto-stellar cores lying in the area surveyed in the CO(1-0) line, obtaining core total masses of 2880, 2540, 2140, and 2550 $M_\odot$ for the four components, respectively. Finally, these values have been converted in stellar masses assuming a core-to-star conversion efficiency $\varepsilon_{\rm eff} = 1/3$ (Alves et al. 2007; André et al. 2010), and a average SFE of $8^{+2}_{-1}\times10^{-3}$, $3.9^{+0.9}_{-0.6}\times10^{3}$, $1.2^{+0.3}_{-0.2}\times10^{-2}$, $5.8^{+1.2}_{-0.8}\times10^{-3}$ has been obtained in the four cases. Here the relative uncertainties are not simply the same associated to the CFE, since one must take into account also the assumptions on the $\varepsilon_{\rm eff}$. Following Kauffmann & Pillai (2010), we adopt $\varepsilon_{\rm eff} = 1/2$ as upper limit for this coefficient.

Further considerations, however, lead us to take these estimates as lower limits for the real SFE: *i*) this derivation of the SFE is based only on FIR/sub-mm observations, neglecting the mass of more evolved young stellar objects detected only in the medium infrared; *ii*) as it will be discussed in Section 6, it is possible that a small fraction of sources classified as starless cores, not taken into account for this calculation, may already have a strongly embedded early-stage proto-stellar content.

On the other hand, at increasing distances the so-called compact sources correspond to structures having increasing physical sizes, departing from the definition of core. Therefore, unresolved distant regions are considered as a single source, although containing in most cases a complex internal substructure consisting of dense cores and dif-

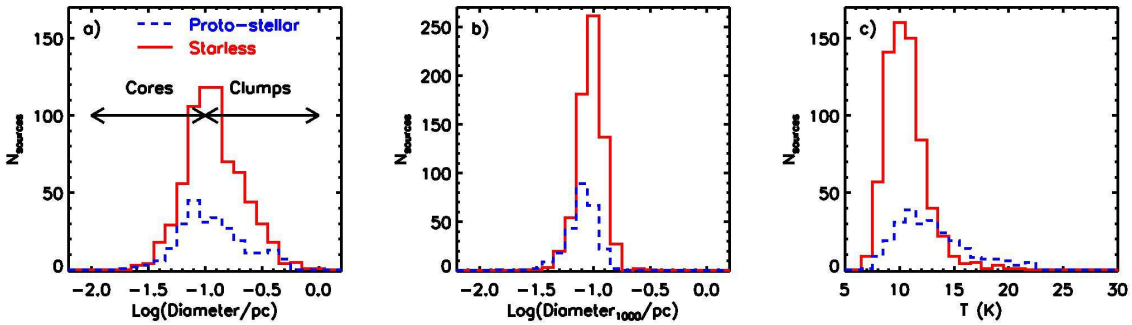

Fig. 12.— Histograms of diameter (panel a) and temperature (panel b) of starless (red) and proto-stellar (blue) sources in $\ell 217 - 224$.

fuse matter. In particular, for such sources classified as proto-stellar clumps, only a fraction of the mass is taking part in the ongoing star formation processes, nevertheless the total mass is entirely taken into account in the SFE calculation.

In any case, these results are comparable with typical SFE values. In the 40 star forming complexes analyzed by Murray (2011), the SFE ranges from 0.002 to 0.2, with an average of 0.08. In Lada et al. (2010), who analyzed 11 nearby molecular clouds, it ranges from ~ 0.003 (Pipe nebula) to ~ 0.09 (RCrA). Compared with these data, the SFE of our four components can be classified as relatively low. It is noteworthy, in this sense, that we find the lowest SFE in what we call component II, that is likely spatially related to the Maddalena's cloud, i.e. one of the most striking cases of giant molecular with an unusual combination of high gas mass and little evidence for star formation (e.g., Heyer et al. 2006; Megeath et al. 2009).

5.5. Mass distribution of the sources

In the following discussion we focus on the starless objects that are also gravitationally bound, which we call pre-stellar cores, because they may give rise to the formation of proto-stellar clusters. In the recent Herschel literature, to study the stability of such sources, the lack of kinematic information has forced the adoption of the critical Bonnor-Ebert (BE) mass as a surrogate for the virial mass (Könyves et al. 2010; Giannini et al. 2012). We use it also in the present case: although in principle we could exploit the velocity dispersion obtainable the CO(1-0) data to estimate the virial mass, in practice the CO(1-0) line spectral resolution is too coarse for determining reliable line widths.

The BE mass is given by:

$$M_{\rm BE} = 2.4\ r_{\rm BE}\ a^2/G\ , \qquad (6)$$

where a is the sound speed at the source temperature, G is the gravitational constant, and $r_{\rm BE}$ is the BE radius (in pc), that in this case is assumed to coincide with the source radius observed at the reference wavelength. We consider gravitationally bound, and therefore pre-stellar, all the starless sources with $M > M_{\rm BE}$ (cf. Olmi et al. 2010; Giannini et al. 2012). According to this definition, we find 398, 131, 42 and 19 pre-stellar sources associated to the gas velocity component I, II, III, and IV, corresponding to the 82%, 94%, 98% and 100% of the starless core populations, respectively.

In our case the availability of four different distance components gives us the chance to discuss a trend emerging from the recent Herschel literature. The studies of the relatively nearby star-forming regions of Aquila (Könyves et al. 2010), Orion-A (Polychroni et al. 2013, in prep.), and Vela-C Giannini et al. (2012), located at 260, 414 and 700 pc away, respectively, provided an estimate of the pre-stellar fraction over the total starless core number of 69%, 87%, and 94%, respectively. These percentages have been estimated using a less severe threshold for identifying the gravitationally bound sources, namely $M > 0.5 M_{\rm BE}$. If we adopt the same criterium for the components I-IV of the present work, the fraction of pre-stellar sources increases to 94%, 100%, 100%, 100%, respectively. We notice a general trend of this frac-

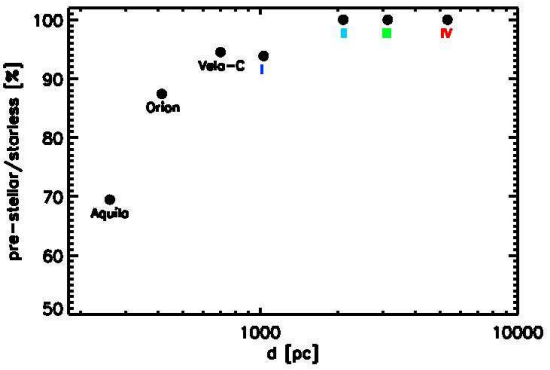

Fig. 13.— Fraction of pre-stellar sources over the total number of starless ones for seven different regions, as a function of the average region distance. Data from previous literature have labels in black, while data from this article have labels with different colors, according with the color-component convention adopted in Figure 4.

tion to increase with the distance (see Figure 13), highlighting a clear selection effect against gravitationally unbound structures located at large distances (at $d \geq 2000$ pc the saturation is practically achieved). This is implicit in fact in Equation 6: given a certain SED and changing its distance d, M varies as d^2, while $r_{\rm BE}$ varies as d, thus making it easier for the same SED to fulfil the BE criterium when d increases. On one hand, this means that to exploit this fraction of gravitationally bound sources in a region as an evolutionary indication about its star formation capability is affected by a strong and practically unsolvable bias related to the distance. On the other hand, the slight deviation of the behavior of the component I from the general trend seen in Figure 13 can be considered, from the qualitative point of view, indicative of an intrinsically lower occurrence of pre-stellar sources compared, for example, with the Vela-C region.

A mass vs radius plot, shown in Figure 14, can be used to illustrate and quantify the discussion on the gravitational stability of the starless cores (neglecting the turbulence and magnetic field supports against gravity). The lines corresponding to 1 $M_{\rm BE}$ mass behavior at two different temperatures, $T = 10$ K and 20 K, respectively, are displayed (orange dashed lines). It can be seen that all the unbound sources (red open symbols) lie below the curve at $T = 20$ K, while, at the same time, most of the bound ones (red filled symbols) show a remarkable degree of boundedness (i.e. $M \gg M_{\rm BE}(T = 20{\rm K})$). Although this diagram is meaningless in the case of the proto-stellar sources, since part of the mass has already formed the central protostar(s) or could have been ejected in form of proto-stellar jets, we report also these sources in the plot (blue filled symbols) for completeness.

In Figure 14 "Larson's third law" is shown as a green dotted-dashed line. Originally formulated as $M(r) > 460 M_\odot (r/{\rm pc})^{1.9}$ Larson (1981) it has been revised later: Solomon et al. (1987) found a value 2 for the power-law exponent, i.e. a constant column density as a function of the radius. Since the two values are very similar, we plot this relation in its original form. In any case, it can be seen that the sources of our sample do not obey a precise power law. Therefore we do not try here to fit a power law to the mass-size distribution of the pre-stellar cores in $\ell 217 - 224$.

The mass vs radius diagram is also a useful tool for checking the presence of the conditions for MSF, based on the intuitive concept that to form massive stars a conspicuous mass reservoir concentrated in a relatively small volume is required. In the recent literature a theoretical column density threshold of 1 g cm^{-2} (Krumholz & McKee 2008) is largely invoked and used to identify candidate sites of MSF (see also Section 3.2). It can be represented as a locus in the bi-logarithmic plot of Figure 14, down to a minimum core mass value that, for a 10 $M_\odot$ star and a core-to-star conversion efficiency $\varepsilon_{\rm eff} = 1/3$, amounts to 30 $M_\odot$. A small but significant fraction of sources (both pre- and proto-stellar) exceed this threshold and can be considered therefore potential progenitors of massive stars. Also, an empirical and less demanding limit for MSF has been estimated by Kauffmann & Pillai (2010), based on observations of Infrared Dark Clouds (IRDCs Egan et al. 1998), as $M(r) > 870 M_\odot (r/{\rm pc})^{1.33}$ and reported in Figure 14. Further sources, belonging to all the four distance components of $\ell 217 - 224$, fulfil this threshold, testifying the occurrence of the conditions for having MSF also in this portion of the TGQ and, in particular, at remarkably large Galactocentric distances ($R > 11$ kpc for the com-

ponent IV).

Moving to the analysis of the mass distribution, it becomes necessary to deal with homogeneous samples, from both the spatial and the evolutionary point of view. Thus, we consider only the pre-stellar sources of the closest velocity component (I), a choice that also ensures enough statistics to obtain a reliable mass distribution. Again, it is correct to calculate this kind of distribution only for the pre-stellar sources, as the masses of the proto-stellar ones are not representative of the initial core mass.

The core mass distribution is reported in Figure 15. The mass completeness limit of $1.9 M_{\odot}$ has been estimated from the flux completeness limit at the reference wavelength 250 μm (Section 4) using the modified black body equation, combined with the average temperature and distance of the sample, and $\beta = 2$. The turn over of the mass function falls around 3 $M_{\odot}$, too close to the completeness limit to claim that we are well tracing the log-normal behavior of the mass distribution below the turnover point (as, e.g., in Könyves et al. 2010). We then fit a power law $N(\log M) \propto M^{\alpha}$ to the high-mass part of the distribution using an approach based on the method of maximum likelihood and independent from the histogram binning Olmi et al. (see 2013, and references therein). It allows us to determine the lower limit of range of validity of the power-law, $\log(M_{\rm inf}/M_{\odot}) = 0.65$, and its slope $\alpha = -1.0 \pm 0.2$.

Whereas the core mass functions derived for nearby regions through spectral lines (Orion A, $\alpha = -1.3 \pm 0.1$, Ikeda et al. 2007), Spitzer (Perseus, Serpens and Ophiucus, $\alpha = -1.3 \pm 0.2$, Enoch et al. 2008), and Herschel observations (Aquila Rift, $\alpha = -1.45 \pm 0.2$, Könyves et al. 2010) have slope values consistent with those of the stellar initial mass function ($\alpha = -1.3 \pm 0.7$ for single stars, Kroupa 2001; $\alpha = -1.35 \pm 0.3$ for multiple systems, Chabrier 2005), when the considered sample is contaminated by the presence of larger structures (clumps) as in our case (see Figure 14), the slope generally tends to be shallower, towards the values found for the clump mass functions (e.g., $\alpha = -(0.6 - 0.8)$ for various clouds, Kramer et al. 1998; $\alpha = -0.6$ for the Galactic center region, Miyazaki & Tsuboi 2000; $\alpha = -1.0$ for the Vela-D cloud, Elia et al. 2007). A very similar behavior was observed also in the case of the Herschel-based source mass distribution of the Vela-C cloud ($\alpha = -1.1 \pm 0.2$, Giannini et al. 2012), affected by the same kind of contamination.

In our case, we can check on the same region this gradual steepening of the mass function from clumps to cores, by considering the masses of the CO clumps extracted as described in Section 4.2, and belonging to the component I (purple histogram in Figure 15, $\alpha = -0.7 \pm 0.3$). This steepening is quite usual and is explained, in the general case, as a consequence of the fragmentation of the clumps in cores that constitute the last fragment generating the single star (or multiple system). However, in our case, notice that the error bars associated to the two slopes (obtained with the same method) partially overlap. Furthermore, the disagreement between Herschel- and CO-derived column densities highlighted in Figure 2 surely introduces an uncertainty on the slope of the CO clump mass function larger than that derived simply from the power-law fit.

It is possible to make a direct comparison with the mass function slope derived by Kim et al. (2004) for their "Group I" clumps (namely sources associated with CMa OB1 and G220.8-1.7), $\alpha = -0.59 \pm 0.32$, that is consistent with our result.

6. Evolutionary framework

To further investigate the differences between the proto- and pre-stellar sources considered so far, we discuss here a plot of the bolometric luminosities vs the envelope masses. In the previous literature (Saraceno et al. 1996; André et al. 2000; Molinari et al. 2008) such a diagram has been already used as a meaningful method to infer the evolutionary status of the compact sources, through the comparison between their positions in the plot and the theoretical tracks obtained from models of accreting cores. Such tracks start from a given initial mass and initially follow an almost vertical path corresponding to the accretion phase. Subsequently, the proto-stellar outflow activity produces mass loss and disperses the residual envelope (horizontal portion of the tracks).

Recently, this diagnostics has been applied to the clump populations of star forming regions observed by Herschel (Elia et al. 2010; Bontemps et al. 2010; Hennemann et al. 2010; Giannini et al. 2012; Veneziani et al. 2013), re-

vealing some degree of segregation between proto- and pre-stellar sources. A general caveat about the use of this diagram for distant star forming regions consists in the fact that, rigorously speaking, the evolutionary tracks are calculated for a single protostar. Instead, in cases like ours, many sources are in fact clumps having an unresolved internal structure, with the possible presence of few proto-stars, and/or smaller pre-stellar cores. Therefore, a precise star formation timeline cannot be deduced from such tracks. Of course also in these cases to find a higher luminosity at the same envelope mass is indicative of a more evolved evolutionary stage, but it is difficult to understand whether this is a general property of the entire (unresolved) population hosted by the clump, or it is essentially due to only the brightmost contained source(s).

To build this diagram we used the mass values discussed in the previous sections. They represent, in fact, the envelope mass in the case of a proto-stellar source, and of course the whole mass of a starless one. The luminosities have been derived integrating the whole observed SED, including *i*) the flux of the best-fitting modified black body at 1 mm, to take into account also the millimetric portion of the SED we do not observe directly, and *ii*) the WISE flux at 22 μm, where available, to ensure a better estimate in the case of the sources most evolved and then bright in the mid-infrared unlike, for example, the similar plot in Giannini et al. (2012). By the way, in Molinari et al. (2008) and Hennemann et al. (2010), since their targets were constituted by limited amounts of proto-stellar sources (this explains the lack of the pre-stellar ones in their analysis), more extended SEDs were collected, down to 8.3 and 3.6 μm, respectively. On one hand, this increases and improves the bolometric luminosity estimation for more evoled sources, on the other hand this operation requires special care in checking the reliability of the short-wavelength counterpart assignment to each single FIR source, and therefore it lies outside the goals of the present work.

The $L_{\rm bol}$ vs $M_{\rm env}$ plot is reported in Figure 16, whith the same symbol convention of Figure 14. Furthermore, the symbol size linearly scales with the source temperature. The theoretical evolutionary tracks for the low and high mass regimes adopted by (Molinari et al. 2008) are also plotted.

Also in our case, the proto-stellar sources and the pre-stellar ones populate quite different regions of the diagram, corresponding to the accreting core phase in the first case, and to a quiescent or collapsing core in the second, respectively. Obviously, there is a transition region with some overlap between the two populations, especially at high masses (discussed below), but a global look suggests a certain degree of segregation.

In the low-mass regime, where the distinction of well-defined evolutionary classes makes more sense (André et al. 2000, and references therein), the region corresponding to the Class 0 to I transition appears populated, as in Giannini et al. (2012). However, we remind the reader that the $L_{\rm bol}$ vs $M_{\rm env}$ plot is not a tool **suitable** for obtaining a precise classification, essentially because *i*) Hennemann et al. (2010) showed that sources classified as Class I from their NIR-to-MIR SED are found to be compatible instead with a Class 0 status based on their FIR fluxes, and there is not a sharp transition from Class 0 to I to II in their $L_{\rm bol}$ vs $M_{\rm env}$ diagram; *ii*) this evolutionary classification can not be easily extended to the high-mass regime, a fortiori when the considered source is a large clump hosting multiple star formation. Furthermore, comparing our diagram with those of Molinari et al. (2008) and Hennemann et al. (2010), we can explain the lack of evolved sources in ours with the aforementioned different ranges used for calculating $L_{\rm bol}$. In summary, due to both the investigated spectral range and mass regime, this $L_{\rm bol}$ vs $M_{\rm env}$ plot can not be used to obtain a classical single-YSO classification.

From the point of view of the distance, it is remarkable that proto-stellar activity is detected also in the most distant sources, confirming the occurrence of the star formation also at $R > 11$ kpc (see, e.g., Reipurth & Yan 2008; Yun et al. 2009, and references therein).

Focusing on the source temperatures, the first general indication is that the most luminous proto-stellar sources, i. e. the most evolved, are also the warmest, and of course the proto-stellar are on average warmer than the pre-stellar ones as already indicated by Figure 12. Furthermore, the luminous pre-stellar sources occupying regions of the diagram where early-stage proto-stellar cores are instead expected (beginning of the evolution-

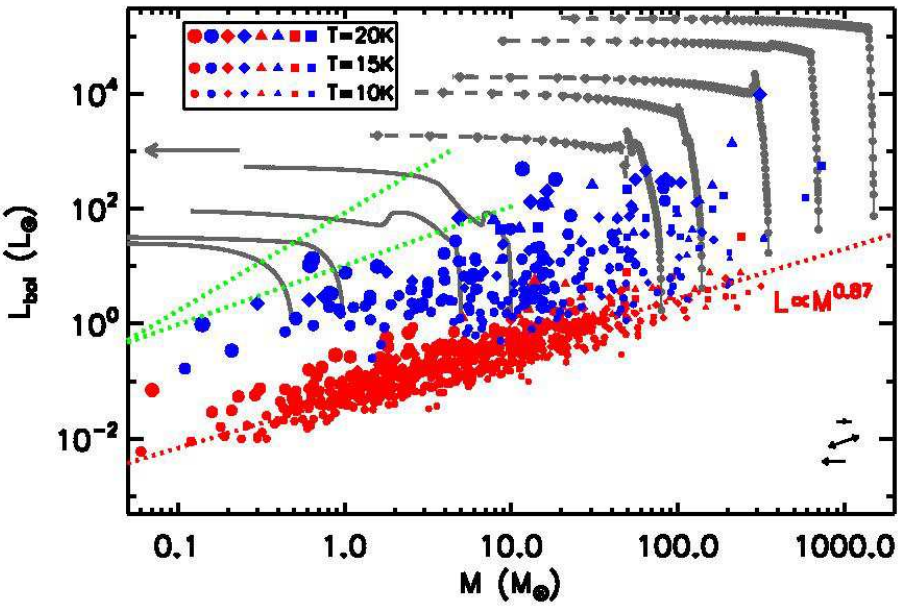

Fig. 16.— Plot of the bolometric luminosity vs the mass of the the same sources of Figure 14, with the same symbol and color convention. In addition, the symbol size varies according to the source temperature, as illustrated in the legend. Grey and black solid lines represent the evolutionary tracks for the low- and high-mass regime, respectively, taken from Molinari et al. (2008). The grey arrow indicates the evolution direction, while green dashed lines delimit the region of transition between Class 0 and Class I sources (André et al. 2000) in the low-mass regime. The red dotted line represents the best-fitting power law ($L_{\rm bol} \propto M_{\rm env}^{0.87\pm0.02}$) for the distribution of the prestellar sources. In the right bottom corner the effects of possible sources of random or systematic uncertainty affecting the points of the plot are represented as arrows, as in Figure 14 (see it for further explanation).

ary tracks) are generally characterized by a higher temperature. We interpret this fact as the presence of a strongly embedded early-phase proto-star(s) not detected at both the 22 and 70 μm wavebands. This might lead to misclassify early proto-stellar sources as pre-stellar, a fact that should be taken into account in the future analyses of core/clump populations extracted from the Herschel maps.

Finally, we notice that while the proto-stellar sources are spread over a wide range of possible evolutionary stages, the displacement of the bulk of the pre-stellar sources follows a power-law in a region of the diagram corresponding to a stage in which no mass accretion has started yet. A similar behavior was already discussed in Giannini et al. (2012) for the Vela-C cloud but here it looks more evident and, more interestingly, it appears the same over several spatially unrelated regions. A power-law fit gives a dependence $L_{\rm bol} \propto M^{(0.87\pm0.02)}$. This slope is very similar to the 0.85 value found by Brand et al. (2001) for their sample of proto-stellar sources, while it is very different from the 0.42 value found by Giannini et al. (2012) for pre-stellar sources in Vela-C. However, we need to increase the statistics of this slope across the Galactic plane, exploiting the whole Hi-GAL data base, before stating a possible link between the evolutionary stage of a star forming region and the slope of the luminosity vs mass relation of the pre-stellar cores.

6.1. Star formation rate

The $L_{\rm bol}$ vs $M_{\rm env}$ diagram can be exploited to quantify the star formation rate (SFR) of the four distance components we identify in $\ell217-224$. For the high mass regime ($M > 10M_{\odot}$) we followed the method of Veneziani et al. (2013). Briefly, it consists in associating each proto-stellar source mass to a nearby evolutionary track, and to consider the mass M_f of the central object at the end of the track (corresponding to a time t_f), when the envelope clean-up phase is completed. The SFR is calculated by adding the M_f/t_f ratios of all sources. In the low-mass regime, instead, we use the Equation 1 of Lada et al. (2010) that assumes a constant final mass and time, $0.5M_{\odot}$ and 2×10^6 yr, respectively. Anyway, the contribution of the low-mass part to the total SFR amounts to 8% for the component I and less than 1% for the remaining components. We find, for the components I-IV, $SFR = 2.6^{+0.2}_{-0.3}\times10^{-4}, 1.39^{+0.03}_{-0.05}\times10^{-4}, 6.30^{+0.04}_{-0.23}\times10^{-5}, 4.77^{+0.26}_{-0.05}\times10^{-5} M_{\odot}$ yr^{-1}, respectively. In the portion of the Galaxy corresponding to $\ell217-224$, thus, $SFR_{\rm tot} = 5.1^{+0.2}_{-0.3}\times10^{-4} M_{\odot}$ yr^{-1}. The error bars have been estimated assuming a 20% average uncertainty on both mass and luminosity. Of course, larger uncertainties come from the choice of the YSO model and from the distance estimate and are not easily quantifiable (see Veneziani et al. 2013).

In two single Hi-GAL tiles of the first Galactic quadrant, namely centered close to $[\ell, b] = [30^{\circ}, 0^{\circ}]$ and $[59^{\circ}, 0^{\circ}]$, Veneziani et al. (2013) obtained $SFR = 9.5\times10^{-4}$ and $1.6\times10^{-4} M_{\odot}$ yr^{-1}, respectively, considering all the distance components together. Taking into account that the solid angle spanned by the $\ell217-224$ maps is about five times larger than in the case of these two inner Galaxy fields, we conclude that in our case the SFR per solid angle is significantly lower, as expected for the outer Galaxy. However, the forthcoming studies based on the Hi-GAL survey will provide a more exhaustive description of the SFR as a function of the Galactic position, and an extrapolation to the SFR of the entire Galaxy.

6.2. Diagnostics of CO clumps

If one wants to to apply a diagnostics based on a luminosity-mass relation also to the clumps extracted from the CO(1-0) data, the most meaningful way is to use the virial mass. Indeed, the way the clump mass is calculated in our case, namely as proportional to the intensity integrated over all the channels assigned by the cloud decomposing algorithm to the clump (Equation 3), makes it directly proportional to the luminosity, which strictly speaking is a "luminous mass":

$$M_{CO} = cL_{CO} \quad . \tag{7}$$

Bolatto et al. (2008), who used the same decomposition algorithm we used, report a value for the constant $c = 45$ with M_{CO} in $M_{\odot}$ and L_{CO} in K km s^{-1} pc^2. Instead, the estimate of the virial mass is independent from the clump luminosity. We show the plot of these two quantities (derived as in Section 4.2) in Figure 17, panel *a*, where we adopt the same symbol convention of Figure 16 to separate sources associated to the different dis-

tance components. Furthermore, blue and red colors are used for clumps associated with at least one Hi-GAL proto-stellar source and clumps associated only with Hi-GAL starless ones, respectively. Finally, smaller green symbols represent the CO clumps that do not contain Hi-GAL sources, or that lie outside the area surveyed by Herschel.

Two lines corresponding to Equation 7 for two different slopes have been plotted (grey dotted lines). They are obtained correcting the c value of Bolatto et al. (2008) (corresponding to $X = 2 \times 10^{20}$ (K km s^{-1})$^{-1}$ cm^{-2}), by the minimum (upper line) and maximum (lower line) values of X used for the clumps of this paper, respectively, according to Equation 3. This is equivalent to saying that all the values of the luminosity-luminous mass pairs lie in the stripe of the plot delimited by these two lines (and in particular the majority of them lies close to the upper one, namely that corresponding to the smaller value of X).

The less rigorous classification between "proto-stellar" and "starless" CO clumps probably explains the reason of the absence of a clear segregation like that found in Figure 16 for dust cores and clumps. It is noteworthy, however, that for $M_{CO} \gg 10^3$ M$_\odot$ the most luminous clumps *i*) all have a proto-stellar content; *ii*) all are supervirial. If we consider all the supervirial clumps in our sample, namely 22 objects corresponding to $\sim 7\%$ of the total, 17 of them have a proto-stellar content, 3 are starless and 2 are not associable with Herschel sources. This indication is surely relevant, but not resolutive or sufficient to identify evolved clumps in such a diagram. On one hand, the majority of the supervirial structures are found to host star formation; on the other hand, many "proto-stellar" clumps can appear as sub-virial, since their global physical properties plotted here cannot describe local conditions that could allow star formation in limited parts of them. Finally, unlike the case of the Hi-GAL $L_{\rm bol}$ vs M diagram, we do not recognize any power-law trend either in the whole sample of clumps or in the single identified classes.

7. Conclusions

The first Hi-GAL observations of the TGQ consist of a "chunk" of ~ 20.5 deg^2 corresponding to the longitude range $216.5° \leq \ell \leq 225.5°$. Here we presented a first study based on both the overall displacement of the far-infrared emission in this region and on the statistical analysis of the properties of the compact sources derived from photometric measurements. The NANTEN CO(1-0) observations have added the fundamental information about gas kinematics. This study confirms the view of the outer Galaxy as an interesting laboratory to investigate star formation processes, benefitting of the generally simple structure of the velocity field (compared with the inner Galaxy). Summarizing, we found that:

- In the Hi-GAL images it is possible to recognize the dust emission from all the velocity components in this sky region detected in the line observations presented in this and previous papers (Kim et al. 2004). In particular we identify four components (I-IV) located at average heliocentric distances of 1.1, 2.2, 3.3, and 5.8 kpc respectively. The overlap among these components is quite infrequent, making clearer their identification.

- The large-scale column density and temperature distribution for the cold component of the dust reveal a variety of conditions, with star formation sites preferentially distributed along filaments. Interestingly, two of these are likely associated with the S296 HII region, which might be responsible of triggering star formation in these filaments.

- We obtained a five-band Hi-GAL compact source catalog of this region, complemented with the WISE 22 μm photometry and with the distance information derived from the spatial association with the clumps extracted from the CO(1-0) data set. The classification between proto-stellar (provided with a detection at 70 μm and/or at 22 μm and 160 μm) and starless sources has been made.

- A modified black body has been fitted to the regular and well sampled SEDs (255 proto-stellar, 688 starless), to derive temperatures and masses. On average, the proto-stellar sources are found to be warmer than the starless ones. Concerning the source size, moreover, we find that our sample is composed by a mixture of clumps and cores, due

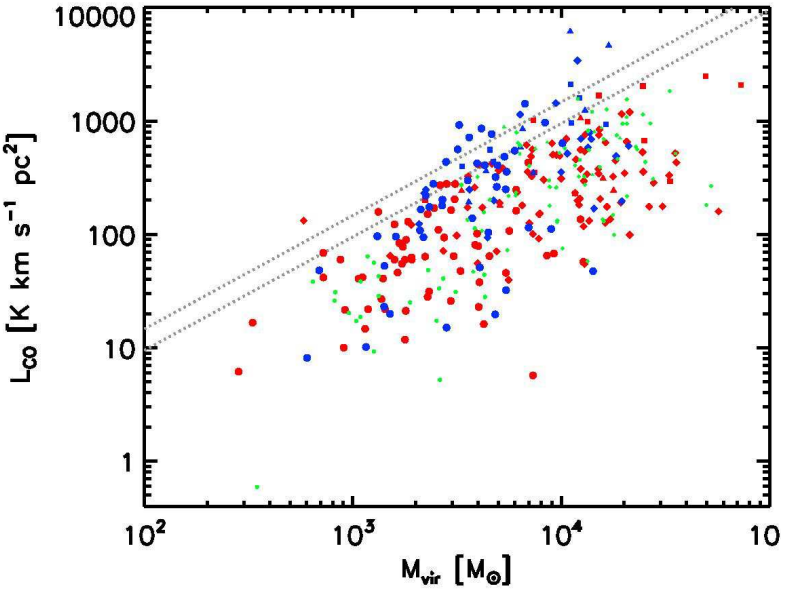

Fig. 17.— Plot of the luminosity vs the virial mass of the CO clumps, derived as in Section 4.2. The symbol-distance convention is the same of Figure 14. The blue color indicates clumps containing protostellar Hi-GAL sources (at least one), while the red color indicates clumps associated only with starless Hi-GAL sources. Sources lacking Hi-GAL counterparts or lying outside the area surveyd by Herschel are plotted with small green symbols. Two grey dotted lines represent the luminosity vs luminous mass relation for the two extreme values of the X factor used in this paper.

to the wide involved distance range. Looking at their spatial distribution in the Galactic plane, the local and Perseus spiral arm are clearly seen, although a remarkable amount of sources with assigned inter-arm distances are also found. The limited range of investigated Galactic longitudes does not allow a better recognition of a grand design spiral pattern.

- We derived the SFE for the four velocity components (0.008, 0.004, 0.012, 0.006, respectively). These values lead to classify the star formation in these regions as not very efficient. On one hand, being only based on Herschel far-infrared photometry, they should be taken as lower limits. On the other hand, a systematic overestimate of the SFE with increasing distance has to be taken into account.

- Applying a virial analysis to the starless Hi-GAL sources, large fractions of them (ranging from 82% for the component I to 100% for the component IV) are found to be gravitationally bound, i. e. pre-stellar. We show that these percentages must be considered as upper limits, because they are biased by a selection effect related to the distance and implicit in the adopted criterium.

- In the mass vs radius plot for the pre-stellar sources we do not recognize any clear power-law behavior. We use this tool to check the potential ability of clump/cores to form massive stars, based on the different thresholds of Krumholz & McKee (2008) and Kauffmann & Pillai (2010). In both cases we find condensations compatible with high-mass star formation in all the distance components.

- A power-law $N(\log M) \propto M^{\alpha}$ has been fitted to high-mass portion of the core/clump mass distribution of the pre-stellar sources belonging to the component I. Similarly to the Vela-C case (Giannini et al. 2012), its slope $\alpha = -1.0 \pm 0.2$ is shallower (although still consistent within the errors) than the stellar IMF slope and the similar slopes also found for cores in nearby star forming regions, and steeper than the slopes found for the gas clump distributions, as in this case ($\alpha = -0.7 \pm 0.3$).

- The $L_{\rm bol}$ vs $M_{\rm env}$ plot of the Hi-GAL sources reveals an evident separation between proto- and pre-stellar sources. For both classes the warmest sources are, in general, the most evolved of their class. Few proto-stellar sources populate the region of the diagram where objects in transition between Class 0 and Class I are expected to lie, whereas the majority populate the Class 0 region. This classification obviously weakens when distant sources are considered, namely those corresponding to large and massive ($M \gtrsim 100 M_{\odot}$) clumps. Using this diagram as in Veneziani et al. (2013) we are able to derive also an estimate of the star formation rate of $SFR_{\rm tot} = 5.1 \times 10^{-4} M_{\odot}$ yr^{-1}.

- Most of the CO clumps (93%) are subvirial. Line observations at better angular resolution would probably reveal denser supervirial substructures. The remaining 7% fraction of supervirial clumps (22 objects) is in most cases associated with Hi-GAL protostellar sources, suggesting that these clumps fulfill globally and not only locally the conditions for the gravitational collapse to occurr.

  Besides the characterization of star forming regions in the $\ell 217 - 224$, this article gives also a first contribution to the larger statistics that will be built exploiting the entire Hi-GAL survey archive. Prescriptions and caveats on using the photometric data, on combining them with kinematics derived from CO observations, and on addressing effects of distance-resolution have been explicitly discussed in several points of the text.

PACS has been developed by a consortium of institutes led by MPE (Germany) and including UVIE (Austria); KU Leuven, CSL, IMEC (Belgium); CEA, LAM (France); MPIA (Germany); INAF-IFSI/OAA/OAP/OAT, LENS, SISSA (Italy); IAC (Spain). This development has been supported by the funding agencies BMVIT (Austria), ESAPRODEX (Belgium), CEA/CNES (France), DLR (Germany), ASI/INAF (Italy),and CICYT/MCYT (Spain). SPIRE has been developed

by a consortium of institutes led by Cardiff Univ. (UK) and including: Univ. Lethbridge (Canada); NAOC (China); CEA,LAM (France); INAF-IFSI, Univ. Padua (Italy); IAC (Spain); Stockholm Observatory (Sweden); Imperial College London, RAL, UCL-MSSL, UKATC, Univ. Sussex (UK); and Caltech, JPL, NHSC, Univ. Colorado (USA). This development has been supported by national funding agencies: CSA (Canada); NAOC (China); CEA, CNES, CNRS (France); ASI (Italy); MCINN (Spain); SNSB (Sweden); STFC, UKSA (UK); and NASA (USA). DE, MP, and KJLR are funded by an ASI fellowship under contract numbers I/005/11/0 and I/038/08/0. DP is funded through the Operational Program "Education and Lifelong Learning" and is co-financed by the European Union (European Social Fund) and Greek national funds.

Facilities: Herschel Space Observatory, NANTEN.

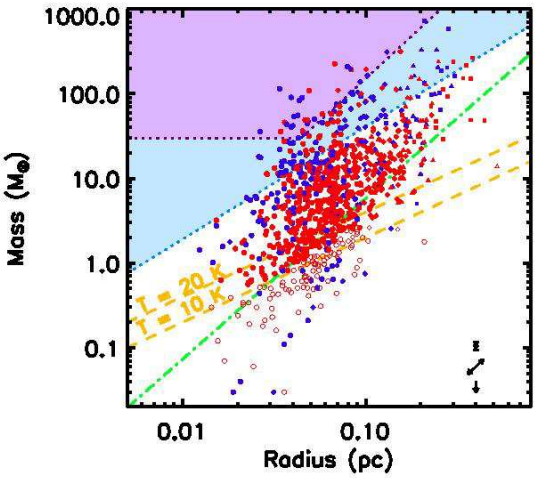

Fig. 14.— Mass vs radius diagram for the Hi-GAL sources in $\ell 217 - 224$. Symbols with the same shape convention of Figure 9 represent pre-stellar (red filled), starless unbound (red open), and proto-stellar (blue filled) sources. Orange dashed lines are the loci of sources with $M = 1M_{\rm BE}$, for $T = 10$ K and $T = 20$ K, while the green dotted-dashed line represents the power-law estimated by Larson (1981). The area with a purple background represents the region corresponding to the conditions for MSF to occurr, according to the Krumholz & McKee (2008) threshold (purple dotted line). It represents a sub-region of the blue-background area, corresponding to the MSF threshold of Kauffmann & Pillai (2010) (blue dotted line). In the bottom right corner of the plot three possible sources of uncertainty are represented: the error bar represents a 10% uncertainty on the mass coming from the original photometry, the double arrow indicates the shift that would be produced by a $\pm 10\%$ uncertainty on the distance, and the down arrow indicates the shift that would be applied if a different opacity law was adopted, as proposed in Section 3.3.

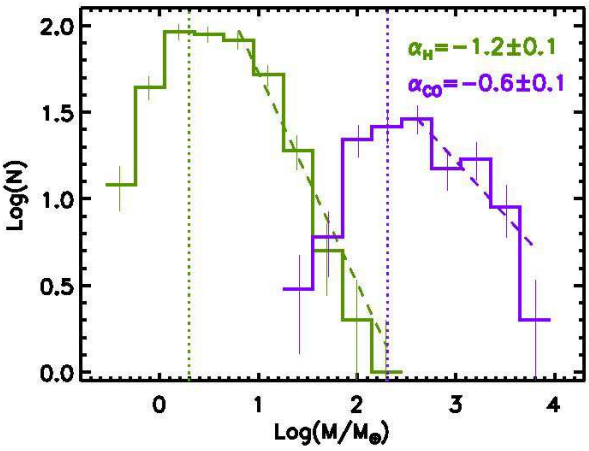

Fig. 15.— Source mass distribution in $\ell 217-224$ (green: Hi-GAL pre-stellar sources, purple: CO clumps). The error bars are estimated as $\sqrt{N}$ statistical uncertainties. The dashed lines represent the maximum likelihood fit (see Olmi et al. 2013) to the linear portion of the two mass distributions, and the corresponding slopes are reported. As a consequence of the adopted fitting technique, the slope does not depend on the arbitrary choice of the bin width. The dotted vertical lines represent the mass completeness limit in the two cases: for the Hi-GAL observations it has been derived as described in the text, whereas for the NANTEN observations we followed the method of Simon et al. (2001).

A. Hi-GAL images: the ℓ224, ℓ222, ℓ220, and ℓ217 tiles from 70 to 500 μm

B. List of CO clumps

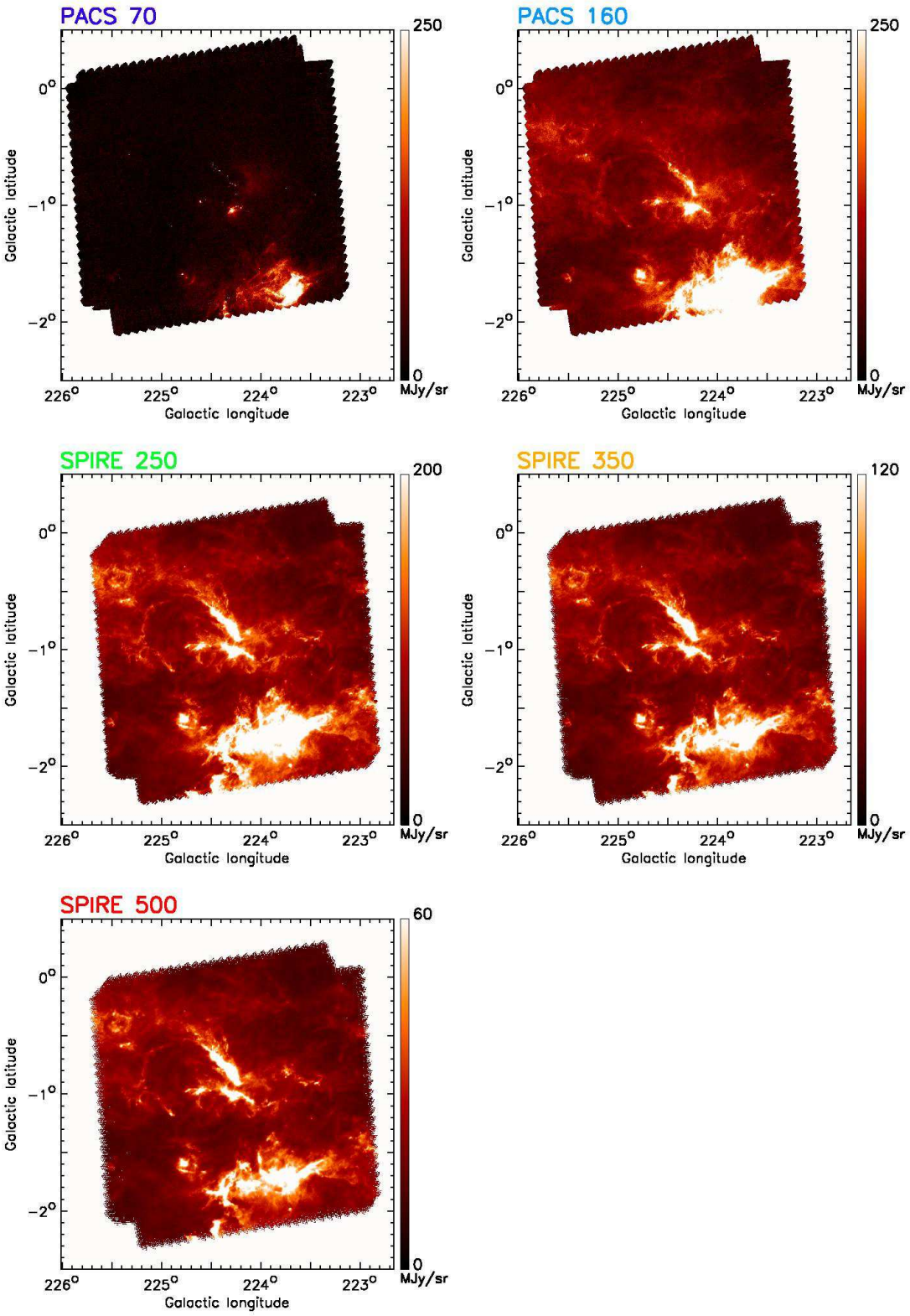

Fig. 18.— Hi-GAL maps of the ℓ224 field at 70, 160, 250, 350, 500 μm.

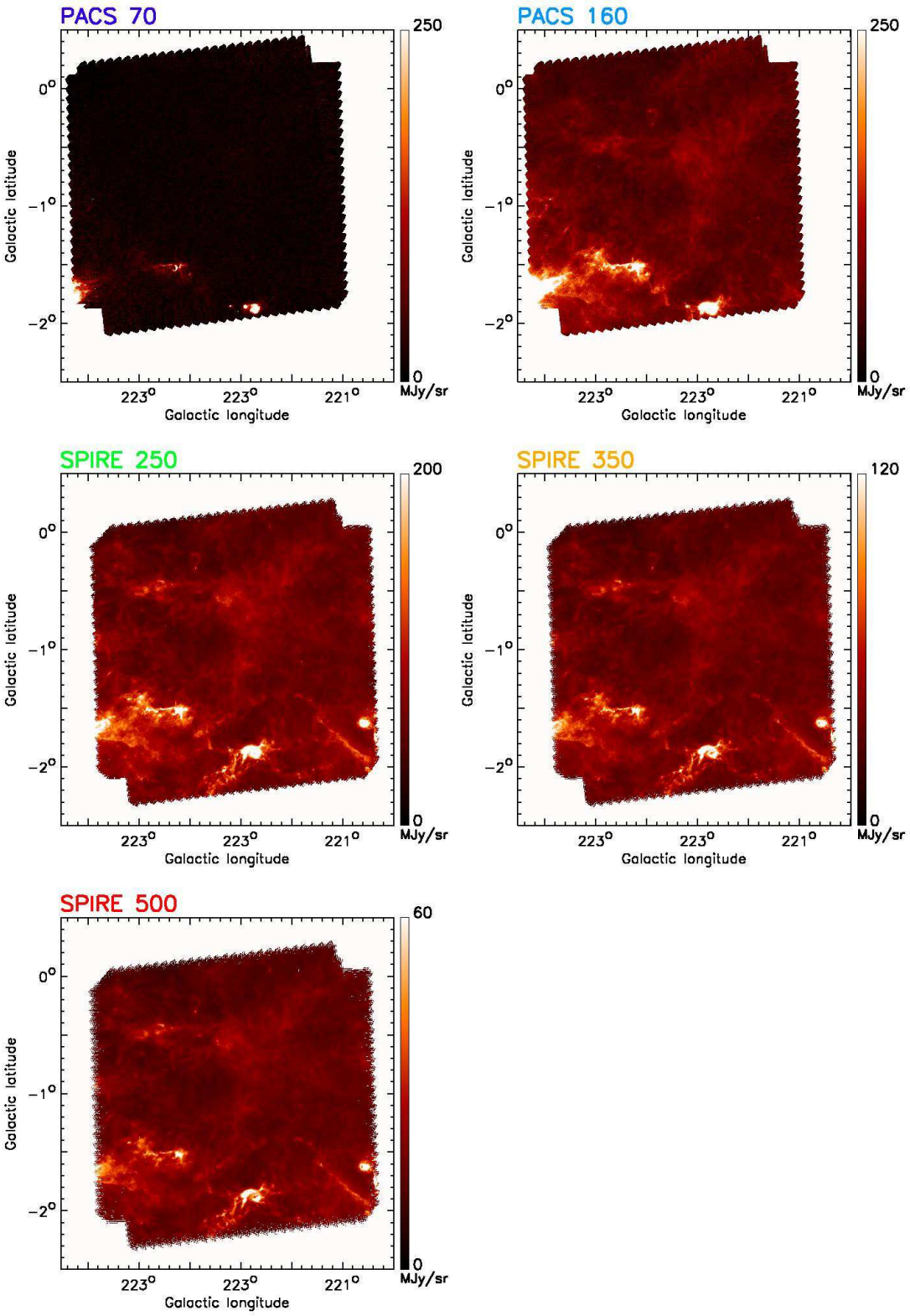

Fig. 19.— The same as Figure 18, but for the ℓ222 field.

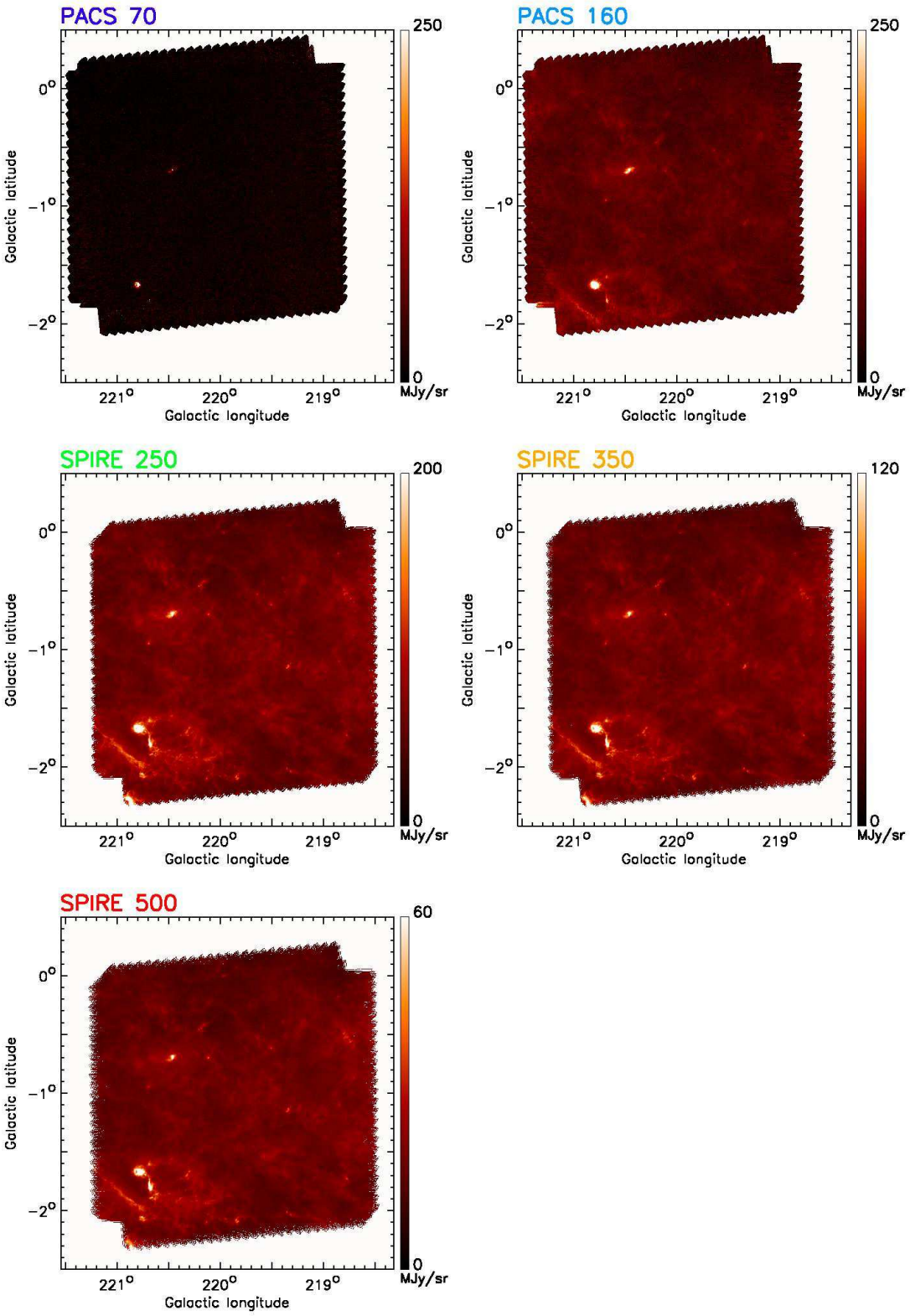

Fig. 20.— The same as Figure 18, but for the ℓ220 field.

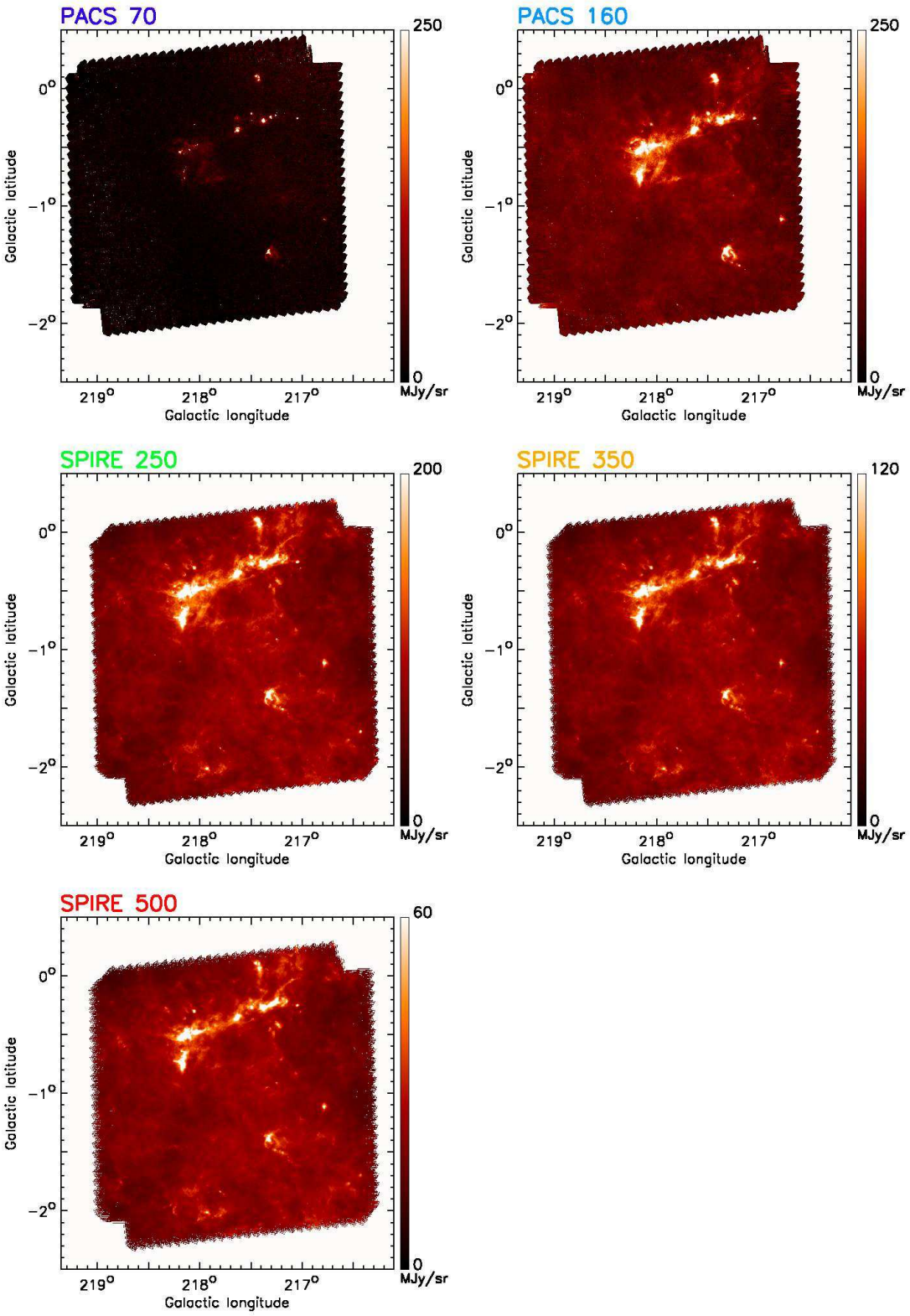

Fig. 21.— The same as Figure 18, but for the ℓ217 field.

TABLE 2
LIST OF THE CLUMPS DETECTED IN THE CO(1-0) LINE

ID	ℓ [°]	b [°]	v_{lsr} [km s^{-1}]	σ_v [km s^{-1}]	d [kpc]	r [pc]	M [$M_\odot$]	M_{vir} [$M_\odot$]	L [K km s^{-1} pc^2]
1	216.61829	-1.82868	44.0	1.8	4.3	5.7	5770.	19154.	704.6
2	216.62572	-1.64908	30.6	0.9	2.6	6.5	2707.	5009.	366.3
3	216.64683	-2.24570	23.8	1.9	1.9	3.6	3943.	13551.	554.5
4	216.66404	-2.08390	25.9	2.0	2.1	5.0	6811.	20697.	947.4
5	216.66706	-1.70928	32.8	0.8	2.8	8.9	5936.	6110.	791.9
6	216.67371	-1.42988	30.9	1.1	2.6	5.5	3611.	7170.	487.8
7	216.68618	-0.48407	55.2	1.7	6.1	8.7	6204.	25071.	671.9
8	216.69400	-1.88198	29.7	1.6	2.5	7.8	8458.	19509.	1151.3
9	216.70952	-0.44180	26.5	1.2	2.1	2.8	401.	3964.	55.6
10	216.72395	-2.36709	24.1	1.5	1.9	4.0	3712.	9794.	521.4
11	216.74965	-1.87533	51.6	0.9	5.4	8.2	4526.	6321.	512.5
12	216.81554	-1.10761	30.7	1.6	2.6	5.0	4327.	13447.	585.9
13	216.81786	-1.35122	31.9	1.1	2.7	5.8	4182.	7258.	561.7
14	216.84120	-1.98124	24.9	1.7	2.0	6.5	7738.	20583.	1082.9
15	216.87085	-2.05228	31.6	2.2	2.7	10.4	1980.	52479.	266.4
16	216.87131	-2.20133	20.4	1.6	1.5	5.3	5724.	13453.	819.4
17	216.89132	-1.53862	30.5	1.6	2.6	6.0	2776.	15040.	376.3
18	216.91345	-2.21344	27.6	1.7	2.3	6.8	11262.	20623.	1552.9
19	216.95635	-0.11574	20.1	1.1	1.5	2.1	105.	2814.	15.0
20	216.96588	-1.31297	29.3	1.1	2.4	6.1	1111.	7907.	151.7
21	216.97759	-1.82817	30.4	1.9	2.5	7.1	1296.	26417.	175.8
22	216.98623	-0.36119	58.7	1.6	6.7	12.9	4969.	35366.	516.3
23	217.01355	-1.80752	24.7	1.9	1.9	5.3	1398.	19528.	195.9
24	217.07652	-1.55184	50.0	1.0	5.1	11.5	13848.	12248.	1602.2
25	217.07859	-0.71760	25.3	1.4	2.0	2.4	505.	4893.	70.6
26	217.13268	-1.83133	54.8	2.2	5.9	15.1	18877.	72960.	2068.5
27	217.13893	-1.40723	51.3	1.0	5.3	10.7	8402.	11192.	958.8
28	217.14853	-2.16251	22.4	1.1	1.7	6.6	1262.	8803.	179.1
29	217.16301	-1.83244	32.8	1.0	2.8	9.7	5215.	10575.	697.5
30	217.17056	-1.45563	32.0	1.2	2.7	3.2	697.	4431.	93.8
31	217.17616	-2.09673	41.9	1.3	3.9	4.8	5176.	8574.	647.0
32	217.18633	-1.21478	52.3	1.1	5.5	9.4	2024.	11649.	228.6
33	217.19393	-1.31640	54.1	0.9	5.8	19.7	8476.	16360.	938.0
34	217.21256	-1.16125	30.2	1.5	2.5	5.5	1463.	11980.	198.9
35	217.24703	-0.56298	26.5	0.9	2.1	4.6	1241.	3551.	172.4
36	217.26359	-1.45943	47.4	0.9	4.7	5.0	4689.	4539.	558.4
37	217.27331	-2.03231	28.2	1.6	2.3	9.2	8295.	24668.	1141.5
38	217.27597	-0.25348	16.1	1.1	1.1	1.9	1194.	2327.	174.3
39	217.30057	-2.25778	26.0	1.5	2.1	7.9	5359.	18446.	746.5
40	217.32318	-2.12037	33.3	1.4	2.9	9.7	3466.	18649.	462.3
41	217.33114	-1.33540	50.2	1.3	5.1	6.5	18263.	11112.	2114.3
42	217.35038	-0.07286	26.6	1.5	2.1	2.8	8211.	6348.	1140.5
43	217.43133	-2.20728	41.8	1.2	3.9	5.1	4524.	7506.	566.8
44	217.43689	-1.62192	28.3	1.3	2.3	4.8	1908.	8826.	262.7
45	217.48365	-2.23507	33.3	1.6	2.8	9.5	7115.	26795.	950.1
46	217.48940	-1.73221	26.8	1.9	2.1	3.3	1479.	12223.	205.2
47	217.52488	-0.07782	23.6	0.9	1.8	2.4	1631.	2197.	230.3
48	217.52520	-2.05917	41.2	1.4	3.8	6.6	2650.	14100.	334.2
49	217.58998	-0.65801	23.4	2.7	1.8	1.8	409.	13394.	57.8
50	217.59529	-2.17524	42.1	1.4	3.9	8.1	6917.	15589.	866.2
51	217.59816	-2.33317	30.8	2.1	2.6	7.2	13550.	33112.	1838.6
52	217.62439	-0.83164	26.2	2.0	2.1	3.8	1473.	15375.	205.2
53	217.64804	-2.13506	30.8	1.5	2.6	6.4	5097.	15993.	691.8
54	217.67658	-0.27373	21.9	0.8	1.6	3.7	502.	2716.	71.5
55	217.67767	-1.74748	26.9	1.3	2.1	2.9	523.	5515.	72.6
56	217.67987	-0.18635	26.4	1.6	2.1	4.5	4979.	12423.	693.3
57	217.69956	-1.09217	26.6	1.5	2.1	4.1	540.	10151.	75.1
58	217.71058	-0.68278	28.7	1.5	2.3	7.4	1276.	16562.	175.4

TABLE 2—*Continued*

ID	ℓ [°]	b [°]	v_{lsr} [km s^{-1}]	σ_v [km s^{-1}]	d [kpc]	r [pc]	M [$M_\odot$]	M_{vir} [$M_\odot$]	L [K km s^{-1} pc^2]
59	217.71504	-2.28461	51.8	1.4	5.3	6.5	10590.	14067.	1209.7
60	217.79114	-1.87444	33.6	1.8	2.9	6.5	4509.	21059.	601.5
61	217.81175	-2.07470	25.4	1.2	2.0	4.1	4330.	6365.	606.0
62	217.82549	-0.75672	24.1	1.6	1.8	4.8	835.	12811.	117.7
63	217.83223	-2.04447	29.8	1.2	2.4	7.3	4193.	10394.	572.8
64	217.85049	-1.31174	52.5	0.9	5.4	8.4	8898.	7358.	1011.8
65	217.85109	-1.86782	26.2	1.0	2.1	5.9	1294.	6493.	180.4
66	217.85510	-0.83449	28.9	1.0	2.3	5.4	1700.	6074.	233.6
67	217.91541	-2.26242	32.8	1.4	2.8	8.7	9466.	16527.	1269.9
68	217.93003	-2.06501	34.7	1.2	3.0	8.6	5723.	13022.	758.8
69	217.93015	-0.65582	26.7	1.6	2.1	5.2	2446.	13292.	340.3
70	217.97411	-2.33651	29.9	1.0	2.4	6.5	2935.	7020.	400.9
71	218.00000	-2.02904	25.3	1.1	2.0	3.8	2982.	4643.	417.7
72	218.03485	-0.12363	27.0	1.3	2.1	5.4	2548.	9998.	354.0
73	218.03869	-2.08777	9.6	1.0	0.5	1.0	115.	1039.	17.2
74	218.04493	-1.82313	32.3	1.5	2.7	9.3	8882.	21335.	1196.4
75	218.05294	-0.30104	28.4	1.3	2.3	6.7	24699.	11965.	3405.1
76	218.11081	-0.36260	21.1	1.5	1.5	3.7	780.	8942.	111.7
77	218.11564	-1.82006	28.0	1.4	2.2	6.6	5698.	13715.	787.3
78	218.14830	-2.20643	28.4	1.3	2.3	6.5	2948.	11655.	406.4
79	218.16229	-0.54526	25.5	1.3	2.0	5.4	10267.	9427.	1438.1
80	218.17237	-2.31574	31.8	0.8	2.6	6.3	2378.	3966.	321.4
81	218.17886	-1.45503	63.8	1.0	7.4	13.9	17026.	15169.	1680.9
82	218.20702	-2.26182	34.3	0.9	2.9	7.8	4813.	6200.	640.6
83	218.22667	-2.04647	33.7	1.3	2.8	8.2	6292.	15240.	840.7
84	218.24427	-1.99777	26.0	1.5	2.0	3.8	3589.	9506.	501.4
85	218.31216	-0.73223	29.0	1.1	2.3	5.1	1712.	6136.	235.5
86	218.34052	-2.34400	31.3	1.2	2.6	5.4	2203.	8751.	298.9
87	218.35491	-0.12208	28.0	1.0	2.2	3.7	1876.	3835.	259.5
88	218.35827	-0.33033	27.2	1.6	2.1	5.8	4653.	16313.	646.4
89	218.36033	-2.19445	29.4	1.2	2.4	8.7	2001.	12997.	274.4
90	218.38635	-2.13527	26.6	1.3	2.1	8.7	1213.	14362.	169.1
91	218.39177	-0.31332	32.9	1.6	2.7	9.6	3952.	24602.	531.2
92	218.44969	-1.88503	26.6	2.2	2.1	6.2	1264.	30638.	176.1
93	218.45210	-1.68007	28.4	2.2	2.3	6.7	2408.	32962.	332.2
94	218.45495	-1.43652	64.6	1.3	7.5	14.2	20753.	24681.	2035.8
95	218.45760	-1.22120	32.8	1.3	2.7	7.0	2805.	12414.	377.4
96	218.45861	-1.87242	32.8	1.2	2.7	10.3	5586.	15164.	751.5
97	218.49399	-0.46073	32.2	1.6	2.7	3.5	950.	9555.	128.3
98	218.49497	-0.08676	59.4	1.4	6.5	6.9	9305.	13403.	983.7
99	218.50857	-1.84000	29.9	1.0	2.4	14.3	964.	13625.	132.0
100	218.50865	-0.44554	28.3	1.7	2.2	6.2	2341.	17734.	323.5
101	218.53027	-2.36531	32.0	2.0	2.6	5.7	4153.	23123.	561.4
102	218.58402	-0.90594	22.0	1.5	1.6	2.4	277.	5592.	39.5
103	218.59721	-2.08729	34.7	1.1	2.9	17.3	4920.	20718.	654.5
104	218.61812	-0.61193	26.8	2.3	2.1	2.9	906.	16318.	126.2
105	218.65378	-1.30765	34.7	1.3	2.9	9.2	2583.	15113.	343.6
106	218.65763	-1.39615	29.7	1.0	2.4	4.5	1385.	5068.	189.8
107	218.66472	-2.18965	31.7	1.6	2.6	8.2	4358.	22846.	590.4
108	218.66841	-1.63922	34.7	2.3	2.9	6.8	3245.	35693.	431.7
109	218.69304	-0.76835	30.7	0.9	2.5	4.1	715.	3150.	97.5
110	218.75213	-0.44043	55.9	2.2	5.8	10.0	22483.	49378.	2488.3
111	218.77892	-1.84992	31.8	1.1	2.6	7.8	4688.	9030.	635.3
112	218.79081	-1.77784	34.6	1.5	2.9	8.3	3365.	18212.	448.1
113	218.80046	-1.36580	36.1	2.1	3.1	7.4	3952.	35247.	521.5
114	218.80047	-0.40866	22.4	2.4	1.6	2.2	385.	12918.	54.8
115	218.82371	-0.17535	60.4	1.0	6.6	12.6	4323.	12250.	453.5
116	218.84698	-2.32736	30.7	1.6	2.5	5.7	2865.	15311.	390.9

TABLE 2—*Continued*

ID	ℓ [°]	b [°]	v_{lsr} [km s^{-1}]	σ_v [km s^{-1}]	d [kpc]	r [pc]	M [$M_\odot$]	M_{vir} [$M_\odot$]	L [K km s^{-1} pc^2]
117	218.88310	-1.51551	45.5	0.6	4.3	7.0	1620.	2226.	199.1
118	218.90849	-2.23681	27.5	1.7	2.2	8.2	3131.	25332.	434.7
119	218.94575	-1.95912	32.1	1.5	2.6	8.1	3619.	18335.	489.9
120	218.95846	-2.35521	0.0	1.1	0.2	0.3	4.	346.	0.6
121	218.96655	-1.23197	34.2	1.7	2.9	8.4	2671.	24761.	357.1
122	219.05289	-2.20551	30.6	1.7	2.5	6.9	6944.	19697.	948.4
123	219.06029	-1.84722	30.1	1.5	2.4	8.7	4807.	20610.	658.6
124	219.16395	-1.64909	28.3	2.4	2.2	9.5	1150.	56849.	159.1
125	219.21546	-1.18276	35.1	1.6	2.9	7.3	2609.	20157.	347.2
126	219.23624	-0.35023	31.5	0.6	2.5	4.1	477.	1509.	64.9
127	219.24433	-2.31049	28.2	1.5	2.2	6.6	981.	15808.	135.9
128	219.29442	-1.56392	30.6	1.9	2.5	7.5	2261.	27567.	309.1
129	219.29619	-1.11911	25.4	1.2	1.9	2.9	1226.	4182.	172.3
130	219.30648	-2.12974	30.0	1.7	2.4	3.1	1889.	9450.	259.1
131	219.31675	-1.09479	17.4	1.3	1.2	2.2	157.	4018.	22.9
132	219.35489	-1.24640	32.1	1.2	2.6	7.9	1343.	12180.	182.1
133	219.39198	-0.98446	16.3	1.1	1.1	2.0	214.	2320.	31.4
134	219.42825	-1.16293	35.7	1.1	3.0	7.4	2342.	9987.	310.7
135	219.43898	-1.41559	27.7	2.5	2.1	2.7	711.	17937.	98.8
136	219.45225	-1.70908	32.4	1.6	2.6	4.9	2188.	12845.	296.2
137	219.47299	-1.52531	34.6	0.5	2.9	14.6	1174.	4257.	156.8
138	219.47882	-0.90028	32.3	1.3	2.6	6.7	1525.	12275.	206.6
139	219.49497	-1.51006	51.1	2.0	5.0	8.2	2497.	33324.	293.2
140	219.51974	-1.60112	30.9	1.5	2.5	6.4	5074.	13947.	693.1
141	219.56282	-0.99047	35.0	1.3	2.9	6.7	1744.	11647.	232.4
142	219.59557	-1.39016	31.8	1.1	2.6	7.3	3631.	9816.	493.4
143	219.64914	-0.91668	34.8	1.1	2.9	6.8	2268.	8228.	302.9
144	219.66109	-1.44992	34.7	0.9	2.9	4.6	805.	4151.	107.6
145	219.67558	-2.17179	30.2	1.2	2.4	3.8	1610.	6050.	220.9
146	219.68265	-1.18561	17.7	0.7	1.2	1.7	139.	958.	20.3
147	219.71339	-2.37602	12.6	0.8	0.8	1.6	260.	1090.	38.5
148	219.73047	-2.04188	26.9	1.5	2.1	4.7	3284.	11769.	458.6
149	219.73797	-0.11036	36.7	1.0	3.1	4.6	1363.	5075.	180.0
150	219.77673	-1.44166	32.2	1.4	2.6	4.0	1114.	7827.	151.2
151	219.78109	-1.25631	36.5	2.1	3.1	3.5	984.	15995.	130.1
152	219.83611	-0.92944	25.1	1.4	1.9	3.4	2307.	7222.	325.1
153	219.84160	-2.01182	30.9	0.9	2.5	6.5	2812.	5238.	384.3
154	219.84398	-2.19972	12.2	0.9	0.7	1.4	194.	1331.	28.8
155	219.84890	-1.27179	18.5	1.1	1.3	3.4	304.	4271.	44.2
156	219.86069	-1.00864	17.9	2.4	1.2	2.1	393.	12785.	57.2
157	219.86273	-2.21884	29.1	0.9	2.3	4.0	973.	3543.	134.4
158	219.86409	-1.37585	19.5	1.7	1.4	2.7	451.	8542.	65.2
159	219.96747	-0.13501	33.7	1.6	2.8	6.8	1097.	17718.	147.6
160	219.97538	-2.37066	12.6	0.8	0.8	1.3	176.	817.	26.1
161	220.02312	-1.90182	31.0	1.2	2.5	6.4	3694.	9119.	505.1
162	220.04748	-1.97550	34.2	1.2	2.8	8.1	4155.	12371.	557.6
163	220.04813	-2.14261	13.2	0.9	0.8	2.1	525.	1737.	77.7
164	220.07720	-0.57029	26.9	1.8	2.0	5.4	974.	17223.	136.1
165	220.12973	-1.20465	33.7	1.3	2.7	7.6	4004.	12966.	539.3
166	220.13756	-1.26730	18.5	0.8	1.3	3.6	650.	2180.	94.3
167	220.14007	-0.28800	30.1	1.0	2.4	3.2	1805.	3631.	248.2
168	220.14528	-0.44460	24.4	1.0	1.8	4.8	1426.	4544.	201.8
169	220.14630	-0.12833	36.0	0.6	3.0	6.4	1865.	2241.	247.7
170	220.16245	-1.50227	33.9	1.0	2.8	5.7	1621.	5583.	218.1
171	220.16500	-1.44552	36.2	0.9	3.0	7.5	2678.	6900.	355.2
172	220.22442	-1.95845	33.0	1.0	2.7	6.4	4533.	6825.	613.2
173	220.27914	-0.68848	34.9	2.2	2.9	5.7	2129.	27799.	284.9
174	220.29300	-0.85491	22.2	1.4	1.6	3.7	642.	7797.	91.8

TABLE 2—*Continued*

ID	ℓ [°]	b [°]	v_{lsr} [km s^{-1}]	σ_v [km s^{-1}]	d [kpc]	r [pc]	M [$M_\odot$]	M_{vir} [$M_\odot$]	L [K km s^{-1} pc^2]
175	220.29833	-2.26271	12.3	1.0	0.7	1.4	288.	1330.	42.8
176	220.30473	-2.08209	13.1	0.7	0.8	1.6	281.	721.	41.7
177	220.32080	-1.79356	14.0	1.0	0.9	2.5	743.	2573.	109.7
178	220.34555	-1.24850	18.2	1.1	1.2	1.7	332.	2297.	48.3
179	220.39158	-1.99274	34.1	0.8	2.8	5.2	2416.	3575.	324.9
180	220.43577	-1.37462	18.3	1.2	1.2	1.8	280.	2712.	40.8
181	220.44935	-0.69346	22.2	1.1	1.6	2.8	328.	3782.	46.9
182	220.45987	-0.25588	28.8	1.7	2.2	2.2	907.	7035.	125.7
183	220.46326	-2.09991	11.3	0.9	0.6	1.6	377.	1263.	56.2
184	220.47238	-0.62280	29.1	1.9	2.2	2.8	3729.	10703.	516.1
185	220.50764	-2.23354	34.5	2.8	2.8	6.0	1354.	49782.	181.7
186	220.50895	-1.64215	14.4	1.3	0.9	1.9	435.	3046.	64.2
187	220.56194	-0.14878	36.8	1.5	3.1	6.7	2350.	15867.	311.0
188	220.62506	-1.90139	12.1	1.1	0.7	1.8	1114.	2116.	165.7
189	220.70520	-2.13950	9.1	1.2	0.5	0.8	146.	1183.	21.9
190	220.74079	-2.36335	33.3	1.3	2.7	6.5	2391.	12118.	323.4
191	220.74275	-2.04401	33.4	0.4	2.7	2.9	978.	580.	132.2
192	220.77745	-1.68182	13.4	1.1	0.8	2.0	1884.	2433.	278.9
193	220.82142	-2.36739	13.4	0.9	0.8	1.4	432.	1176.	64.0
194	220.84033	-0.33599	24.5	0.8	1.8	3.1	873.	2079.	123.7
195	220.85550	-2.01005	9.0	1.0	0.5	0.9	144.	917.	21.6
196	220.86121	-2.23778	33.7	1.4	2.7	4.4	981.	9584.	132.4
197	221.00045	-1.86797	8.4	1.2	0.4	0.8	98.	1145.	14.7
198	221.02278	-2.15159	35.6	1.3	2.9	6.9	2433.	12875.	325.0
199	221.10790	-2.06077	34.0	1.6	2.7	7.0	1417.	19366.	191.2
200	221.19192	-1.82072	7.9	1.3	0.4	0.8	132.	1506.	19.9
201	221.21485	-1.67292	8.3	1.4	0.4	0.7	145.	1425.	21.9
202	221.29949	-1.51836	9.6	1.0	0.5	1.2	179.	1371.	26.9
203	221.32065	-1.86544	36.5	0.5	3.0	6.4	914.	1910.	121.7
204	221.43579	-2.24274	39.0	0.9	3.3	5.8	6760.	5322.	885.3
205	221.51510	-2.01515	36.4	1.6	3.0	8.0	1626.	20661.	216.6
206	221.58965	-1.71627	34.3	1.5	2.7	3.0	747.	7316.	100.8
207	221.64320	-1.93632	40.2	1.3	3.4	8.0	9524.	13011.	1239.4
208	221.66099	-0.65995	25.1	2.7	1.8	2.9	699.	21336.	99.0
209	221.66236	-2.17210	38.1	1.4	3.2	7.3	6080.	14427.	802.1
210	221.85319	-1.49250	17.2	1.0	1.1	1.9	408.	1775.	59.7
211	221.88716	-2.03011	40.0	1.1	3.4	8.8	47071.	11043.	6138.4
212	221.94101	-1.18234	21.4	1.1	1.5	2.9	706.	3945.	101.6
213	222.04347	-0.46200	18.4	0.9	1.2	1.4	128.	1086.	18.7
214	222.13298	-1.65963	17.6	0.9	1.2	2.6	743.	2100.	108.5
215	222.14348	-1.25561	20.6	0.9	1.4	3.8	1415.	3079.	204.3
216	222.15225	-2.23575	38.7	1.2	3.2	10.6	35038.	16903.	4613.9
217	222.17169	-1.42468	19.4	1.0	1.3	4.0	717.	4469.	104.1
218	222.17464	-0.50214	16.5	0.6	1.1	2.2	468.	721.	68.6
219	222.26914	-2.39338	16.1	0.8	1.0	1.2	210.	823.	30.9
220	222.28893	-1.74660	20.2	1.4	1.4	2.0	354.	4065.	51.1
221	222.38925	-0.57429	17.8	1.3	1.2	3.0	313.	5431.	45.8
222	222.41979	-1.50987	17.9	1.2	1.2	4.5	787.	6976.	114.9
223	222.45446	-0.23248	51.1	0.9	4.7	5.7	3606.	4721.	434.4
224	222.47657	-0.40751	16.2	1.0	1.0	2.7	639.	2742.	93.8
225	222.55848	-2.00582	15.3	1.3	1.0	1.9	323.	3287.	47.5
226	222.59226	-1.65167	17.8	0.9	1.2	2.8	1503.	2238.	219.6
227	222.62328	-1.60328	42.4	1.3	3.6	3.9	6567.	6525.	845.8
228	222.71451	-0.65952	16.6	1.0	1.1	3.4	770.	3844.	113.0
229	222.76605	-0.37975	16.1	1.0	1.0	2.6	1378.	2691.	202.4
230	222.80675	-1.60301	17.9	1.1	1.2	4.1	3314.	5337.	484.0
231	222.86894	-1.86472	39.4	1.5	3.2	7.2	1854.	17842.	243.7
232	222.88445	-2.01860	38.8	1.3	3.2	7.0	7979.	12375.	1053.3

TABLE 2—*Continued*

ID	ℓ [°]	b [°]	v_{lsr} [km s^{-1}]	σ_v [km s^{-1}]	d [kpc]	r [pc]	M [$M_\odot$]	M_{vir} [$M_\odot$]	L [K km s^{-1} pc^2]
233	222.89596	-1.60599	41.9	1.2	3.5	4.1	4531.	6365.	586.4
234	222.91114	-1.02965	15.9	1.1	1.0	1.5	80.	1778.	11.8
235	222.94071	-0.49868	15.1	0.6	0.9	2.5	407.	872.	60.0
236	222.95052	-1.51563	12.8	1.1	0.7	1.1	155.	1412.	23.0
237	222.95085	-0.38800	12.7	1.0	0.7	1.4	275.	1394.	40.8
238	222.97828	-0.36949	17.4	0.9	1.1	3.0	1167.	2454.	170.8
239	222.98334	-0.61279	58.6	0.6	5.7	8.4	3511.	3351.	396.4
240	223.02400	-1.33220	13.2	0.8	0.8	1.5	274.	1065.	40.6
241	223.02604	-1.47150	18.5	0.9	1.2	3.3	1233.	2679.	179.7
242	223.04577	-2.21752	15.7	1.2	1.0	2.9	438.	4517.	64.4
243	223.08384	-1.81147	40.9	0.8	3.4	6.4	2759.	4361.	359.7
244	223.10717	-0.84201	15.4	0.9	1.0	3.2	1845.	2620.	272.0
245	223.11403	-1.87932	17.9	1.1	1.2	3.4	2839.	3989.	414.7
246	223.12868	-0.39210	14.0	1.0	0.8	1.6	404.	1583.	59.8
247	223.15225	-0.17586	13.2	1.2	0.8	1.4	189.	2283.	28.1
248	223.16135	-0.57153	14.9	0.9	0.9	1.9	372.	1720.	54.9
249	223.25247	-1.67840	39.9	1.1	3.3	5.4	2652.	7355.	348.2
250	223.26401	-0.33130	15.4	1.3	1.0	2.3	256.	4055.	37.8
251	223.27004	-1.78248	38.8	0.8	3.1	4.6	1825.	3325.	241.4
252	223.30090	-2.18953	19.5	1.6	1.3	4.9	935.	12393.	135.8
253	223.37318	-1.80454	18.1	1.1	1.2	2.9	4904.	3619.	715.9
254	223.43536	-0.61934	13.1	0.9	0.8	2.1	421.	1911.	62.6
255	223.46962	-0.92311	15.9	1.1	1.0	3.0	2036.	3562.	299.7
256	223.50709	-2.04035	17.1	1.1	1.1	2.5	1860.	3317.	272.5
257	223.51112	-2.06330	12.4	1.2	0.7	2.0	208.	3114.	31.0
258	223.57972	-2.34839	18.6	1.0	1.2	1.9	172.	1882.	25.1
259	223.62754	-1.83456	17.8	1.2	1.1	2.8	5876.	4133.	859.2
260	223.62901	-2.19556	11.4	1.9	0.6	0.7	35.	2614.	5.2
261	223.68933	-2.15481	16.8	1.4	1.1	1.2	228.	2596.	33.4
262	223.72345	-0.52264	12.2	2.0	0.7	1.8	38.	7317.	5.7
263	223.73529	-0.09304	15.4	0.5	1.0	1.3	113.	330.	16.6
264	223.74755	-1.97876	16.9	1.1	1.1	2.4	2976.	2796.	436.5
265	223.74931	-0.81232	13.5	1.5	0.8	2.5	1680.	5411.	249.3
266	223.76004	-2.01628	63.3	1.0	6.3	10.7	14505.	12030.	1570.3
267	223.81334	-0.61099	14.1	1.5	0.8	2.4	218.	5438.	32.2
268	223.84369	-0.09735	51.8	1.1	4.6	6.4	2904.	7427.	351.4
269	223.86839	-1.53879	19.2	1.1	1.3	2.2	1914.	2818.	278.4
270	223.88749	-0.49225	14.4	1.7	0.9	1.4	109.	4250.	16.1
271	223.90961	-1.86607	17.7	1.1	1.1	2.7	6299.	3240.	921.5
272	223.94819	-2.31370	14.7	1.0	0.9	1.2	63.	1261.	9.2
273	223.94945	-0.96932	42.9	0.9	3.6	4.7	1487.	3598.	192.2
274	223.96870	-0.07250	11.3	0.7	0.6	0.5	41.	283.	6.2
275	224.01014	-1.17245	15.1	1.0	0.9	2.8	3807.	3187.	562.0
276	224.02807	-1.70343	17.4	1.3	1.1	3.0	2434.	5476.	356.6
277	224.09656	-0.11342	15.3	0.8	0.9	1.7	283.	1112.	41.8
278	224.10830	-0.87756	13.3	1.4	0.8	2.4	2738.	4954.	406.6
279	224.16174	-1.93486	17.8	1.5	1.1	2.9	9700.	6698.	1418.7
280	224.18161	-1.64760	21.7	1.2	1.5	3.4	1383.	4749.	199.4
281	224.18974	-0.56697	12.6	1.2	0.7	2.6	542.	3862.	80.7
282	224.20744	-0.30617	14.4	1.2	0.9	2.8	533.	3991.	78.9
283	224.27956	-1.03729	14.3	1.6	0.9	1.9	2159.	4838.	319.7
284	224.29481	-2.15138	16.7	1.3	1.1	2.3	2776.	4290.	407.6
285	224.38363	-1.97467	17.1	1.3	1.1	2.5	5231.	4636.	767.1
286	224.42319	-0.71043	15.1	1.5	0.9	3.5	6564.	8356.	969.5
287	224.44950	-1.22910	15.3	0.9	0.9	1.9	649.	1607.	95.7
288	224.45196	-2.37347	9.6	1.1	0.5	0.6	255.	643.	38.3
289	224.46809	-1.68803	14.8	2.3	0.9	2.5	320.	14214.	47.3
290	224.48688	-0.10934	15.5	1.8	0.9	2.8	459.	9218.	67.7

C. List of Herschel sources

TABLE 2—*Continued*

ID	ℓ [°]	b [°]	v_{lsr} [km s^{-1}]	σ_v [km s^{-1}]	d [kpc]	r [pc]	M [$M_\odot$]	M_{vir} [$M_\odot$]	L [K km s^{-1} pc^2]
291	224.49204	-2.14882	15.1	1.4	0.9	2.5	133.	4820.	19.7
292	224.54490	-2.14914	18.2	0.8	1.2	2.1	361.	1417.	52.7
293	224.58083	-0.96230	16.5	1.1	1.0	3.2	2881.	3944.	423.5
294	224.58199	-1.52493	15.6	0.9	1.0	2.3	406.	1918.	59.8
295	224.59567	-0.38858	16.0	1.6	1.0	3.7	4324.	10140.	636.8
296	224.61948	-1.85638	18.8	1.2	1.2	4.1	1701.	6079.	248.0
297	224.65739	-1.32624	16.8	0.9	1.1	2.4	610.	1798.	89.6
298	224.67817	-2.01929	16.1	0.9	1.0	1.9	313.	1639.	46.1
299	224.72063	-0.96201	17.7	1.1	1.1	3.0	946.	3740.	138.6
300	224.73413	-1.71988	16.5	1.4	1.0	3.0	3720.	5979.	546.9
301	224.74864	-0.15232	13.0	0.9	0.7	3.6	174.	2951.	25.9
302	224.81018	-1.56172	16.9	0.8	1.1	4.2	118.	2522.	17.3
303	224.81874	-0.84184	18.6	1.2	1.2	3.0	192.	4308.	28.0
304	224.83916	-1.49400	18.7	1.3	1.2	3.4	736.	5640.	107.3
305	224.85275	-0.41591	15.7	1.5	1.0	2.9	2919.	6942.	430.4
306	224.92372	-1.15640	12.7	0.6	0.7	2.1	324.	689.	48.2
307	224.92913	-1.17375	9.8	1.0	0.5	1.2	68.	1155.	10.2
308	225.05476	-0.20742	17.0	1.0	1.1	3.1	1894.	3097.	278.1
309	225.06605	-0.59853	15.5	1.5	0.9	2.5	1095.	6073.	161.6
310	225.15878	-0.74363	19.7	0.9	1.3	2.5	437.	2220.	63.6
311	225.19247	-0.33050	15.0	0.8	0.9	2.4	567.	1669.	83.8
312	225.24214	-1.07539	13.9	0.8	0.8	1.9	649.	1310.	96.2
313	225.25760	-0.33575	17.1	0.7	1.1	2.4	1076.	1323.	158.0
314	225.26637	-0.91563	14.7	0.8	0.9	2.2	829.	1584.	122.6
315	225.27990	-1.34988	13.4	1.1	0.8	1.5	142.	1794.	21.2
316	225.31169	-0.55449	17.3	1.3	1.1	2.6	1790.	4904.	262.7
317	225.34649	-0.11049	17.6	1.1	1.1	2.3	1116.	2962.	163.5
318	225.37235	-0.51791	11.8	0.8	0.6	0.8	55.	602.	8.1
319	225.42389	-0.23851	15.7	1.1	1.0	2.0	1025.	2284.	151.2
320	225.43577	-0.97221	10.7	0.9	0.6	1.1	67.	903.	10.0
321	225.44266	-0.38711	17.5	1.0	1.1	1.8	883.	1842.	129.5

Table 3

List of the analyzed Hi-GAL sources

ID	ℓ [°]	b [°]	d [kpc]	$F_{70} \pm \Delta F_{70}$ [Jy]	$F_{160} \pm \Delta F_{160}$ [Jy]	$F_{250} \pm \Delta F_{250}$ [Jy]	$F_{350} \pm \Delta F_{350}$ [Jy]	$F_{500} \pm \Delta F_{500}$ [Jy]	r [″]	M [$M_\odot$]	T [K]	F_{22} [Jy]	L_{bol} [$L_\odot$]	unbound/pre-/proto-stellar 0/1/2
1	216.66360	-1.66179	2.6	···	···	0.43± 0.04	0.28± 0.02	0.17± 0.03	21.0	6.4	11.9	···	0.4	1
2	216.68802	-1.42173	2.6	···	···	0.29± 0.07	0.29± 0.01	0.12± 0.02	13.6	5.9	11.5	···	0.3	1
3	216.69028	-1.37625	2.6	···	···	0.31± 0.09	0.27± 0.02	0.23± 0.01	21.9	17.5	9.3	···	0.4	1
4	216.69757	-1.41449	2.6	···	···	0.89± 0.07	0.79± 0.01	0.51± 0.05	31.0	33.4	10.1	···	1.1	1
5	216.74443	-0.39604	2.1	···	···	0.46± 0.11	0.52± 0.01	0.27± 0.04	25.6	13.4	9.9	···	0.4	1
6	216.78496	-1.06081	2.6	0.87± 0.03	2.45± 0.12	3.99± 0.15	2.61± 0.02	1.36± 0.01	16.2	53.1	12.1	0.01	17.2	2
7	216.78586	-1.04352	2.6	24.01± 0.14	26.32± 0.24	20.11± 0.18	8.66± 0.02	3.61± 0.01	19.4	55.6	18.1	3.18	322.1	2
8	216.79010	-1.33692	2.7	···	···	0.35± 0.06	0.30± 0.01	0.19± 0.01	16.7	12.2	10.4	···	0.4	1
9	216.82965	-1.30140	2.7	···	···	0.62± 0.05	0.39± 0.01	0.22± 0.02	17.7	8.0	12.6	···	0.6	1
10	216.84781	-1.32426	2.7	···	···	0.83± 0.10	0.66± 0.02	0.36± 0.03	23.0	18.8	11.3	···	1.0	1
11	216.85027	-1.54283	2.6	···	···	0.14± 0.03	0.20± 0.01	0.10± 0.02	15.1	8.8	9.3	···	0.2	1
12	216.94028	-1.58797	5.1	···	···	0.15± 0.05	0.14± 0.01	0.07± 0.01	10.5	14.3	11.0	···	0.7	1
13	216.99194	-1.31877	2.4	···	···	0.31± 0.07	0.27± 0.02	0.16± 0.01	20.9	7.5	10.7	···	0.3	1
14	217.01163	-0.11884	1.5	1.32± 0.04	2.90± 0.10	3.37± 0.14	1.87± 0.02	0.73± 0.02	13.2	6.4	14.6	0.02	6.6	2
15	217.02290	-0.12783	1.5	···	···	0.63± 0.04	0.67± 0.02	0.48± 0.02	21.6	13.7	9.2	···	0.3	1
16	217.03499	-1.61789	5.1	···	···	0.53± 0.04	0.42± 0.01	0.24± 0.01	19.4	47.1	11.0	···	2.2	1
17	217.05092	-0.72714	2.0	···	···	0.84± 0.06	0.58± 0.01	0.40± 0.02	20.9	11.2	10.9	···	0.5	1
18	217.06100	-1.71599	1.9	0.38± 0.03	0.40± 0.06	0.28± 0.06	0.11± 0.01	···	11.0	0.3	19.9	0.01	2.2	2
19	217.06459	-1.61942	5.1	···	···	0.34± 0.06	0.26± 0.01	0.17± 0.02	13.9	35.2	10.7	···	1.4	1
20	217.06668	-0.71351	2.0	···	···	0.58± 0.05	0.31± 0.01	0.29± 0.02	15.3	6.0	11.2	···	0.3	1
21	217.09753	-1.62461	5.1	···	···	0.12± 0.11	0.15± 0.01	0.08± 0.02	14.8	27.0	9.5	···	0.7	1
22	217.12683	-1.57470	5.1	···	···	0.54± 0.08	0.48± 0.01	0.22± 0.04	19.5	40.1	11.6	···	2.3	1
23	217.13768	-1.53865	5.1	1.02± 0.05	1.18± 0.07	0.94± 0.10	0.42± 0.01	0.13± 0.01	9.5	8.6	18.6	0.03	43.3	2
24	217.14229	-1.39884	5.3	0.48± 0.02	0.53± 0.06	0.65± 0.11	0.66± 0.03	0.29± 0.05	14.6	49.7	12.0	0.07	31.3	2
25	217.16275	-1.23764	5.8	0.43± 0.02	0.34± 0.05	0.26± 0.09	0.14± 0.01	···	13.6	5.0	16.8	···	12.4	2
26	217.16357	-1.83950	2.8	···	···	0.28± 0.04	0.27± 0.01	0.20± 0.01	19.9	17.9	9.4	···	0.4	1
27	217.16840	-0.04018	2.1	···	···	1.36± 0.09	0.77± 0.02	0.60± 0.01	20.7	14.5	11.6	···	0.8	1
28	217.17271	-1.35582	5.3	···	···	0.42± 0.24	0.53± 0.01	0.42± 0.02	27.3	216.3	8.4	···	3.0	1
29	217.17929	-0.05392	2.1	···	···	0.94± 0.12	1.53± 0.01	1.10± 0.02	28.6	112.6	8.0	···	1.2	1
30	217.19145	-1.49453	2.7	1.05± 0.03	3.79± 0.15	4.73± 0.18	2.53± 0.01	1.30± 0.03	25.3	40.8	13.6	0.07	26.6	2
31	217.19412	-0.51546	2.1	···	···	0.20± 0.04	0.15± 0.01	0.10± 0.01	17.1	3.7	10.6	···	0.1	1
32	217.20294	-0.59034	2.1	···	···	1.09± 0.07	0.92± 0.01	0.56± 0.01	22.1	21.1	10.5	···	0.8	1
33	217.21700	-1.48283	4.7	···	···	1.70± 0.13	0.97± 0.02	0.40± 0.02	23.2	29.0	15.4	···	4.4	1
34	217.22528	-0.26994	1.1	···	···	1.24± 0.09	1.42± 0.01	1.07± 0.02	26.0	19.6	8.8	···	0.3	1
35	217.23386	-0.25371	1.1	0.35± 0.02	0.43± 0.06	1.25± 0.07	1.72± 0.01	···	21.4	22.0	8.8	0.10	1.5	2
36	217.23518	-0.24417	1.1	···	···	2.38± 0.29	2.12± 0.01	1.52± 0.02	25.7	19.1	9.8	···	0.5	1
37	217.24686	-0.23750	1.1	···	···	1.24± 0.18	1.59± 0.01	0.86± 0.02	22.8	13.9	9.4	···	0.3	1
38	217.25539	-0.21553	1.1	0.81± 0.03	0.74± 0.06	1.19± 0.12	0.93± 0.02	0.38± 0.01	14.8	3.0	12.1	0.20	2.4	2
39	217.26141	-1.46862	4.7	1.76± 0.06	3.36± 0.10	3.80± 0.14	2.38± 0.01	1.04± 0.02	20.1	97.7	13.9	0.18	98.5	2
40	217.26904	-1.36247	5.1	0.68± 0.04	2.50± 0.12	1.25± 0.12	0.75± 0.02	0.27± 0.01	16.2	14.5	18.9	0.02	48.0	2
41	217.27194	-0.34158	1.1	···	···	0.50± 0.11	0.40± 0.01	0.38± 0.01	12.4	4.6	9.4	···	0.1	1
42	217.27429	-0.36459	1.1	···	···	0.78± 0.09	0.59± 0.01	0.57± 0.02	31.7	6.5	9.5	···	0.2	1
43	217.29121	-1.31510	5.1	0.23± 0.04	0.63± 0.09	0.86± 0.15	0.51± 0.01	0.47± 0.01	10.4	44.8	12.3	0.02	19.0	2
44	217.30083	-1.12665	2.5	···	···	1.28± 0.11	0.75± 0.03	0.47± 0.05	33.3	14.7	12.3	···	1.1	1

TABLE 3—*Continued*

ID	ℓ [°]	b [°]	d [kpc]	$F_{70} \pm \Delta F_{70}$ [Jy]	$F_{160} \pm \Delta F_{160}$ [Jy]	$F_{250} \pm \Delta F_{250}$ [Jy]	$F_{350} \pm \Delta F_{350}$ [Jy]	$F_{500} \pm \Delta F_{500}$ [Jy]	r [″]	M [$M_\odot$]	T [K]	F_{22} [Jy]	L_{bol} [$L_\odot$]	unbound/pre-/proto-stellar 0/1/2
45	217.30141	-0.05822	2.1	27.95± 0.20	36.45± 0.22	31.76± 0.25	15.53± 0.02	6.53± 0.01	21.6	84.3	16.3	9.90	344.0	2
46	217.30147	-1.32625	5.1	···	0.82± 0.08	1.20± 0.09	1.05± 0.01	0.84± 0.01	16.9	133.9	10.9	0.01	20.3	2
47	217.30151	-1.78669	2.8	···	···	0.47± 0.05	0.52± 0.02	0.31± 0.02	19.8	28.4	9.6	···	0.8	1
48	217.30252	-0.03870	2.1	···	4.39± 0.17	9.50± 0.28	7.82± 0.02	4.27± 0.01	19.9	163.9	10.7	0.32	28.7	2
49	217.30620	-0.04772	2.1	15.24± 0.14	22.90± 0.21	21.77± 0.35	17.66± 0.02	6.64± 0.02	24.8	128.7	13.9	0.31	127.6	2
50	217.31033	-0.21533	1.1	···	···	0.36± 0.07	0.37± 0.02	0.25± 0.03	25.5	3.6	9.5	···	0.1	1
51	217.31052	-0.28071	1.1	···	···	2.28± 0.10	1.58± 0.01	0.94± 0.03	26.6	7.2	11.6	···	0.4	1
52	217.31207	-1.38271	5.1	2.12± 0.11	5.52± 0.26	6.61± 0.17	3.78± 0.01	···	20.8	187.4	14.0	0.28	169.7	2
53	217.31659	-1.37286	5.1	···	···	10.10± 0.20	6.08± 0.01	2.74± 0.02	24.2	240.3	14.8	···	33.0	1
54	217.31665	-1.33835	5.1	···	4.47± 0.22	5.46± 0.16	3.13± 0.02	···	24.7	162.2	13.8	0.08	99.1	2
55	217.31862	-0.30418	1.1	···	···	0.93± 0.07	0.73± 0.01	0.56± 0.01	21.6	5.4	10.1	···	0.2	1
56	217.32750	-1.36968	5.1	8.43± 0.14	18.17± 0.33	21.88± 0.20	13.75± 0.01	6.35± 0.01	16.9	728.5	13.6	0.42	553.9	2
57	217.33861	-0.23874	1.1	···	···	0.71± 0.09	0.58± 0.02	0.32± 0.03	32.4	2.9	11.1	···	0.1	1
58	217.33931	-1.36862	5.1	1.10± 0.05	···	10.16± 0.19	7.94± 0.01	···	22.7	585.4	12.1	0.32	158.1	2
59	217.34460	-1.37803	5.1	4.88± 0.13	5.39± 0.16	4.23± 0.09	1.93± 0.01	···	13.3	49.9	17.7	0.23	217.6	2
60	217.35243	-1.43530	4.7	···	···	3.10± 0.34	1.68± 33.58	0.71± 0.04	32.9	49.1	15.7	···	7.9	1
61	217.35413	-1.41616	5.1	···	···	1.82± 0.09	1.24± 0.01	0.64± 0.01	22.6	92.5	12.3	···	6.7	1
62	217.35962	-1.32541	5.1	0.43± 0.03	0.51± 0.07	0.64± 0.11	0.40± 0.01	···	8.4	22.7	13.3	0.02	21.1	2
63	217.36540	-1.33517	5.1	0.56± 0.03	0.84± 0.07	1.62± 0.12	1.09± 0.02	···	20.4	103.2	11.6	0.02	32.7	2
64	217.37611	-0.08454	2.1	827.64± 1.66	319.99± 0.64	222.51± 0.89	87.32± 0.00	33.92± 0.00	25.4	310.9	19.3	474.50	9679.4	2
65	217.47652	-0.04724	1.8	2.61± 0.05	3.76± 0.13	3.39± 0.18	2.49± 0.03	0.75± 0.03	10.7	8.9	15.4	0.88	23.9	2
66	217.47820	-0.18994	2.1	···	···	0.81± 0.07	0.68± 0.01	0.55± 0.02	21.1	25.0	9.6	···	0.7	1
67	217.49167	-0.08088	1.8	1.27± 0.05	2.48± 0.12	5.59± 0.20	3.20± 0.01	···	17.1	38.8	11.6	···	8.7	2
68	217.49518	-0.07074	1.8	8.64± 0.11	17.84± 0.27	17.70± 0.18	10.09± 0.01	4.40± 0.03	21.4	51.2	14.8	1.07	73.8	2
69	217.50027	-0.20677	2.1	···	···	0.68± 0.08	0.86± 0.02	0.44± 0.01	19.5	24.2	9.5	···	0.6	1
70	217.52646	-0.07732	1.8	···	···	1.94± 0.18	1.86± 0.02	1.11± 0.03	25.1	36.3	10.1	···	1.2	1
71	217.57440	-0.09783	1.8	···	···	1.64± 0.16	1.05± 0.01	0.56± 0.04	28.2	9.4	12.6	···	0.7	1
72	217.60297	-0.05246	1.8	···	···	0.98± 0.15	0.51± 0.01	0.28± 0.02	24.8	3.4	14.0	···	0.4	1
73	217.62495	-0.15439	2.1	2.46± 0.22	3.77± 0.12	7.61± 0.27	3.48± 0.03	1.36± 0.03	28.1	26.4	13.6	0.22	26.3	2
74	217.62689	-0.18399	2.1	49.31± 0.30	40.47± 0.24	35.20± 0.28	14.31± 0.01	5.91± 0.02	24.8	64.3	17.5	11.56	461.0	2
75	217.63626	-0.13185	2.1	···	···	0.55± 0.12	0.65± 0.01	0.34± 0.01	13.9	17.4	9.7	···	0.5	1
76	217.65610	-0.19365	2.1	9.23± 0.15	10.97± 0.19	4.72± 0.12	1.99± 0.01	0.87± 0.02	18.4	4.9	22.7	0.64	69.8	2
77	217.69716	-0.23935	1.6	···	···	1.30± 0.11	0.97± 0.01	0.57± 0.02	30.9	10.4	11.3	···	0.5	1
78	217.69861	-0.20510	2.1	···	···	1.64± 0.19	1.09± 0.01	0.66± 0.03	28.5	16.8	11.8	···	1.0	1
79	217.72137	-0.16784	2.1	···	···	0.58± 0.09	0.32± 0.01	0.15± 0.01	16.5	2.3	14.6	···	0.3	0
80	217.73511	-0.69747	2.3	···	···	0.33± 0.08	0.31± 0.02	0.20± 0.01	19.5	11.1	9.9	···	0.3	1
81	217.76306	-1.90009	2.9	···	···	0.86± 0.05	0.65± 0.01	0.47± 0.01	21.1	31.0	10.4	···	1.2	1
82	217.79570	-1.88198	2.9	4.20± 0.06	3.75± 0.09	3.09± 0.19	2.52± 0.02	1.05± 0.02	16.9	33.6	14.0	0.66	69.7	2
83	217.79695	-0.13617	2.1	···	···	0.73± 0.07	0.53± 0.02	0.34± 0.04	23.5	9.9	11.1	···	0.5	1
84	217.80267	-0.28371	1.6	···	···	0.39± 0.06	0.26± 0.01	0.13± 0.02	15.1	1.7	12.9	···	0.1	1
85	217.83006	-0.18935	2.1	···	···	0.37± 0.09	0.53± 0.01	0.34± 0.02	19.1	25.0	8.6	···	0.4	1
86	217.84331	-1.81442	2.1	···	···	0.28± 0.04	0.23± 0.02	0.12± 0.02	17.7	3.5	11.4	···	0.2	1
87	217.84694	-0.25950	2.1	···	···	1.55± 0.09	1.31± 0.02	0.74± 0.02	21.6	25.4	10.8	···	1.1	1
88	217.86577	-1.90944	2.1	···	0.57± 0.03	0.10± 0.05	0.05± 0.01	···	6.3	0.0	43.8	0.01	1.3	2

TABLE 3—*Continued*

ID	ℓ [°]	b [°]	d [kpc]	$F_{70} \pm \Delta F_{70}$ [Jy]	$F_{160} \pm \Delta F_{160}$ [Jy]	$F_{250} \pm \Delta F_{250}$ [Jy]	$F_{350} \pm \Delta F_{350}$ [Jy]	$F_{500} \pm \Delta F_{500}$ [Jy]	r [″]	M [$M_\odot$]	T [K]	F_{22} [Jy]	L_{bol} [$L_\odot$]	unbound/pre-/proto-stellar 0/1/2
89	217.87485	-1.83482	2.1	···	···	0.28± 0.04	0.25± 0.01	0.12± 0.03	21.0	4.3	11.1	···	0.2	1
90	217.88361	-0.27692	2.3	···	···	0.87± 0.13	0.63± 0.01	0.37± 0.02	27.6	12.1	11.6	···	0.7	1
91	217.88567	-0.18413	2.3	···	···	1.07± 0.07	0.98± 0.02	0.59± 0.04	21.6	28.7	10.2	···	1.0	1
92	217.89963	-0.29547	2.3	0.49± 0.02	0.61± 0.09	0.92± 0.13	0.63± 0.02	0.36± 0.03	16.3	10.5	12.0	0.02	5.0	2
93	217.91693	-1.88418	2.7	···	···	0.42± 0.04	0.40± 0.01	0.26± 0.01	17.8	19.5	9.9	···	0.6	1
94	217.91704	-0.29507	2.3	···	···	0.89± 0.08	0.76± 0.01	0.46± 0.02	18.5	20.7	10.5	···	0.8	1
95	217.91763	-1.81642	2.1	···	···	0.27± 0.05	0.31± 0.02	0.24± 0.02	20.7	15.4	8.7	···	0.3	1
96	217.92119	-0.26952	2.3	···	···	1.27± 0.11	0.97± 0.02	0.65± 0.02	30.1	26.7	10.6	···	1.1	1
97	217.92220	-0.24550	2.3	···	···	2.26± 0.14	1.43± 0.04	0.81± 0.02	36.5	22.5	12.3	···	1.6	1
98	217.94304	-0.28449	2.3	···	···	2.19± 0.12	1.72± 0.02	0.95± 0.04	30.0	37.1	11.1	···	1.8	1
99	217.95029	-0.29615	2.3	···	···	1.02± 20.42	1.24± 0.01	0.96± 0.01	18.2	81.7	8.6	···	1.3	1
100	217.95697	-0.49270	2.1	···	···	1.11± 0.54	0.67± 0.01	0.39± 0.02	23.9	8.7	12.5	···	0.6	1
101	217.95921	-0.12667	2.1	···	···	0.52± 0.05	0.29± 0.02	0.21± 0.02	20.5	4.6	12.1	···	0.3	1
102	217.96873	-1.82791	2.7	···	···	0.21± 0.06	0.19± 0.02	0.10± 0.02	15.0	5.2	11.1	···	0.3	1
103	217.99861	-0.31560	2.3	···	···	2.82± 0.23	5.10± 0.01	3.36± 0.02	28.1	315.2	8.3	···	4.5	1
104	218.01694	-1.95616	2.0	···	···	0.58± 0.05	0.47± 0.01	0.24± 0.03	17.7	6.5	11.4	···	0.3	1
105	218.01711	-1.87673	2.7	···	···	0.46± 0.09	0.30± 0.03	0.15± 0.02	23.1	5.4	12.8	···	0.5	1
106	218.01738	-0.48248	1.5	···	···	0.94± 0.06	0.64± 0.02	0.32± 0.02	17.3	4.1	12.5	···	0.3	1
107	218.02229	-0.31524	2.3	29.95± 0.21	34.01± 0.27	28.04± 0.14	13.74± 0.01	5.63± 0.01	18.1	79.5	16.7	2.90	299.4	2
108	218.03098	-0.26996	2.3	···	···	1.45± 0.11	1.03± 0.02	0.55± 0.03	28.5	16.5	12.0	···	1.1	1
109	218.03860	-1.81585	2.7	···	···	0.17± 0.07	0.25± 0.01	0.18± 0.01	15.1	27.9	8.1	···	0.3	1
110	218.04095	-0.32733	2.3	2.90± 0.08	6.37± 0.15	8.71± 0.15	6.04± 0.01	3.52± 0.01	19.4	91.1	12.3	0.12	39.0	2
111	218.04378	-0.48542	2.0	···	···	0.69± 0.11	0.55± 0.01	0.28± 0.01	21.1	7.4	11.6	···	0.4	1
112	218.05252	-0.11740	2.1	28.07± 0.20	45.77± 0.27	39.40± 0.43	20.01± 0.02	7.60± 0.02	17.6	104.2	16.4	3.16	289.2	2
113	218.06357	-0.32522	2.3	···	1.64± 0.13	3.62± 0.13	2.28± 0.01	2.13± 0.02	23.3	55.6	11.1	0.10	11.7	2
114	218.07256	-0.27425	2.3	0.79± 0.04	0.91± 0.06	1.26± 0.10	0.71± 0.01	···	13.9	8.2	13.3	0.01	6.8	2
115	218.07767	-0.28704	2.3	···	0.68± 0.07	1.69± 0.14	1.54± 0.01	0.78± 0.02	18.1	40.4	10.3	0.02	4.5	2
116	218.08118	-0.30117	2.3	1.17± 0.03	1.02± 0.17	3.43± 0.19	2.71± 0.02	1.63± 0.04	15.0	101.7	9.7	0.11	14.2	2
117	218.08861	-0.05262	2.1	···	···	0.69± 0.05	0.42± 0.01	0.30± 0.02	20.2	7.7	11.6	···	0.4	1
118	218.10060	-1.87255	2.2	···	···	0.63± 0.21	0.45± 0.02	0.28± 0.01	23.2	9.8	11.1	···	0.5	1
119	218.10332	-0.36435	1.5	42.69± 0.26	59.18± 0.36	56.90± 0.40	28.07± 0.03	10.93± 0.02	20.6	81.8	16.0	5.45	225.0	2
120	218.10861	-0.03431	2.1	···	···	0.38± 0.04	0.25± 0.01	0.18± 0.02	15.1	5.4	11.1	···	0.3	1
121	218.11208	-0.29306	2.3	0.89± 0.05	2.37± 0.11	4.02± 0.11	2.54± 0.03	1.65± 0.03	21.0	49.8	11.7	0.35	18.9	2
122	218.11674	-0.12198	2.1	···	···	1.10± 0.06	0.61± 0.01	0.38± 0.02	21.9	7.8	12.7	···	0.6	1
123	218.12117	-0.31474	1.5	0.56± 0.03	1.16± 0.07	4.36± 0.15	4.43± 0.01	2.71± 0.02	25.2	93.5	9.1	···	4.5	2
124	218.12663	-0.27104	2.3	···	···	1.16± 0.14	0.84± 0.02	0.49± 0.03	21.7	16.8	11.4	···	0.9	1
125	218.12708	-1.74818	2.2	···	0.40± 0.05	0.32± 0.09	0.17± 0.01	···	12.9	0.9	16.5	0.01	1.5	2
126	218.13034	-0.30450	1.5	···	···	3.32± 0.25	2.89± 0.01	1.53± 0.02	24.2	28.4	11.0	···	1.3	1
127	218.13336	-0.37784	2.3	···	···	5.26± 0.25	3.45± 0.02	1.75± 0.04	30.1	45.3	12.8	···	3.7	1
128	218.13341	-0.31053	1.5	0.40± 0.04	0.98± 0.13	2.36± 0.19	1.32± 0.01	···	17.7	13.0	11.3	0.06	3.4	2
129	218.13341	-0.51962	2.0	0.87± 0.04	2.39± 0.12	3.41± 0.15	2.19± 0.01	0.86± 0.01	13.9	17.0	13.3	0.18	11.9	2
130	218.13423	-1.43585	7.4	···	···	0.54± 0.04	0.42± 0.02	0.17± 0.17	24.8	48.7	13.0	···	4.3	1
131	218.13649	-0.53308	2.0	1.57± 0.05	1.52± 0.10	0.95± 0.10	0.55± 0.01	···	3.8	1.8	18.0	0.01	8.0	2
132	218.14186	-0.52209	2.0	0.46± 0.03	0.45± 0.07	1.83± 0.16	1.97± 0.01	1.06± 0.01	17.4	66.3	9.0	0.06	5.2	2

TABLE 3—*Continued*

ID	ℓ [°]	b [°]	d [kpc]	$F_{70} \pm \Delta F_{70}$ [Jy]	$F_{160} \pm \Delta F_{160}$ [Jy]	$F_{250} \pm \Delta F_{250}$ [Jy]	$F_{350} \pm \Delta F_{350}$ [Jy]	$F_{500} \pm \Delta F_{500}$ [Jy]	r [″]	M [$M_\odot$]	T [K]	F_{22} [Jy]	L_{bol} [$L_\odot$]	unbound/pre-/proto-stellar 0/1/2
133	218.14290	-1.89307	2.2	···	···	0.67± 0.07	0.54± 0.03	0.34± 0.04	28.6	13.5	10.6	···	0.5	1
134	218.14362	-0.28641	1.5	···	···	1.91± 0.32	1.37± 0.01	1.35± 0.02	25.5	28.1	9.7	···	0.8	1
135	218.14444	-0.18696	2.1	···	···	1.49± 0.06	1.12± 0.01	0.73± 0.01	17.7	25.1	10.8	···	1.1	1
136	218.14633	-0.56713	2.0	7.83± 0.11	10.85± 0.17	11.46± 0.25	7.11± 0.02	3.54± 0.01	20.5	54.0	13.9	3.90	96.6	2
137	218.14888	-0.33179	1.5	···	···	2.10± 0.21	1.56± 0.01	1.32± 0.21	19.5	25.1	10.1	···	0.8	1
138	218.15030	-0.64382	2.0	15.22± 0.17	16.92± 0.24	16.67± 0.17	8.73± 0.01	4.08± 0.03	21.0	52.7	15.1	1.31	113.8	2
139	218.15474	-0.40847	2.0	1.06± 0.04	1.52± 0.10	2.43± 0.10	1.38± 0.02	···	20.6	14.5	12.6	0.19	10.7	2
140	218.15652	-0.58218	2.0	8.55± 0.09	11.95± 0.20	11.13± 0.65	6.66± 0.02	3.20± 0.03	30.5	43.4	14.6	0.61	67.5	2
141	218.15736	-0.37530	2.3	···	2.04± 0.09	2.50± 0.19	1.60± 0.01	1.44± 0.01	18.2	27.0	12.3	0.03	9.0	2
142	218.15930	-0.18826	2.1	···	···	0.37± 0.08	0.40± 0.01	0.24± 0.01	15.6	12.4	9.7	···	0.3	1
143	218.16008	-0.34305	1.5	0.59± 0.04	1.53± 0.10	4.13± 0.17	2.92± 0.01	···	19.4	39.7	10.4	0.02	5.0	2
144	218.16364	-0.35937	1.5	0.55± 0.04	1.83± 0.09	6.03± 0.20	5.87± 0.01	3.29± 0.02	22.8	99.0	9.5	0.24	8.2	2
145	218.16907	-1.84870	2.2	···	···	0.45± 0.08	0.41± 0.02	0.27± 0.03	19.3	12.3	10.1	···	0.4	1
146	218.17120	-0.67295	2.0	···	···	8.16± 0.27	8.68± 0.02	4.78± 0.03	21.1	194.5	10.0	···	6.2	1
147	218.17444	-0.63119	2.0	···	···	2.76± 0.12	3.03± 0.02	1.69± 0.01	19.2	74.2	9.8	···	2.1	1
148	218.17519	-0.37541	2.3	2.01± 0.05	7.74± 0.23	9.24± 0.21	4.66± 0.02	4.09± 0.02	28.5	63.2	13.3	0.10	36.2	2
149	218.17607	-0.50686	2.0	0.79± 0.04	1.59± 0.10	3.28± 0.15	2.60± 0.02	1.29± 0.01	19.1	39.1	11.1	0.10	9.7	2
150	218.18240	-0.58864	2.0	0.91± 0.05	1.32± 0.09	1.57± 0.15	0.92± 0.01	···	16.6	6.8	13.9	0.09	8.0	2
151	218.18529	-0.43450	2.0	···	···	0.58± 0.07	0.70± 0.01	0.39± 0.03	19.5	19.3	9.4	···	0.5	1
152	218.19066	-0.38409	2.3	1.10± 0.09	6.89± 0.13	13.48± 0.43	8.96± 0.03	3.99± 0.02	16.9	139.4	11.9	0.42	38.8	2
153	218.19389	-0.60201	2.0	2.36± 0.06	3.64± 0.14	3.92± 0.22	2.14± 0.01	0.92± 0.02	14.2	12.7	14.8	0.12	18.8	2
154	218.19931	-0.39083	2.0	17.48± 0.16	20.38± 0.14	13.10± 0.42	5.41± 0.02	···	25.5	13.1	20.5	1.92	131.9	2
155	218.20279	-0.31413	1.5	···	0.49± 0.07	1.18± 0.07	1.26± 0.02	0.84± 0.02	20.9	22.2	9.6	···	0.9	1
156	218.22362	-0.39818	2.0	···	2.10± 0.08	2.87± 0.16	1.66± 0.02	···	23.8	14.5	13.3	0.11	9.0	2
157	218.22694	-2.00283	2.0	···	···	0.27± 0.06	0.42± 0.01	0.24± 0.02	19.2	17.1	8.6	···	0.3	1
158	218.23599	-2.02763	2.8	···	···	1.15± 0.06	1.01± 0.02	0.62± 0.02	24.5	45.0	10.4	···	1.6	1
159	218.23843	-0.30095	2.1	···	1.41± 0.07	1.71± 0.09	1.18± 0.01	0.73± 0.02	23.0	15.2	12.6	0.05	6.4	2
160	218.24062	-0.39514	2.1	···	0.87± 0.09	1.54± 0.09	0.87± 0.01	···	22.8	11.7	12.3	0.02	4.0	2
161	218.24518	-0.60239	2.0	···	···	3.19± 0.18	2.32± 0.03	1.38± 0.03	26.2	27.0	12.1	···	1.9	1
162	218.25404	-2.04922	2.8	···	0.60± 0.04	1.05± 0.09	1.01± 0.02	0.60± 0.01	18.7	38.8	10.6	···	2.8	1
163	218.25458	-0.35242	2.1	···	1.58± 0.06	2.08± 0.23	1.36± 0.02	0.70± 0.03	24.2	15.7	12.8	0.04	6.6	2
164	218.26382	-0.39015	2.1	···	···	2.13± 0.16	1.21± 0.02	0.58± 0.03	27.7	9.9	14.3	···	1.2	1
165	218.28824	-2.01099	2.0	···	···	0.93± 0.09	1.01± 0.01	0.70± 0.03	22.5	39.0	9.1	···	0.8	1
166	218.29642	-0.80482	2.3	···	···	0.31± 0.05	0.27± 0.01	0.13± 0.03	19.4	5.0	11.4	···	0.3	1
167	218.29813	-1.44999	7.4	···	···	0.25± 0.05	0.28± 0.02	0.17± 0.01	14.8	113.6	9.5	···	2.9	1
168	218.30522	-0.11718	2.2	···	···	1.04± 0.08	0.88± 0.02	0.70± 0.02	28.4	36.6	9.5	···	0.9	1
169	218.30528	-0.37284	2.1	···	···	0.56± 0.07	0.32± 0.02	0.18± 0.02	22.0	3.6	13.1	···	0.3	1
170	218.31230	-0.44349	2.1	···	···	1.25± 0.11	0.75± 0.02	0.39± 0.02	21.5	7.9	13.3	···	0.7	1
171	218.31528	-0.08900	2.2	···	···	1.07± 0.11	0.74± 0.02	0.56± 0.04	25.3	20.1	10.6	···	0.8	1
172	218.33670	-0.07875	2.2	···	···	1.77± 0.09	1.42± 0.03	0.91± 0.04	27.9	36.1	10.6	···	1.4	1
173	218.33705	-2.02509	2.0	···	···	0.65± 0.04	0.58± 0.01	0.42± 0.05	20.6	17.6	9.7	···	0.5	1
174	218.33766	-2.04468	2.1	···	···	0.41± 0.04	0.37± 0.01	0.25± 0.05	24.1	10.6	9.9	···	0.3	1
175	218.35033	-2.03794	2.1	0.43± 0.02	···	0.74± 0.09	0.49± 0.01	0.24± 0.04	9.7	5.2	12.8	0.04	4.2	2
176	218.36565	-1.11563	2.7	···	···	0.76± 1.12	0.71± 0.02	0.43± 0.03	25.1	31.1	10.1	···	1.0	1

TABLE 3—*Continued*

ID	ℓ [°]	b [°]	d [kpc]	$F_{70} \pm \Delta F_{70}$ [Jy]	$F_{160} \pm \Delta F_{160}$ [Jy]	$F_{250} \pm \Delta F_{250}$ [Jy]	$F_{350} \pm \Delta F_{350}$ [Jy]	$F_{500} \pm \Delta F_{500}$ [Jy]	r [″]	M [$M_\odot$]	T [K]	F_{22} [Jy]	L_{bol} [$L_\odot$]	unbound/pre-/proto-stellar 0/1/2
177	218.39359	-1.44219	7.5	···	···	0.24± 0.06	0.32± 0.01	0.25± 0.02	21.0	265.2	8.3	···	3.5	1
178	218.39362	-0.18950	2.2	···	···	0.38± 0.10	0.30± 0.02	0.21± 0.02	28.0	8.4	10.4	···	0.3	1
179	218.39891	-2.06174	2.1	···	···	0.57± 0.05	0.44± 0.01	0.20± 0.02	15.8	5.0	12.3	···	0.4	1
180	218.40973	-1.12670	2.7	···	···	0.43± 0.04	0.34± 0.01	0.20± 0.02	16.8	11.6	10.9	···	0.5	1
181	218.46768	-1.97681	2.1	···	···	0.59± 0.07	0.60± 0.03	0.38± 0.02	25.1	18.3	9.7	···	0.5	1
182	218.55058	-0.93413	1.6	···	···	0.20± 0.04	0.16± 0.01	0.11± 0.01	21.9	1.8	11.1	···	0.1	0
183	218.56168	-1.90193	2.7	···	0.60± 0.04	0.32± 0.05	0.16± 0.02	···	15.0	0.7	20.5	0.01	3.0	2
184	218.58128	-1.44798	2.4	···	···	0.29± 0.04	0.31± 0.02	0.24± 0.03	21.0	18.9	8.9	···	0.4	1
185	218.68935	-0.64691	2.5	···	···	0.42± 0.04	0.31± 0.03	0.10± 0.03	24.9	2.5	14.7	···	0.3	0
186	218.69077	-0.58594	2.1	···	···	0.19± 0.03	0.17± 0.01	0.11± 0.01	17.8	4.9	10.0	···	0.2	1
187	218.70361	-0.81409	2.5	···	···	0.54± 0.07	0.45± 0.02	0.28± 0.02	18.6	14.2	10.6	···	0.6	1
188	218.70598	-0.49142	5.8	···	···	0.55± 0.06	0.60± 0.01	0.38± 0.03	26.5	152.0	9.5	···	3.8	1
189	218.73402	-0.45868	5.8	···	0.37± 0.04	0.88± 0.06	0.81± 0.02	0.61± 0.02	19.7	203.7	9.8	0.01	17.4	2
190	218.74429	-0.44515	5.8	···	···	0.47± 0.06	0.43± 0.01	0.23± 0.01	11.2	55.6	11.1	···	2.7	1
191	218.76701	-1.78701	2.9	···	···	1.11± 0.06	1.28± 0.01	0.58± 0.05	22.6	48.5	10.4	···	1.8	1
192	218.76704	-0.42141	5.8	···	···	0.34± 0.05	0.40± 0.02	0.30± 0.05	24.1	152.1	8.8	···	2.7	1
193	218.78169	-0.44537	5.8	···	···	0.19± 0.09	0.18± 0.01	0.16± 0.02	16.1	71.7	8.9	···	1.3	1
194	218.80585	-0.38295	1.6	···	···	0.50± 0.10	0.41± 0.01	0.24± 0.01	15.8	5.1	10.8	···	0.2	1
195	218.84952	-1.55865	4.3	···	···	0.17± 0.02	0.16± 0.01	0.11± 0.01	15.1	19.7	9.9	···	0.6	1
196	218.91626	-1.72617	2.6	···	···	0.54± 0.03	0.34± 0.02	0.28± 0.01	21.6	12.4	10.8	···	0.5	1
197	218.98193	-1.28618	2.9	···	···	0.11± 0.04	0.07± 0.01	0.06± 0.02	15.4	3.6	10.5	···	0.1	1
198	219.22278	-1.08200	1.9	···	···	0.44± 0.05	0.43± 0.01	0.25± 0.02	25.4	8.9	10.2	···	0.3	1
199	219.23773	-1.11610	1.9	···	···	0.69± 0.05	0.38± 0.07	0.37± 0.02	26.0	7.2	11.1	···	0.4	1
200	219.31848	-1.08639	1.2	···	···	0.72± 0.06	0.37± 0.10	0.37± 0.02	20.2	2.3	11.5	···	0.1	1
201	219.33624	-1.12155	1.2	···	···	0.96± 0.11	0.88± 0.01	0.78± 0.02	23.7	13.0	9.1	···	0.3	1
202	219.33771	-1.10507	1.2	···	···	0.92± 0.05	0.94± 0.02	0.63± 0.01	17.9	10.1	9.5	···	0.3	1
203	219.35236	-1.13380	1.2	···	···	1.31± 0.16	1.35± 0.01	0.84± 0.02	30.1	13.0	9.7	···	0.4	1
204	219.40442	-1.26784	2.6	···	···	0.30± 0.02	0.25± 0.02	0.13± 0.02	16.9	6.9	11.1	···	0.3	1
205	219.54990	-0.80885	2.6	···	···	0.39± 0.04	0.25± 0.01	0.17± 0.01	17.9	7.1	11.5	···	0.4	1
206	219.57233	-1.57568	2.5	···	···	0.37± 0.05	0.29± 0.01	0.25± 0.02	20.3	14.8	9.7	···	0.4	1
207	219.66856	-1.34391	2.6	···	···	0.43± 0.04	0.41± 0.01	0.21± 0.04	24.5	11.8	10.7	···	0.5	1
208	219.67012	-1.90204	2.1	···	···	0.41± 0.02	0.27± 0.01	0.19± 0.03	21.8	5.4	11.1	···	0.3	1
209	219.72528	-1.30127	2.6	···	···	0.31± 0.06	0.28± 0.02	0.23± 0.03	19.9	17.2	9.3	···	0.4	1
210	219.81528	-0.83951	1.9	···	···	0.33± 0.03	0.23± 0.01	0.17± 0.01	19.8	4.2	10.8	···	0.2	1
211	219.85861	-0.95960	1.9	···	···	0.33± 0.06	0.33± 0.01	0.17± 0.01	20.0	6.7	10.1	···	0.2	1
212	219.91673	-1.95510	2.5	···	···	0.44± 0.11	0.33± 0.04	0.26± 0.02	22.0	13.1	10.2	···	0.4	1
213	220.08527	-2.02981	2.8	···	···	0.51± 0.05	0.37± 0.02	0.23± 0.02	21.0	12.3	11.2	···	0.6	1
214	220.10861	-0.61273	2.0	···	0.63± 0.07	1.36± 0.06	1.16± 0.01	0.74± 0.02	19.0	27.3	10.4	0.05	4.1	2
215	220.15361	-1.20618	2.7	···	···	0.25± 0.14	0.26± 0.01	0.15± 0.03	24.3	11.8	9.9	···	0.4	1
216	220.15628	-0.29484	2.4	···	···	0.46± 0.07	0.38± 0.01	0.25± 0.01	11.1	11.9	10.4	···	0.4	1
217	220.17960	-0.36337	2.4	···	···	0.71± 0.04	0.46± 0.01	0.32± 0.01	19.2	11.0	11.3	···	0.6	1
218	220.18361	-0.33092	2.4	···	···	1.41± 0.10	0.88± 0.02	0.52± 0.02	23.4	15.4	12.3	···	1.1	1
219	220.18413	-1.87562	2.7	···	···	0.50± 0.05	0.41± 0.01	0.25± 0.02	19.5	14.0	10.7	···	0.6	1
220	220.18965	-1.20219	2.7	···	···	0.40± 0.04	0.28± 0.02	0.14± 0.08	22.3	5.7	12.5	···	0.4	1

TABLE 3—*Continued*

ID	ℓ [°]	b [°]	d [kpc]	$F_{70} \pm \Delta F_{70}$ [Jy]	$F_{160} \pm \Delta F_{160}$ [Jy]	$F_{250} \pm \Delta F_{250}$ [Jy]	$F_{350} \pm \Delta F_{350}$ [Jy]	$F_{500} \pm \Delta F_{500}$ [Jy]	r [″]	M [$M_\odot$]	T [K]	F_{22} [Jy]	L_{bol} [$L_\odot$]	unbound/pre-/proto-stellar 0/1/2
221	220.20215	-0.34194	2.4	1.08± 0.04	0.98± 0.06	1.79± 0.04	1.21± 0.01	0.61± 0.03	19.6	22.0	11.8	0.49	17.8	2
222	220.20824	-0.16897	3.0	···	···	0.51± 0.03	0.32± 0.01	0.17± 0.02	25.4	7.0	13.0	···	0.6	1
223	220.25204	-1.91249	2.7	···	···	0.58± 0.07	0.43± 0.02	0.21± 0.01	16.0	9.8	11.8	···	0.6	1
224	220.27026	-1.76359	0.9	···	···	0.50± 0.09	0.41± 0.02	0.18± 0.02	20.9	0.9	12.1	···	0.1	0
225	220.29817	-1.71690	0.9	···	···	1.45± 0.08	1.24± 0.01	0.74± 0.03	26.7	5.4	10.1	···	0.2	1
226	220.30891	-1.78707	0.9	···	···	0.50± 0.23	0.84± 0.03	0.49± 0.02	26.4	7.2	8.4	···	0.1	1
227	220.31667	-1.74675	0.9	···	···	1.42± 0.10	1.19± 0.02	0.54± 0.03	34.2	2.7	11.9	···	0.2	1
228	220.32027	-1.89012	0.9	···	···	0.74± 0.18	0.52± 0.01	0.37± 0.02	25.3	1.8	11.1	···	0.1	1
229	220.32063	-1.95297	0.8	···	···	0.40± 0.07	0.30± 0.02	0.16± 0.03	20.9	0.6	11.9	···	0.0	0
230	220.32780	-1.76004	0.9	···	···	1.27± 0.09	1.16± 0.02	0.87± 0.03	30.3	7.6	9.5	···	0.2	1
231	220.33427	-1.89749	0.9	···	···	1.97± 0.19	1.61± 0.03	0.95± 0.05	33.7	5.7	10.8	···	0.2	1
232	220.36496	-1.96519	0.8	···	···	0.71± 0.09	0.75± 0.03	0.34± 0.03	23.1	1.9	10.7	···	0.1	1
233	220.37860	-1.78618	0.9	···	···	1.36± 0.09	1.02± 0.01	0.61± 0.03	30.7	3.5	11.1	···	0.2	1
234	220.38187	-1.97019	2.8	···	···	0.52± 0.07	0.30± 0.01	0.26± 0.05	18.9	11.4	11.1	···	0.6	1
235	220.39813	-1.90991	2.8	···	···	0.34± 0.04	0.33± 0.01	0.18± 0.01	16.8	12.7	10.4	···	0.5	1
236	220.42284	-0.58607	2.2	0.54± 0.05	···	0.79± 0.08	0.43± 0.01	···	25.2	2.5	16.2	0.04	5.6	2
237	220.45834	-0.60897	2.2	22.97± 0.18	26.19± 0.24	27.72± 0.22	12.02± 0.02	5.74± 0.02	20.2	91.3	15.5	6.60	293.1	2
238	220.46141	-0.60237	2.2	19.45± 0.18	21.09± 0.23	11.30± 0.15	5.29± 0.02	···	14.3	16.4	20.8	3.15	200.7	2
239	220.47417	-1.59828	0.9	···	···	0.36± 0.06	0.39± 0.02	0.24± 0.08	24.1	2.4	9.5	···	0.1	1
240	220.48645	-1.93346	2.8	···	···	0.61± 0.10	0.62± 0.02	0.28± 0.02	24.5	18.4	10.9	···	0.8	1
241	220.50360	-1.93499	0.7	···	···	0.52± 0.05	0.47± 0.02	0.23± 0.01	20.3	0.9	11.1	···	0.0	1
242	220.57458	-1.94131	0.7	···	···	0.75± 0.11	0.54± 0.01	0.40± 0.05	24.8	1.6	10.5	···	0.1	1
243	220.57959	-2.01522	0.7	···	···	0.47± 0.12	0.48± 0.02	0.25± 0.02	24.2	1.2	10.2	···	0.0	1
244	220.58614	-1.99846	0.7	···	···	0.59± 0.07	0.38± 0.03	0.24± 0.02	31.6	0.7	11.7	···	0.0	0
245	220.61360	-1.93542	0.7	···	···	0.75± 0.10	0.88± 0.03	0.53± 0.01	15.4	3.5	9.3	···	0.1	1
246	220.62610	-1.86985	0.7	···	···	0.56± 0.06	0.38± 0.01	0.21± 0.02	20.5	0.6	12.1	···	0.0	0
247	220.62987	-1.98768	0.7	···	···	0.22± 0.05	0.32± 0.00	0.28± 0.01	8.9	3.2	7.9	···	0.0	1
248	220.63036	-2.02230	0.7	···	···	0.75± 0.06	0.73± 0.02	0.40± 0.03	24.5	1.9	10.3	···	0.1	1
249	220.64902	-1.68893	0.8	···	···	0.54± 0.05	0.41± 0.02	0.16± 0.08	19.2	0.5	13.6	···	0.1	0
250	220.65720	-1.96683	0.7	0.70± 0.03	0.72± 0.07	1.99± 0.07	1.69± 0.02	0.86± 0.06	18.5	4.5	10.2	0.23	1.1	2
251	220.66861	-1.96927	0.7	···	···	1.23± 0.12	1.39± 0.02	0.39± 0.04	22.3	1.1	12.8	···	0.1	1
252	220.67680	-1.97724	0.7	···	···	1.30± 0.08	1.35± 0.02	0.95± 0.05	25.3	5.9	9.3	···	0.1	1
253	220.68027	-1.61378	0.8	···	···	0.48± 0.05	0.32± 0.02	0.28± 0.02	18.9	1.4	10.4	···	0.1	1
254	220.68097	-1.86537	0.7	1.13± 0.05	2.93± 0.10	7.24± 0.20	4.90± 0.01	4.20± 0.01	15.5	17.6	10.1	0.12	2.2	2
255	220.68314	-1.79279	0.7	···	···	1.45± 0.10	1.93± 0.01	1.21± 0.03	22.1	9.7	8.8	···	0.2	1
256	220.68343	-1.82118	0.7	···	···	2.45± 0.12	2.43± 0.02	2.11± 0.03	25.6	14.2	8.9	···	0.3	1
257	220.68738	-1.64756	0.8	···	0.83± 0.07	2.70± 0.09	2.03± 0.02	1.10± 0.01	20.3	8.1	10.0	···	0.5	1
258	220.68959	-1.84020	0.7	···	···	1.40± 0.10	3.24± 0.01	2.47± 0.01	21.0	45.9	7.1	···	0.3	1
259	220.69145	-1.76785	0.7	···	···	0.66± 0.06	0.62± 0.01	0.41± 0.01	18.9	2.2	9.8	···	0.1	1
260	220.71892	-2.09471	0.5	···	···	0.48± 0.13	0.54± 0.03	0.24± 0.03	26.7	0.5	10.5	···	0.0	0
261	220.71959	-1.74963	0.8	···	0.60± 0.06	2.69± 0.13	2.15± 0.02	1.22± 0.03	18.3	11.7	9.3	···	0.5	1
262	220.72655	-2.02186	2.7	···	···	0.20± 0.06	0.16± 0.01	0.09± 0.01	12.7	4.3	11.4	···	0.2	1
263	220.74297	-1.71511	0.8	···	0.61± 0.08	1.86± 0.13	1.53± 0.01	0.83± 0.02	12.7	6.1	10.0	0.03	0.6	2
264	220.77162	-1.72315	0.8	3.18± 0.09	22.07± 0.26	29.11± 0.38	17.91± 0.02	8.56± 0.03	18.8	27.3	13.2	0.49	12.2	2

TABLE 3—*Continued*

ID	ℓ [°]	b [°]	d [kpc]	$F_{70} \pm \Delta F_{70}$ [Jy]	$F_{160} \pm \Delta F_{160}$ [Jy]	$F_{250} \pm \Delta F_{250}$ [Jy]	$F_{350} \pm \Delta F_{350}$ [Jy]	$F_{500} \pm \Delta F_{500}$ [Jy]	r [″]	M [$M_\odot$]	T [K]	F_{22} [Jy]	L_{bol} [$L_\odot$]	unbound/pre-/proto-stellar 0/1/2
265	220.77525	-1.66612	0.8	···	···	1.58± 0.14	1.18± 0.02	0.51± 0.03	23.6	1.7	13.0	···	0.2	1
266	220.77763	-2.07407	2.7	···	···	0.58± 0.05	0.45± 0.01	0.32± 0.01	16.3	21.9	10.1	···	0.7	1
267	220.78081	-2.06005	2.7	···	···	1.17± 0.20	0.96± 0.02	0.76± 0.02	35.2	55.9	9.7	···	1.5	1
268	220.78998	-1.71551	0.8	350.99± 0.70	116.76± 0.58	76.06± 0.61	26.79± 0.03	9.98± 0.03	30.9	11.7	21.2	123.21	493.6	2
269	220.80859	-1.74176	0.8	···	3.84± 0.12	4.16± 0.12	2.10± 0.01	1.10± 0.03	20.5	2.6	14.5	···	0.9	1
270	220.81714	-1.72115	0.8	2.10± 0.08	5.23± 0.11	5.19± 0.20	2.48± 0.02	1.20± 0.03	20.4	2.5	15.4	0.23	3.9	2
271	220.84007	-2.00722	0.5	···	···	1.18± 0.11	0.81± 0.01	0.54± 0.03	28.7	0.8	11.2	···	0.0	1
272	220.85739	-2.12180	0.5	···	···	0.63± 0.15	0.48± 0.01	0.29± 0.02	30.0	0.4	11.1	···	0.0	0
273	220.86861	-1.98951	0.5	···	···	2.03± 0.14	1.91± 0.01	1.09± 0.03	25.6	2.2	10.3	···	0.1	1
274	220.90346	-1.97350	0.5	···	···	0.81± 0.07	0.70± 0.01	0.58± 0.02	19.5	1.3	9.4	···	0.0	1
275	220.91592	-1.84368	0.4	···	···	0.27± 0.04	0.21± 0.03	0.07± 0.03	24.5	0.1	13.8	···	0.0	0
276	220.95256	-1.94321	0.4	···	···	1.49± 0.15	0.91± 0.02	0.57± 0.02	28.1	0.5	12.1	···	0.0	0
277	221.01361	-0.30341	1.8	···	···	0.29± 0.02	0.13± 0.02	0.10± 0.03	16.1	1.2	13.1	···	0.1	0
278	221.01779	-1.88110	0.4	···	0.34± 0.04	1.13± 0.07	0.78± 0.02	0.37± 0.03	23.9	0.6	10.4	···	0.0	1
279	221.02028	-1.85618	0.4	···	···	0.37± 0.06	0.28± 0.02	0.18± 0.01	20.2	0.2	10.7	···	0.0	0
280	221.04073	-2.01474	2.7	···	···	0.34± 0.07	0.27± 0.01	0.17± 0.02	23.6	10.2	10.7	···	0.4	1
281	221.04996	-1.84921	0.4	···	···	0.33± 0.11	0.28± 0.02	0.21± 0.04	21.5	0.3	9.8	···	0.0	0
282	221.06265	-1.82691	0.4	···	···	0.46± 0.08	0.31± 0.01	0.16± 0.03	17.4	0.1	12.4	···	0.0	0
283	221.06631	-1.89868	0.4	···	···	0.73± 0.07	0.43± 0.02	0.23± 0.04	27.6	0.2	13.1	···	0.0	0
284	221.07498	-2.09293	2.7	···	···	0.34± 0.04	0.26± 0.01	0.16± 0.01	17.0	8.6	11.1	···	0.4	1
285	221.10945	-1.80266	0.4	···	···	0.61± 0.08	0.53± 0.02	0.41± 0.02	26.2	0.6	9.6	···	0.0	1
286	221.12860	-1.78952	0.4	···	···	0.69± 0.11	0.69± 0.01	0.41± 0.02	25.5	0.6	9.9	···	0.0	1
287	221.13835	-1.77993	0.4	···	···	0.73± 0.44	0.78± 0.01	0.46± 0.03	30.3	0.8	9.5	···	0.0	1
288	221.14677	-1.70049	0.4	···	···	0.94± 0.21	0.80± 0.03	0.48± 0.04	25.4	0.6	10.6	···	0.0	1
289	221.15402	-1.76118	0.4	···	···	0.62± 0.05	0.47± 0.02	0.28± 0.02	23.9	0.3	10.7	···	0.0	0
290	221.18008	-1.60550	0.4	···	···	0.38± 0.05	0.33± 0.01	0.20± 0.04	25.9	0.3	10.4	···	0.0	0
291	221.20360	-1.70795	0.4	···	···	1.05± 0.12	1.29± 0.02	0.82± 0.03	22.2	1.8	9.1	···	0.0	1
292	221.21077	-1.69173	0.4	···	···	1.91± 0.13	1.90± 0.03	1.45± 0.04	28.6	2.9	9.2	···	0.1	1
293	221.21512	-1.74699	0.4	···	···	0.48± 0.07	0.31± 0.02	0.20± 0.06	23.6	0.2	11.7	···	0.0	0
294	221.22061	-1.70672	0.4	···	···	1.61± 0.08	1.38± 0.03	1.00± 0.05	30.5	1.6	9.9	···	0.0	1
295	221.23824	-1.68452	0.4	···	···	0.67± 0.05	0.65± 0.01	0.31± 0.02	18.7	0.4	11.1	···	0.0	0
296	221.24693	-1.66071	0.4	···	···	0.83± 0.12	0.50± 0.02	0.31± 0.02	30.5	0.4	11.1	···	0.0	0
297	221.25288	-1.88401	3.0	···	···	0.56± 0.05	0.41± 0.01	0.28± 0.01	18.9	19.4	10.7	···	0.8	1
298	221.27051	-1.86055	3.0	···	···	0.64± 0.08	0.40± 0.02	0.22± 0.02	22.3	9.8	12.7	···	0.8	1
299	221.28821	-1.54326	0.5	···	···	0.91± 0.05	0.60± 0.01	0.19± 0.03	26.4	0.2	16.3	···	0.0	0
300	221.31360	-1.49345	0.5	···	···	0.64± 0.04	0.64± 0.01	0.38± 0.02	15.8	1.5	9.1	···	0.0	1
301	221.40959	-1.45116	0.5	···	···	0.39± 0.04	0.53± 0.01	0.25± 0.01	16.7	0.8	9.6	···	0.0	1
302	221.41096	-1.46285	0.5	···	···	0.51± 0.05	0.70± 0.01	0.64± 0.02	25.8	3.6	7.9	···	0.0	1
303	221.41943	-1.88986	0.4	···	···	0.44± 0.07	0.37± 0.01	0.24± 0.01	16.1	0.3	10.3	···	0.0	0
304	221.44730	-1.45209	0.5	···	···	0.83± 0.04	0.62± 0.02	0.39± 0.09	19.2	0.6	11.1	···	0.0	1
305	221.45702	-1.43383	0.5	···	···	0.67± 0.06	0.46± 0.02	0.42± 0.02	19.7	0.9	10.1	···	0.0	1
306	221.47028	-1.44233	0.5	···	···	0.96± 0.12	0.72± 0.02	0.44± 0.03	28.3	0.9	10.9	···	0.0	1
307	221.61063	-1.96285	3.4	···	···	0.43± 0.07	0.42± 0.01	0.26± 0.01	13.1	30.8	9.9	···	0.9	1
308	221.62140	-1.97294	3.4	···	···	0.67± 0.21	0.80± 0.01	0.73± 0.01	23.9	146.9	8.3	···	1.9	1

TABLE 3—*Continued*

ID	ℓ [°]	b [°]	d [kpc]	$F_{70} \pm \Delta F_{70}$ [Jy]	$F_{160} \pm \Delta F_{160}$ [Jy]	$F_{250} \pm \Delta F_{250}$ [Jy]	$F_{350} \pm \Delta F_{350}$ [Jy]	$F_{500} \pm \Delta F_{500}$ [Jy]	r [″]	M [$M_\odot$]	T [K]	F_{22} [Jy]	L_{bol} [$L_\odot$]	unbound/pre-/proto-stellar 0/1/2
309	221.64833	-0.64641	1.8	···	···	0.89± 0.26	0.69± 0.01	0.44± 0.04	32.8	11.5	10.7	···	0.5	1
310	221.65941	-1.97432	3.4	···	···	1.34± 0.06	1.04± 0.02	0.59± 0.03	24.3	47.7	11.2	···	2.4	1
311	221.67384	-0.65854	1.8	···	···	0.43± 0.04	0.29± 0.01	0.17± 0.01	18.1	3.3	11.8	···	0.2	1
312	221.67769	-1.89724	3.4	0.68± 0.04	0.83± 0.04	1.26± 0.11	0.89± 0.02	0.70± 0.01	20.3	44.0	11.4	1.06	39.2	2
313	221.68977	-1.91388	3.4	···	···	0.91± 0.07	0.68± 0.01	0.50± 0.01	21.0	46.6	10.4	···	1.7	1
314	221.76068	-1.87185	3.4	···	···	0.93± 0.06	0.66± 0.02	0.24± 0.02	24.1	11.0	14.5	···	1.4	1
315	221.77640	-1.89046	3.4	···	···	1.28± 0.08	0.91± 0.01	0.61± 0.03	26.4	49.1	10.9	···	2.2	1
316	221.78694	-1.46119	1.1	···	···	0.73± 0.07	0.52± 0.01	0.27± 0.02	24.1	2.0	12.1	···	0.1	1
317	221.79367	-1.93285	3.4	···	···	4.06± 0.08	3.67± 0.05	1.79± 0.01	21.8	154.7	11.1	···	7.6	1
318	221.79500	-1.85506	3.4	···	···	0.68± 0.05	0.45± 0.02	0.27± 0.03	19.4	18.3	11.7	···	1.1	1
319	221.84097	-1.99511	3.4	2.81± 0.13	6.09± 0.16	3.05± 0.19	1.30± 0.01	···	17.3	7.9	22.4	0.08	63.5	2
320	221.85423	-1.97388	3.4	2.35± 0.10	···	3.08± 0.83	1.41± 0.02	···	24.6	11.2	19.9	0.07	45.5	2
321	221.85603	-2.00270	3.4	1.45± 0.10	7.16± 0.24	6.35± 0.27	3.16± 0.03	···	26.4	43.3	16.2	0.28	68.0	2
322	221.87639	-1.50934	1.1	···	···	0.61± 0.08	0.40± 0.02	0.17± 0.04	21.8	1.0	13.7	···	0.1	0
323	221.87692	-1.54629	1.1	···	···	0.83± 0.08	0.55± 0.02	0.40± 0.02	25.8	3.3	11.1	···	0.2	1
324	221.88266	-2.00579	3.4	7.42± 0.24	5.69± 0.15	4.13± 0.16	1.74± 0.02	···	25.7	16.7	18.7	0.30	121.2	2
325	221.88997	-1.94734	3.4	0.23± 0.03	2.20± 0.13	6.09± 0.13	4.80± 0.03	2.86± 0.04	24.8	327.3	10.1	0.06	28.9	2
326	221.89005	-1.97390	3.4	···	2.90± 0.10	4.01± 0.14	1.77± 0.02	0.62± 0.02	25.2	26.2	15.3	0.05	27.4	2
327	221.90764	-1.94720	3.4	0.56± 0.03	1.53± 0.13	4.87± 0.24	4.04± 0.03	···	30.0	328.4	9.7	0.19	31.8	2
328	221.92062	-1.94709	3.4	···	···	3.91± 0.23	3.37± 0.03	2.24± 0.04	30.7	237.7	10.1	···	7.7	1
329	221.94850	-1.98371	3.4	14.56± 0.38	9.23± 0.23	12.94± 0.25	5.66± 0.01	3.14± 0.02	25.7	135.1	14.0	···	137.3	2
330	221.96013	-1.99328	3.4	51.84± 0.26	49.44± 0.40	30.59± 0.43	16.56± 0.02	8.54± 0.02	22.4	211.4	17.0	15.03	1367.9	2
331	221.98361	-1.66118	1.2	···	···	0.47± 0.04	0.40± 0.02	0.23± 0.02	23.4	2.4	10.7	···	0.1	1
332	222.02690	-2.03539	3.4	0.92± 0.03	1.61± 0.08	3.22± 0.08	2.68± 0.01	1.57± 0.01	20.8	116.2	11.1	0.08	29.1	2
333	222.03059	-2.01666	3.4	···	···	1.45± 0.07	1.24± 0.01	0.77± 0.01	20.8	90.0	10.1	···	2.8	1
334	222.05750	-2.03285	3.4	···	···	1.47± 0.07	1.02± 0.01	0.98± 0.02	21.6	89.0	9.9	···	2.8	1
335	222.06302	-1.35355	1.4	···	···	0.51± 0.05	0.38± 0.02	0.20± 0.01	19.4	2.5	11.8	···	0.2	1
336	222.06860	-1.72828	1.2	···	···	0.43± 0.03	0.28± 0.01	0.15± 0.01	19.1	1.0	12.7	···	0.1	0
337	222.07347	-1.61539	1.2	···	···	0.32± 0.04	0.27± 0.01	0.10± 0.07	16.9	0.7	13.0	···	0.1	0
338	222.10800	-1.66619	1.2	···	···	0.34± 0.05	0.23± 0.01	0.07± 0.01	11.0	0.3	16.3	···	0.1	0
339	222.11191	-1.98560	3.2	···	1.39± 0.07	1.42± 0.12	0.99± 0.01	0.50± 0.02	21.9	21.1	13.5	···	4.9	1
340	222.20792	-1.72119	1.4	···	···	0.43± 0.09	0.30± 0.01	0.17± 0.02	20.3	2.2	11.6	···	0.1	1
341	222.21552	-1.74081	1.4	···	···	1.00± 0.10	0.84± 0.02	0.47± 0.06	32.3	6.9	10.9	···	0.3	1
342	222.22256	-1.70764	1.4	···	···	0.40± 0.04	0.25± 0.01	0.14± 0.01	10.4	1.3	12.6	···	0.1	1
343	222.22420	-0.52362	1.1	···	···	0.44± 0.09	0.47± 0.01	0.31± 0.01	22.1	4.3	9.3	···	0.1	1
344	222.22839	-0.48183	1.1	···	···	0.75± 0.50	0.87± 0.01	0.54± 0.02	27.5	8.0	9.3	···	0.2	1
345	222.22861	-1.97452	3.2	···	···	0.36± 0.04	0.22± 0.03	0.14± 0.01	17.8	7.8	12.0	···	0.5	1
346	222.23027	-1.71933	1.4	···	···	0.82± 0.09	0.84± 0.02	0.50± 0.03	20.9	10.3	9.8	···	0.3	1
347	222.25806	-1.65205	1.4	0.21± 0.01	0.41± 0.06	0.47± 0.07	0.24± 0.02	0.09± 0.03	17.3	0.6	15.1	0.01	0.9	2
348	222.28526	-1.97143	3.2	···	···	0.76± 0.05	0.51± 0.01	0.23± 0.03	16.1	11.5	13.1	···	1.0	1
349	222.29474	-1.94483	3.2	···	···	0.92± 0.11	0.54± 0.02	0.51± 0.06	25.5	31.0	10.8	···	1.4	1
350	222.30548	-1.96571	3.2	···	···	1.27± 0.13	0.94± 0.01	0.63± 0.07	26.6	47.5	10.8	···	2.0	1
351	222.33113	-1.26244	1.4	···	···	0.39± 0.04	0.28± 0.01	0.17± 0.01	18.7	2.1	11.6	···	0.1	1
352	222.40762	-0.43437	1.0	···	···	0.80± 0.05	0.73± 0.01	0.45± 0.02	17.6	4.5	10.2	···	0.2	1

TABLE 3—*Continued*

ID	ℓ [°]	b [°]	d [kpc]	$F_{70} \pm \Delta F_{70}$ [Jy]	$F_{160} \pm \Delta F_{160}$ [Jy]	$F_{250} \pm \Delta F_{250}$ [Jy]	$F_{350} \pm \Delta F_{350}$ [Jy]	$F_{500} \pm \Delta F_{500}$ [Jy]	r [″]	M [$M_\odot$]	T [K]	F_{22} [Jy]	L_{bol} [$L_\odot$]	unbound/pre-/proto-stellar 0/1/2
353	222.43056	-0.37747	1.0	···	···	0.28± 0.04	0.21± 0.03	0.16± 0.01	19.0	1.3	10.4	···	0.0	1
354	222.44499	-0.19538	4.7	0.95± 0.04	1.21± 0.06	1.83± 0.04	1.31± 0.01	0.71± 0.01	17.1	91.5	12.0	0.08	45.7	2
355	222.46452	-0.21392	4.7	···	···	0.33± 0.05	0.25± 0.02	0.18± 0.03	17.0	31.3	10.4	···	1.2	1
356	222.48000	-0.36760	1.0	···	···	0.51± 0.09	0.36± 0.01	0.24± 0.02	24.1	1.8	11.0	···	0.1	1
357	222.50493	-1.67362	1.2	···	···	1.98± 0.37	0.92± 0.01	0.54± 0.02	31.9	2.3	14.5	···	0.3	0
358	222.53471	-1.59515	1.2	···	···	1.20± 0.10	0.71± 0.02	0.71± 0.01	24.5	5.9	10.5	···	0.2	1
359	222.56842	-1.58987	3.6	···	0.68± 0.07	2.85± 0.47	2.17± 0.01	1.26± 0.03	28.5	205.3	9.5	0.01	13.5	2
360	222.58058	-1.63926	1.2	···	···	0.33± 0.12	0.43± 0.01	0.41± 0.01	11.8	11.5	7.9	···	0.1	1
361	222.58540	-1.62588	1.2	0.17± 0.02	···	2.97± 0.12	2.30± 0.01	1.52± 0.02	22.1	16.3	10.6	0.03	1.8	2
362	222.58748	-1.66868	1.2	···	···	2.91± 0.96	1.44± 0.01	0.78± 0.02	30.5	3.7	14.3	···	0.4	1
363	222.59723	-1.54188	3.6	···	···	5.02± 0.85	1.51± 0.05	0.83± 0.07	60.0	13.8	21.5	···	5.5	0
364	222.59981	-1.60397	3.6	8.69± 0.21	16.68± 0.13	18.08± 0.18	8.82± 0.02	3.63± 0.03	21.2	161.2	15.3	0.44	253.5	2
365	222.62677	-1.61108	3.6	1.25± 0.04	8.10± 0.15	9.58± 0.18	4.60± 0.01	···	27.4	99.2	14.7	0.13	79.8	2
366	222.63492	-1.59053	3.6	10.82± 0.17	12.99± 0.31	5.05± 0.13	2.83± 0.01	1.50± 0.01	20.2	30.6	19.3	1.00	256.8	2
367	222.67039	-0.36185	1.0	···	···	0.75± 0.05	0.69± 0.01	0.53± 0.01	15.1	6.2	9.4	···	0.1	1
368	222.68245	-1.57599	3.6	0.95± 0.08	3.19± 0.09	5.73± 0.15	3.23± 0.02	1.72± 0.03	33.8	122.0	12.3	0.03	43.0	2
369	222.69707	-1.57972	3.6	0.94± 0.07	2.87± 0.13	3.84± 0.10	2.26± 0.01	0.92± 0.02	20.9	54.1	13.7	0.07	38.7	2
370	222.69827	-1.38536	1.2	···	···	0.79± 0.06	0.48± 0.01	0.25± 0.18	22.1	1.5	13.2	···	0.1	0
371	222.70326	-1.39869	1.2	···	···	0.62± 0.04	0.52± 0.01	0.17± 0.13	15.1	1.1	13.8	···	0.1	0
372	222.70799	-1.69619	1.2	···	···	0.55± 0.18	0.45± 0.02	0.24± 0.04	30.1	2.5	11.1	···	0.1	1
373	222.71811	-1.58156	1.2	···	3.05± 0.15	4.23± 0.17	2.09± 0.02	1.05± 0.02	23.4	6.1	13.7	0.08	3.9	2
374	222.73155	-1.69959	1.2	···	···	0.87± 17.38	0.62± 0.02	0.30± 0.04	31.6	2.2	12.5	···	0.2	0
375	222.74771	-1.63462	1.2	···	···	1.26± 0.10	0.76± 0.01	0.42± 0.02	28.8	2.7	12.9	···	0.2	1
376	222.75381	-1.58264	1.2	···	···	0.83± 0.10	1.77± 0.01	0.89± 0.01	12.7	27.5	8.1	···	0.4	1
377	222.76486	-0.33217	1.0	···	0.54± 0.07	2.11± 0.07	1.87± 0.01	1.26± 0.01	19.2	18.8	9.1	0.07	1.2	2
378	222.77548	-1.57931	1.2	···	···	4.44± 0.29	2.23± 0.01	1.57± 31.30	23.9	8.8	12.8	···	0.7	1
379	222.78471	-1.57365	1.2	···	0.85± 0.06	1.31± 0.09	1.18± 0.01	···	23.3	5.6	11.4	0.08	1.6	2
380	222.78636	-1.64347	1.2	···	···	1.26± 0.09	0.93± 0.04	0.66± 0.03	22.9	7.0	10.5	···	0.3	1
381	222.78694	-0.32338	1.0	···	···	1.12± 0.06	0.96± 0.01	0.78± 0.02	21.6	8.5	9.5	···	0.2	1
382	222.78970	-1.65013	1.2	···	···	0.75± 0.07	0.67± 0.03	0.61± 0.02	18.6	10.0	9.1	···	0.2	1
383	222.81094	-1.65026	1.2	···	···	1.97± 0.10	1.45± 0.01	0.92± 0.02	26.9	10.1	10.7	···	0.4	1
384	222.81493	-2.06935	3.2	···	···	0.43± 0.06	0.29± 0.01	0.17± 0.02	20.1	9.9	11.9	···	0.6	1
385	222.81668	-1.60961	1.2	0.68± 0.03	4.65± 0.13	5.41± 0.12	2.81± 0.02	1.20± 0.04	26.9	6.2	14.6	···	4.0	2
386	222.81987	-1.58147	1.2	···	1.68± 0.07	1.18± 0.10	0.63± 0.01	···	16.0	0.8	17.5	0.06	2.0	2
387	222.82413	-1.55637	1.2	···	0.22± 0.06	0.14± 0.04	0.07± 0.01	···	6.0	0.1	19.3	···	0.1	0
388	222.82747	-0.40408	1.0	···	···	0.32± 0.08	0.48± 0.01	0.41± 0.01	17.6	12.7	7.4	···	0.1	1
389	222.83113	-0.38453	1.0	···	···	1.14± 0.11	0.89± 0.03	0.51± 0.07	23.7	5.4	10.1	···	0.2	1
390	222.84862	-0.34452	1.0	···	···	0.42± 0.06	0.30± 0.01	0.18± 0.03	18.5	1.2	11.5	···	0.1	1
391	222.85194	-1.40858	1.2	···	···	0.32± 0.04	0.27± 0.01	0.16± 0.01	16.7	2.0	10.6	···	0.1	1
392	222.85612	-1.59384	3.5	···	0.89± 0.09	2.86± 0.07	1.73± 0.02	1.10± 0.01	18.2	113.5	10.5	0.03	15.4	2
393	222.86479	-1.98605	3.2	···	···	0.17± 0.07	0.15± 0.01	0.08± 0.01	14.6	6.8	10.7	···	0.3	1
394	222.87193	-1.51286	0.7	···	···	0.49± 0.06	0.37± 0.02	0.17± 0.02	19.3	0.5	12.4	···	0.0	0
395	222.87569	-1.59096	3.5	0.24± 0.04	1.46± 0.12	1.27± 0.11	0.64± 0.01	0.27± 0.01	8.9	8.6	16.4	0.01	12.3	2
396	222.88792	-1.58922	3.5	···	···	1.82± 0.11	1.66± 0.03	0.97± 0.02	25.1	126.8	10.1	···	4.0	1

TABLE 3—*Continued*

ID	ℓ [°]	b [°]	d [kpc]	$F_{70} \pm \Delta F_{70}$ [Jy]	$F_{160} \pm \Delta F_{160}$ [Jy]	$F_{250} \pm \Delta F_{250}$ [Jy]	$F_{350} \pm \Delta F_{350}$ [Jy]	$F_{500} \pm \Delta F_{500}$ [Jy]	r [″]	M [$M_\odot$]	T [K]	F_{22} [Jy]	L_{bol} [$L_\odot$]	unbound/pre-/proto-stellar 0/1/2
397	222.89861	-2.09140	3.2	···	···	0.41± 0.09	0.31± 0.02	0.19± 0.01	20.9	13.5	11.1	···	0.6	1
398	222.90027	-1.37600	0.8	···	···	0.98± 19.52	0.58± 0.02	0.37± 0.02	32.8	1.2	12.1	···	0.1	0
399	222.91457	-1.63621	3.5	···	···	0.43± 0.12	1.00± 0.06	0.10± 0.01	17.7	5.1	14.8	···	1.3	1
400	222.91504	-0.85355	1.0	···	···	0.35± 0.03	0.24± 0.02	0.16± 0.02	19.9	1.0	11.1	···	0.0	0
401	222.91597	-1.56927	3.5	···	···	2.20± 0.19	1.53± 0.03	0.95± 0.03	27.1	76.2	11.4	···	4.0	1
402	222.91953	-0.41049	0.7	···	···	0.65± 0.07	0.41± 0.01	0.30± 0.01	23.6	1.0	11.2	···	0.1	1
403	222.92062	-1.51726	0.7	···	···	0.95± 0.08	0.77± 0.02	0.34± 0.02	24.4	1.2	12.2	···	0.1	1
404	222.92625	-1.59276	3.5	···	···	2.44± 0.09	1.50± 0.02	1.02± 0.03	19.4	70.4	11.7	···	4.2	1
405	222.93190	-1.66507	3.5	···	···	1.12± 0.06	0.80± 0.02	0.40± 0.03	19.5	27.1	12.4	···	2.0	1
406	222.93993	-1.62058	3.5	···	···	1.77± 0.09	1.14± 0.01	0.53± 0.03	24.6	26.4	13.6	···	2.9	1
407	222.94356	-1.05401	1.0	···	···	0.63± 0.04	0.44± 0.02	0.24± 0.03	23.0	1.5	11.7	···	0.1	1
408	222.94872	-1.03252	1.0	···	···	0.27± 0.04	0.14± 0.01	0.06± 0.02	11.6	0.2	15.2	···	0.0	0
409	222.95105	-1.60145	3.5	0.27± 0.03	1.47± 0.11	2.47± 0.16	1.65± 0.02	0.69± 0.03	15.1	52.2	12.3	···	14.3	2
410	222.95894	-1.81255	3.2	···	···	0.37± 0.06	0.23± 0.01	0.10± 0.03	22.9	6.7	12.3	···	0.5	1
411	222.96379	-1.62430	3.5	···	···	1.23± 0.11	0.67± 0.01	0.30± 0.03	18.3	12.7	15.0	···	1.8	1
412	222.96652	-1.58795	3.5	···	···	1.18± 0.08	0.58± 0.01	0.26± 0.03	25.8	9.5	15.9	···	1.6	1
413	222.97255	-1.55855	0.7	0.59± 0.04	0.94± 0.09	0.80± 0.13	0.71± 0.04	···	14.5	0.4	14.8	0.05	0.7	2
414	222.97340	-0.61340	5.7	1.30± 0.05	1.20± 0.06	1.52± 0.03	0.89± 0.02	0.45± 0.01	18.7	64.6	13.3	0.05	69.0	2
415	222.97495	-0.44952	0.9	···	···	0.37± 0.06	0.31± 0.01	0.22± 0.02	23.0	1.7	10.2	···	0.1	1
416	222.97861	-1.66099	1.2	···	···	0.51± 0.11	0.43± 0.02	0.22± 0.05	17.5	2.2	11.2	···	0.1	1
417	222.98337	-1.45358	1.2	···	···	1.06± 0.17	1.30± 0.01	0.73± 0.02	25.7	13.6	9.4	···	0.3	1
418	222.99214	-1.43047	1.2	0.89± 0.04	1.16± 0.09	2.16± 0.11	1.48± 0.02	0.79± 0.03	16.8	7.9	11.6	0.07	3.0	2
419	222.99365	-1.51953	0.7	···	···	1.95± 0.22	1.73± 0.02	0.45± 0.04	34.3	0.6	17.7	···	0.2	0
420	222.99698	-1.51120	0.7	···	···	1.26± 0.16	1.21± 0.01	0.79± 0.03	26.7	5.3	9.5	···	0.1	1
421	223.00484	-1.94195	1.2	···	···	0.42± 0.10	0.35± 0.01	0.14± 0.03	25.1	1.1	12.4	···	0.1	0
422	223.00908	-1.36770	0.8	···	···	0.47± 0.07	0.25± 0.02	0.07± 0.02	19.2	0.0	33.6	···	0.0	0
423	223.01208	-1.50200	1.2	···	0.45± 0.05	1.01± 0.14	0.58± 0.02	0.30± 0.02	22.4	3.1	11.6	···	0.4	1
424	223.01291	-1.47151	1.2	···	···	0.71± 0.10	0.44± 0.01	0.28± 0.01	15.5	2.2	12.1	···	0.1	1
425	223.01425	-1.57421	1.2	···	···	2.14± 0.14	1.19± 0.01	0.65± 0.03	25.3	3.9	13.5	···	0.4	1
426	223.02278	-1.77786	3.4	···	···	0.52± 0.08	0.50± 0.01	0.27± 0.02	14.2	28.5	10.4	···	1.1	1
427	223.02487	-1.76720	3.4	···	0.19± 0.04	0.41± 0.08	0.37± 0.01	0.13± 0.01	12.1	12.5	11.3	0.03	4.0	2
428	223.03162	-1.30387	0.8	···	···	0.48± 0.04	0.49± 0.04	0.27± 0.01	19.7	1.6	10.1	···	0.1	1
429	223.03275	-1.40421	1.2	···	···	1.00± 0.07	0.61± 0.03	0.28± 0.03	24.8	1.9	13.6	···	0.2	0
430	223.03484	-1.56766	1.2	···	···	0.93± 0.14	0.68± 0.02	0.45± 0.02	22.4	4.7	10.9	···	0.2	1
431	223.03651	-1.77189	3.4	0.26± 0.03	0.32± 0.07	0.48± 0.07	0.36± 0.01	0.18± 0.01	10.6	12.5	12.0	···	4.1	2
432	223.03957	-0.44354	1.1	···	···	0.39± 0.04	0.38± 0.01	0.15± 0.01	15.1	1.3	11.7	···	0.1	1
433	223.04083	-1.64808	1.2	···	···	1.06± 0.11	0.62± 0.01	0.39± 0.02	32.9	2.6	12.3	···	0.2	1
434	223.04205	-1.48186	1.2	0.15± 0.01	···	1.20± 0.08	0.90± 0.02	0.50± 0.02	23.3	4.9	11.5	0.07	1.2	2
435	223.05009	-0.38869	1.1	···	···	0.35± 0.04	0.24± 0.01	0.14± 0.03	19.2	1.0	12.0	···	0.1	0
436	223.05023	-1.91044	1.2	···	···	0.30± 0.06	0.20± 0.01	0.10± 0.01	16.9	0.6	13.0	···	0.1	0
437	223.05197	-1.86582	1.2	···	···	1.02± 0.09	0.64± 0.02	0.44± 0.03	29.4	3.5	11.6	···	0.2	1
438	223.05559	-1.82892	3.4	···	···	0.28± 0.07	0.19± 0.01	0.10± 0.02	10.3	6.9	12.0	···	0.5	1
439	223.05699	-1.27096	0.8	···	···	0.47± 0.04	0.39± 0.01	0.20± 0.01	21.6	0.8	11.4	···	0.0	0
440	223.05861	-1.94953	1.2	···	···	0.46± 0.06	0.42± 0.01	0.21± 0.01	17.1	2.2	11.0	···	0.1	1

TABLE 3—*Continued*

ID	ℓ [°]	b [°]	d [kpc]	$F_{70} \pm \Delta F_{70}$ [Jy]	$F_{160} \pm \Delta F_{160}$ [Jy]	$F_{250} \pm \Delta F_{250}$ [Jy]	$F_{350} \pm \Delta F_{350}$ [Jy]	$F_{500} \pm \Delta F_{500}$ [Jy]	r [″]	M [$M_\odot$]	T [K]	F_{22} [Jy]	L_{bol} [$L_\odot$]	unbound/pre-/proto-stellar 0/1/2
441	223.06108	-1.65532	1.2	···	···	0.86± 0.40	0.56± 0.02	0.29± 0.04	34.2	2.0	12.8	···	0.2	0
442	223.06293	-1.39705	0.8	···	···	0.60± 0.13	0.35± 0.02	0.17± 0.05	26.0	0.4	13.9	···	0.0	0
443	223.06514	-1.29952	0.8	···	···	0.37± 0.05	0.33± 0.01	0.24± 0.01	20.2	1.5	9.7	···	0.0	1
444	223.06929	-1.94058	1.2	···	···	0.37± 0.10	0.32± 0.01	0.27± 0.02	15.4	4.1	9.3	···	0.1	1
445	223.07265	-1.55845	1.2	···	···	1.65± 0.16	0.85± 0.01	0.31± 0.05	31.6	1.1	18.0	···	0.3	0
446	223.07832	-1.87203	1.2	···	···	0.57± 0.12	0.54± 0.02	0.35± 0.02	23.3	4.9	9.9	···	0.1	1
447	223.08694	-1.55981	1.2	···	···	1.52± 0.07	0.84± 0.02	0.35± 0.04	23.5	1.6	15.7	···	0.3	0
448	223.08853	-1.94225	1.2	···	···	0.82± 0.08	0.90± 0.01	0.44± 0.03	23.5	6.7	10.1	···	0.2	1
449	223.09561	-1.48521	1.2	···	···	1.61± 0.15	1.92± 0.01	1.24± 0.02	15.5	25.6	9.1	···	0.5	1
450	223.09947	-0.69093	0.9	···	···	0.74± 0.04	0.49± 0.01	0.30± 0.02	27.6	1.5	11.7	···	0.1	1
451	223.10693	-1.57471	1.2	···	···	0.56± 0.08	0.31± 0.01	0.20± 0.02	24.3	1.3	12.7	···	0.1	0
452	223.12990	-2.05228	1.2	···	···	0.43± 0.19	0.53± 0.01	0.25± 0.02	26.0	3.7	10.0	···	0.1	1
453	223.13829	-1.28272	0.8	···	···	0.44± 0.04	0.34± 0.02	0.25± 0.02	25.4	1.3	10.2	···	0.0	1
454	223.13840	-1.43799	1.2	···	0.55± 0.04	0.92± 0.11	0.52± 0.02	0.29± 0.05	24.9	2.4	12.1	···	0.4	1
455	223.14328	-0.19754	0.8	···	···	0.38± 0.04	0.29± 0.01	0.19± 0.01	20.0	0.8	10.9	···	0.0	1
456	223.14444	-1.78344	3.4	···	0.46± 0.05	1.27± 0.07	0.96± 0.01	0.50± 0.02	19.2	55.6	10.4	···	4.0	1
457	223.16089	-1.29860	0.8	···	···	0.94± 0.15	0.65± 0.02	0.59± 0.03	35.3	1.8	11.1	···	0.1	1
458	223.16231	-1.71619	1.2	···	···	0.40± 0.06	0.33± 0.01	0.20± 0.01	16.1	1.8	11.1	···	0.1	1
459	223.17906	-0.66603	0.9	···	···	0.67± 0.04	0.42± 0.02	0.20± 0.03	31.3	0.4	16.0	···	0.1	0
460	223.17934	-1.67436	3.3	···	···	0.38± 0.06	0.26± 0.01	0.11± 0.02	19.8	5.2	13.6	···	0.5	1
461	223.19714	-0.65160	0.9	···	···	0.29± 0.03	0.22± 0.01	0.15± 0.01	16.7	1.0	10.7	···	0.0	1
462	223.20377	-0.70562	1.0	···	···	0.68± 0.03	0.26± 0.01	0.25± 0.02	20.2	0.7	13.0	···	0.1	0
463	223.24860	-1.88349	3.1	···	···	1.50± 0.16	0.91± 0.02	0.43± 0.02	30.6	16.3	14.1	···	1.9	1
464	223.24872	-1.65500	3.3	···	···	0.97± 0.08	0.70± 0.01	0.35± 0.02	20.2	21.6	12.2	···	1.5	1
465	223.26091	-1.84888	3.1	···	···	0.57± 0.07	0.64± 0.01	0.41± 0.04	21.2	51.1	9.3	···	1.2	1
466	223.27808	-1.65952	3.3	···	···	1.34± 0.10	0.94± 0.01	0.40± 0.01	21.8	20.3	13.3	···	2.0	1
467	223.28690	-1.00619	1.0	···	···	0.32± 0.04	0.25± 0.01	0.20± 0.01	19.5	1.8	9.9	···	0.1	1
468	223.28694	-1.80786	3.1	···	···	0.75± 0.08	0.54± 0.02	0.28± 0.03	27.1	16.5	12.0	···	1.1	1
469	223.29581	-1.87834	3.1	···	···	0.75± 0.11	0.69± 0.01	0.37± 0.02	14.2	30.6	10.7	···	1.3	1
470	223.29851	-1.08897	1.0	···	···	0.43± 0.03	0.28± 0.01	0.19± 0.03	17.8	1.2	11.2	···	0.1	1
471	223.31477	-0.88728	1.0	0.48± 0.02	0.24± 0.03	0.17± 0.06	0.05± 0.01	···	8.6	0.0	21.2	0.01	0.6	2
472	223.33730	-1.87369	1.2	···	···	1.68± 0.33	1.50± 0.01	0.84± 0.04	31.3	8.6	11.1	···	0.4	1
473	223.34309	-1.72302	1.2	···	···	0.77± 0.14	0.49± 0.01	0.26± 0.01	19.4	1.8	12.7	···	0.1	1
474	223.34862	-0.74233	0.8	···	···	0.19± 0.02	0.16± 0.02	0.07± 0.03	23.2	0.3	11.9	···	0.0	0
475	223.34940	-1.86552	1.2	···	···	0.75± 15.06	1.26± 0.02	0.56± 0.03	27.7	11.8	9.1	···	0.3	1
476	223.37361	-1.59898	1.2	···	···	0.72± 0.06	0.65± 0.01	0.31± 0.02	23.9	2.9	11.6	···	0.2	1
477	223.37543	-1.86953	1.2	···	···	1.24± 0.07	0.74± 0.03	0.61± 0.03	19.9	5.0	11.1	···	0.2	1
478	223.40527	-1.80164	1.2	···	···	1.41± 0.13	1.04± 0.03	0.64± 0.03	28.9	6.3	11.1	···	0.3	1
479	223.40964	-0.94786	1.0	···	···	0.69± 0.04	0.60± 0.02	0.56± 0.01	18.7	6.5	9.1	···	0.1	1
480	223.41028	-0.85286	1.0	···	···	1.35± 0.06	1.24± 0.02	0.51± 0.01	22.1	3.3	11.9	···	0.2	1
481	223.41595	-1.84052	1.2	···	···	2.01± 0.13	2.00± 0.01	1.27± 0.02	27.0	19.2	9.7	···	0.5	1
482	223.41833	-1.83520	1.2	0.35± 0.03	0.81± 0.11	1.81± 0.10	2.14± 0.01	1.01± 0.01	19.9	15.0	10.1	0.16	2.2	2
483	223.42528	-1.59261	1.2	···	···	0.38± 0.08	0.25± 0.02	0.09± 0.03	19.6	0.5	14.6	···	0.1	0
484	223.42528	-0.92787	1.0	···	···	2.44± 0.16	2.69± 0.02	2.13± 0.03	23.4	31.7	8.7	···	0.5	1

TABLE 3—*Continued*

ID	ℓ [°]	b [°]	d [kpc]	$F_{70} \pm \Delta F_{70}$ [Jy]	$F_{160} \pm \Delta F_{160}$ [Jy]	$F_{250} \pm \Delta F_{250}$ [Jy]	$F_{350} \pm \Delta F_{350}$ [Jy]	$F_{500} \pm \Delta F_{500}$ [Jy]	r [″]	M [$M_\odot$]	T [K]	F_{22} [Jy]	L_{bol} [$L_\odot$]	unbound/pre-/proto-stellar 0/1/2
485	223.43175	-1.82718	1.2	···	···	1.99± 0.15	2.34± 0.01	0.80± 0.02	28.0	8.3	11.5	···	0.5	1
486	223.43361	-1.73632	1.2	···	···	10.85± 0.18	4.38± 0.03	3.85± 0.02	31.6	18.0	13.0	···	1.7	1
487	223.43385	-1.87511	1.2	0.29± 0.04	0.79± 0.08	0.48± 0.12	0.17± 0.01	···	13.6	0.1	22.2	0.02	1.0	2
488	223.43474	-1.81328	1.2	3.42± 0.08	4.60± 0.16	5.01± 0.24	2.69± 0.01	1.20± 0.01	13.2	6.1	14.7	0.84	12.3	2
489	223.43942	-0.93338	1.0	0.86± 0.04	1.39± 0.09	2.36± 0.11	1.69± 0.01	···	13.6	5.6	11.7	0.02	1.9	2
490	223.44583	-1.74260	1.2	···	···	4.86± 0.12	2.84± 0.01	1.39± 0.02	19.1	7.9	13.8	···	0.8	1
491	223.45030	-0.86363	1.0	···	···	0.31± 0.06	0.44± 0.01	0.31± 0.03	25.9	5.5	8.4	···	0.1	1
492	223.45251	-0.93630	1.0	12.37± 0.14	11.01± 0.18	8.85± 0.22	4.81± 0.02	1.65± 0.03	14.7	4.6	17.0	3.13	27.5	2
493	223.45625	-1.74560	1.2	···	···	2.67± 0.13	2.83± 0.01	1.80± 0.03	19.4	30.3	9.5	···	0.8	1
494	223.46800	-0.88045	1.0	···	···	0.34± 0.06	0.26± 0.02	0.10± 0.02	19.0	0.5	13.1	···	0.0	0
495	223.46904	-0.40646	0.8	···	0.37± 0.02	0.30± 0.03	0.16± 0.02	···	19.3	0.1	16.4	0.01	0.2	2
496	223.47890	-0.91579	1.0	···	···	0.76± 0.06	0.81± 0.01	0.53± 0.02	18.5	6.4	9.4	···	0.2	1
497	223.48235	-0.99317	1.0	···	1.24± 0.06	1.30± 0.15	0.85± 0.01	0.46± 0.02	26.0	1.7	13.6	0.01	0.9	2
498	223.48395	-1.75978	1.2	···	···	6.58± 0.28	6.59± 0.01	3.55± 0.03	24.7	47.2	10.3	···	1.7	1
499	223.49496	-1.63762	1.2	···	···	0.68± 0.13	0.49± 0.02	0.32± 0.03	26.4	3.1	11.0	···	0.1	1
500	223.49736	-0.59913	0.8	···	···	0.40± 0.03	0.30± 0.02	0.14± 0.02	16.8	0.4	12.6	···	0.0	0
501	223.50287	-0.92286	1.0	···	···	0.64± 0.06	0.59± 0.01	0.46± 0.02	22.8	5.1	9.4	···	0.1	1
502	223.51814	-1.83536	1.1	···	···	2.77± 0.16	1.32± 0.02	1.29± 0.02	25.1	6.8	12.0	···	0.5	1
503	223.51830	-1.77699	1.1	1.90± 0.08	4.10± 0.20	9.36± 0.19	6.72± 0.01	4.88± 0.02	24.1	61.8	10.1	0.09	7.8	2
504	223.52119	-0.56286	0.8	···	···	0.28± 0.04	0.25± 0.01	0.16± 0.02	14.6	0.9	10.2	···	0.0	1
505	223.52808	-1.79086	1.1	0.23± 0.04	1.87± 0.18	11.25± 0.21	10.77± 0.02	7.87± 0.02	28.6	208.2	8.3	0.05	5.2	2
506	223.53317	-1.85961	1.1	0.26± 0.04	1.31± 0.16	7.91± 0.38	5.51± 0.02	3.60± 0.01	24.9	75.1	8.9	0.07	3.5	2
507	223.53740	-0.93668	1.0	···	···	0.58± 0.06	0.54± 0.01	0.42± 0.01	15.1	4.8	9.4	···	0.1	1
508	223.54027	-1.80403	1.1	···	···	1.82± 0.19	1.83± 0.01	1.24± 0.01	17.2	19.2	9.5	···	0.5	1
509	223.54720	-0.95313	1.0	···	···	2.57± 0.09	2.25± 0.01	1.57± 0.03	24.4	15.3	9.9	···	0.5	1
510	223.56526	-1.87287	1.1	···	···	1.59± 0.14	1.35± 0.01	1.35± 0.02	24.5	19.9	9.1	···	0.4	1
511	223.57730	-1.81759	1.1	···	···	1.35± 0.18	1.17± 0.02	0.86± 0.01	16.7	11.2	9.8	···	0.3	1
512	223.58498	-1.76281	1.1	0.66± 0.06	1.36± 0.25	1.26± 0.22	0.98± 0.01	0.44± 0.01	21.2	2.5	13.6	0.08	2.3	2
513	223.58656	-1.85283	1.1	···	···	0.98± 0.35	0.69± 0.01	0.28± 0.02	12.0	1.7	13.7	···	0.2	1
514	223.59427	-1.86906	1.1	···	···	1.83± 0.25	1.86± 0.02	0.86± 0.04	22.1	9.7	10.8	···	0.4	1
515	223.59512	-1.82017	1.1	···	···	4.36± 0.18	2.32± 0.04	1.69± 0.02	31.5	10.5	12.1	···	0.7	1
516	223.59544	-0.92339	1.0	···	···	1.81± 0.08	1.89± 0.02	1.11± 0.03	22.9	11.9	9.8	···	0.3	1
517	223.60013	-1.86221	1.1	···	1.95± 0.12	2.96± 0.30	2.08± 0.02	···	23.2	8.0	12.2	0.05	2.6	2
518	223.60364	-1.77837	1.1	1.23± 0.18	2.23± 0.12	1.78± 0.12	0.72± 0.02	···	22.1	0.8	18.1	0.05	3.3	2
519	223.60861	-0.88459	1.0	···	···	0.67± 0.10	0.68± 0.03	0.57± 0.02	20.0	7.7	8.9	···	0.1	1
520	223.61470	-1.89882	1.1	4.93± 0.19	4.55± 0.20	1.95± 0.26	0.99± 0.03	···	18.1	0.6	22.8	0.34	10.6	2
521	223.62488	-1.72885	1.1	···	1.01± 0.13	0.98± 0.12	0.55± 0.02	···	25.7	1.1	15.0	0.01	0.9	2
522	223.63028	-0.70208	0.8	···	···	0.29± 0.07	0.35± 0.01	0.16± 0.02	21.1	1.0	10.2	···	0.0	1
523	223.63716	-1.89807	1.1	···	···	1.59± 0.11	1.23± 0.01	0.76± 0.02	17.3	6.8	11.1	···	0.3	1
524	223.64027	-1.85328	1.1	···	···	1.67± 0.19	1.43± 0.01	1.01± 0.04	19.0	12.8	10.0	···	0.4	1
525	223.64360	-1.11120	1.0	···	···	0.72± 0.12	0.36± 0.02	0.23± 0.02	24.6	1.0	13.0	···	0.1	0
526	223.64798	-1.79046	1.1	···	1.06± 0.11	1.73± 0.15	1.27± 0.01	···	23.5	5.5	11.8	0.10	2.0	2
527	223.65361	-0.86809	0.8	···	···	1.00± 0.15	0.88± 0.02	0.46± 0.05	26.2	2.3	10.9	···	0.1	1
528	223.65729	-1.96564	1.1	6.79± 0.14	6.48± 0.16	7.83± 0.34	3.76± 0.02	1.41± 0.03	25.9	6.1	15.2	0.41	13.7	2

TABLE 3—*Continued*

ID	ℓ [°]	b [°]	d [kpc]	$F_{70} \pm \Delta F_{70}$ [Jy]	$F_{160} \pm \Delta F_{160}$ [Jy]	$F_{250} \pm \Delta F_{250}$ [Jy]	$F_{350} \pm \Delta F_{350}$ [Jy]	$F_{500} \pm \Delta F_{500}$ [Jy]	r [″]	M [$M_\odot$]	T [K]	F_{22} [Jy]	L_{bol} [$L_\odot$]	unbound/pre-/proto-stellar 0/1/2
529	223.66194	-0.84791	0.8	···	···	0.43± 0.10	0.51± 0.02	0.38± 0.02	25.9	3.7	8.7	···	0.1	1
530	223.66194	-0.81619	0.8	···	···	0.36± 0.09	0.36± 0.01	0.23± 0.02	19.9	1.6	9.7	···	0.0	1
531	223.66371	-1.80012	1.1	5.87± 0.29	5.40± 0.59	5.70± 0.47	2.60± 0.03	1.22± 0.02	32.5	4.8	15.7	0.20	12.2	2
532	223.67334	-0.74704	0.8	···	···	0.78± 0.06	0.69± 0.02	0.23± 0.02	24.6	0.6	13.6	···	0.1	0
533	223.67926	-1.10755	1.0	···	···	0.56± 0.05	0.31± 0.02	0.15± 0.02	17.6	0.5	14.6	···	0.1	0
534	223.68062	-1.88802	1.1	···	···	3.72± 0.16	3.10± 0.02	2.02± 0.03	23.4	23.1	10.4	···	0.8	1
535	223.68073	-1.75561	1.1	9.90± 0.80	4.25± 0.12	2.12± 0.44	0.91± 0.02	···	23.9	0.6	22.4	0.10	13.2	2
536	223.68161	-0.74865	0.8	···	···	0.79± 0.07	0.71± 0.02	0.49± 0.02	26.4	4.1	9.1	···	0.1	1
537	223.69362	-0.83443	0.8	···	···	0.40± 0.05	0.42± 0.01	0.29± 0.02	17.3	2.2	9.4	···	0.1	1
538	223.70442	-1.77953	1.1	···	···	2.00± 0.22	1.57± 0.02	0.78± 0.04	24.6	6.6	11.8	···	0.4	1
539	223.72227	-1.98775	1.1	···	2.73± 0.25	3.25± 0.15	4.63± 0.02	···	16.8	12.8	11.6	0.07	3.2	2
540	223.72473	-0.84729	0.8	0.46± 0.02	0.67± 0.04	2.78± 0.09	2.36± 0.02	1.66± 0.02	25.7	14.6	9.1	0.13	1.2	2
541	223.72644	-0.12151	1.0	···	···	0.96± 0.05	0.69± 0.01	0.44± 0.02	18.7	2.8	11.1	···	0.1	1
542	223.73253	-1.90505	1.1	2.51± 0.10	5.96± 0.21	4.92± 0.15	3.20± 0.00	1.53± 0.03	8.6	5.9	14.7	0.21	7.5	2
543	223.73430	-0.82835	0.8	···	0.76± 0.08	1.20± 0.11	1.25± 0.01	0.81± 0.01	14.0	4.1	10.5	···	0.3	1
544	223.73595	-1.78453	1.1	···	···	2.77± 0.27	2.12± 0.02	1.16± 0.04	30.5	10.2	11.5	···	0.6	1
545	223.74008	-0.78903	0.8	···	···	0.74± 0.07	0.74± 0.02	0.43± 0.02	19.9	2.4	10.1	···	0.1	1
546	223.74031	-1.76021	1.1	···	···	2.69± 0.35	1.85± 0.02	1.24± 0.02	28.7	11.0	11.1	···	0.5	1
547	223.74309	-1.67066	1.3	···	···	0.71± 0.13	0.55± 0.01	0.29± 0.01	15.2	3.1	11.5	···	0.2	1
548	223.74458	-1.90972	1.1	4.45± 0.09	4.57± 0.21	5.02± 0.23	3.89± 0.01	1.62± 0.04	16.0	8.9	13.3	1.43	13.3	2
549	223.74734	-0.87097	0.8	1.29± 0.05	3.16± 0.11	3.52± 0.16	2.18± 0.02	1.09± 0.02	14.5	2.8	13.7	0.01	1.9	2
550	223.74777	-1.11150	0.9	···	···	1.30± 0.07	1.00± 0.02	0.93± 0.03	23.4	7.7	9.5	···	0.2	1
551	223.74796	-1.14737	0.9	···	···	0.27± 0.07	0.19± 0.01	0.12± 0.01	14.3	1.1	10.1	···	0.0	1
552	223.75101	-1.08787	0.8	···	···	0.48± 0.08	0.35± 0.01	0.22± 0.02	16.4	1.0	11.1	···	0.0	1
553	223.75519	-1.81576	1.1	···	···	1.41± 0.20	1.27± 0.02	0.79± 0.02	18.1	9.8	10.2	···	0.3	1
554	223.76877	-0.06406	1.0	···	···	0.89± 0.03	0.43± 0.01	0.25± 0.02	22.4	0.8	14.1	···	0.1	0
555	223.77863	-1.82442	1.1	···	0.90± 0.09	1.87± 0.23	1.39± 0.02	···	23.7	7.9	11.0	0.06	1.6	2
556	223.77907	-1.96897	1.1	0.84± 0.09	1.23± 0.13	1.01± 0.15	0.61± 0.01	···	10.1	1.1	15.2	0.05	1.9	2
557	223.77994	-0.05393	1.0	···	···	0.76± 0.04	0.52± 0.01	0.30± 0.02	22.0	1.6	11.8	···	0.1	1
558	223.77998	-1.09112	0.9	···	···	0.58± 0.11	0.38± 0.03	0.25± 0.02	23.4	1.2	11.6	···	0.1	0
559	223.78171	-0.80509	0.8	···	···	0.73± 0.10	0.64± 0.02	0.53± 0.04	20.2	3.8	9.3	···	0.1	1
560	223.78377	-0.81954	0.8	···	···	0.56± 0.10	0.55± 0.02	0.35± 0.02	20.5	2.3	9.8	···	0.1	1
561	223.78526	-1.81287	1.1	···	···	5.67± 2.09	3.71± 0.02	2.52± 0.03	39.1	20.7	11.3	···	1.1	1
562	223.78952	-1.96029	1.1	1.79± 0.06	5.31± 0.22	4.66± 0.15	2.28± 0.02	1.25± 0.02	24.1	4.0	15.5	0.12	5.8	2
563	223.79861	-1.64567	1.3	···	0.85± 0.08	0.94± 0.10	0.52± 0.01	···	19.9	1.4	14.5	0.02	1.2	2
564	223.80055	-1.82971	1.1	···	···	3.87± 0.17	3.37± 0.01	2.20± 0.02	26.0	26.2	10.2	···	0.9	1
565	223.80098	-0.84007	0.8	···	···	0.81± 0.13	0.70± 0.03	0.41± 0.05	24.1	1.8	11.1	···	0.1	1
566	223.80861	-1.48786	1.3	···	···	0.64± 0.05	0.38± 0.01	0.13± 0.02	15.1	0.7	16.2	···	0.1	0
567	223.81619	-1.64809	1.3	···	···	2.25± 0.27	1.11± 0.03	0.57± 0.02	33.6	1.8	17.7	···	0.4	0
568	223.83205	-1.83230	1.1	···	1.33± 0.09	3.52± 0.25	2.28± 0.02	1.99± 0.01	23.3	19.5	10.3	···	1.3	1
569	223.83426	-1.52120	1.3	···	···	2.13± 0.12	1.59± 0.03	0.91± 0.03	24.6	9.8	11.4	···	0.5	1
570	223.83655	-1.53128	1.3	···	···	1.69± 0.17	1.67± 0.03	0.54± 0.03	21.1	5.0	12.7	···	0.4	1
571	223.83768	-1.86863	1.1	···	···	1.43± 0.13	1.37± 0.01	0.85± 0.03	13.9	10.8	10.1	···	0.3	1
572	223.84377	-1.48866	1.3	···	1.06± 0.08	1.18± 0.13	0.60± 0.01	0.29± 0.01	20.0	2.4	13.6	0.02	1.4	2

TABLE 3—*Continued*

ID	ℓ [°]	b [°]	d [kpc]	$F_{70} \pm \Delta F_{70}$ [Jy]	$F_{160} \pm \Delta F_{160}$ [Jy]	$F_{250} \pm \Delta F_{250}$ [Jy]	$F_{350} \pm \Delta F_{350}$ [Jy]	$F_{500} \pm \Delta F_{500}$ [Jy]	r [″]	M [$M_\odot$]	T [K]	F_{22} [Jy]	L_{bol} [$L_\odot$]	unbound/pre-/proto-stellar 0/1/2
573	223.84630	-1.87010	1.1	0.68± 0.05	1.39± 0.17	2.66± 0.21	2.46± 0.04	···	17.6	14.6	10.7	0.14	3.0	2
574	223.84694	-1.93481	1.1	···	···	2.35± 0.17	1.51± 0.02	0.78± 0.03	24.2	5.0	12.8	···	0.4	1
575	223.85141	-0.89910	0.8	···	···	0.49± 0.05	0.34± 0.01	0.30± 0.01	17.7	1.5	10.1	···	0.1	1
576	223.85164	-1.18779	0.9	···	···	0.64± 0.17	0.52± 0.05	0.35± 0.02	16.4	1.8	11.1	···	0.1	1
577	223.85423	-1.78700	1.1	0.85± 0.05	1.63± 0.09	3.01± 0.28	1.86± 0.02	0.74± 0.03	31.7	5.7	12.6	0.03	2.8	2
578	223.85878	-1.12276	0.9	···	···	0.84± 0.18	1.02± 0.01	0.63± 0.01	19.6	7.3	9.2	···	0.2	1
579	223.86028	-0.87139	0.8	···	···	0.47± 0.09	0.37± 0.01	0.33± 0.02	17.2	2.0	9.6	···	0.1	1
580	223.86278	-0.90451	0.8	···	···	0.42± 0.04	0.36± 0.01	0.23± 0.01	14.4	1.3	10.3	···	0.0	1
581	223.87694	-0.87620	0.8	···	···	0.48± 0.07	0.49± 0.01	0.32± 0.02	24.5	2.3	9.6	···	0.1	1
582	223.87755	-1.58461	1.3	···	···	0.74± 0.12	0.48± 0.01	0.31± 0.01	18.2	3.1	11.5	···	0.2	1
583	223.87941	-1.43669	1.3	···	1.83± 0.07	2.20± 0.15	1.45± 0.01	0.52± 0.02	22.5	3.8	14.0	0.03	2.5	2
584	223.88095	-1.12962	0.9	···	···	0.60± 0.09	0.61± 0.01	0.51± 0.01	12.9	5.9	8.9	···	0.1	1
585	223.88525	-2.00384	1.1	···	1.44± 0.09	0.98± 0.18	0.46± 0.01	···	19.7	0.5	18.5	0.02	1.2	2
586	223.88632	-0.89515	0.8	···	···	0.39± 0.09	0.25± 0.02	0.17± 0.02	20.8	1.1	10.1	···	0.0	1
587	223.88988	-1.87494	1.1	···	0.47± 0.18	1.48± 0.15	2.36± 0.01	1.99± 0.03	23.5	49.0	8.1	0.01	1.1	2
588	223.89125	-1.71452	1.1	···	···	0.95± 0.04	0.45± 0.01	0.27± 0.01	8.9	1.2	14.1	···	0.1	1
589	223.89288	-1.84989	1.1	0.50± 0.04	0.92± 0.14	2.18± 0.20	1.77± 0.01	1.34± 0.01	17.6	14.8	10.1	0.03	1.9	2
590	223.89372	-1.21371	0.9	···	···	0.53± 0.12	0.41± 0.01	0.35± 0.02	27.1	3.0	9.7	···	0.1	1
591	223.89456	-1.90002	1.1	···	···	0.57± 0.15	1.50± 0.04	0.21± 0.01	7.7	1.7	12.1	···	0.2	1
592	223.89989	-1.85853	1.1	···	0.72± 0.13	1.13± 0.17	0.98± 0.01	···	12.8	4.4	11.4	···	0.5	1
593	223.90250	-1.87620	1.1	···	···	2.39± 0.25	3.45± 0.01	2.12± 0.03	24.1	46.4	8.7	···	0.8	1
594	223.90266	-1.44495	1.3	···	0.97± 0.06	1.00± 0.12	0.44± 0.01	···	21.3	0.9	16.0	0.07	1.8	2
595	223.90669	-1.80657	1.1	···	···	9.86± 0.79	5.66± 0.15	3.78± 0.06	52.4	24.3	12.2	···	1.7	1
596	223.91028	-1.46620	1.3	···	···	2.09± 0.09	1.23± 0.01	0.71± 0.02	23.6	5.4	12.7	···	0.4	1
597	223.91878	-1.49035	1.3	···	···	2.22± 0.80	2.06± 0.02	1.44± 0.02	22.2	25.0	9.7	···	0.7	1
598	223.92104	-1.60540	1.3	···	···	0.96± 0.21	0.80± 0.03	0.35± 0.03	21.9	3.3	12.3	···	0.2	1
599	223.92487	-1.15411	0.9	···	0.41± 0.06	1.65± 0.44	2.69± 0.02	2.02± 0.19	21.9	31.4	8.3	···	0.6	1
600	223.92694	-0.78995	0.8	···	···	0.88± 0.11	0.61± 0.02	0.35± 0.03	23.9	1.3	11.8	···	0.1	1
601	223.93051	-1.88770	1.1	1.18± 0.07	2.16± 0.17	2.80± 0.25	1.87± 0.01	0.79± 0.02	14.1	4.3	13.6	···	2.6	2
602	223.93158	-1.65494	1.1	···	···	0.75± 0.09	0.46± 0.01	0.23± 0.04	25.0	1.3	13.3	···	0.1	0
603	223.93387	-1.49817	1.3	···	2.38± 0.09	3.99± 0.12	2.59± 0.01	1.30± 0.02	25.3	12.5	12.1	···	1.9	1
604	223.93506	-1.50724	1.3	···	···	3.90± 0.12	2.16± 0.02	0.66± 0.02	25.5	2.4	19.1	···	0.7	0
605	223.93608	-1.89748	1.1	0.35± 0.07	1.28± 0.12	2.37± 0.17	1.82± 0.01	···	27.4	9.3	11.2	···	1.5	2
606	223.94341	-1.97331	1.1	···	···	2.33± 0.13	1.62± 0.01	0.64± 0.01	22.8	3.5	14.0	···	0.4	1
607	223.94472	-0.96151	3.6	···	···	0.67± 0.08	0.56± 0.02	0.37± 0.03	24.7	40.4	10.4	···	1.5	1
608	223.94691	-1.06714	0.9	···	···	0.27± 0.05	0.22± 0.02	0.10± 0.03	21.5	0.5	12.1	···	0.0	0
609	223.94861	-1.16364	0.9	···	···	0.94± 0.06	0.97± 0.01	0.70± 0.01	21.9	7.5	9.2	···	0.2	1
610	223.94992	-0.90822	3.6	···	···	0.33± 0.06	0.25± 0.01	0.13± 0.05	18.3	10.3	11.8	···	0.6	1
611	223.95480	-0.58193	0.8	0.56± 0.04	0.68± 0.04	0.18± 0.05	0.01± 0.00	···	1.2	0.0	14.8	0.04	0.7	2
612	223.95763	-1.11681	0.9	···	···	1.30± 25.94	1.00± 0.02	0.63± 0.02	32.2	4.1	10.8	···	0.2	1
613	223.96527	-1.17333	0.9	···	···	0.41± 0.08	0.36± 0.01	0.29± 0.01	13.8	2.6	9.5	···	0.1	1
614	223.96693	-1.88535	1.1	···	···	2.22± 0.14	1.51± 0.01	0.71± 0.02	24.1	4.6	12.9	···	0.4	1
615	223.97079	-1.83067	1.1	···	1.22± 0.16	7.63± 0.22	7.95± 0.02	6.10± 0.02	30.2	193.5	7.9	···	3.0	1
616	223.98596	-1.13722	0.9	···	···	0.94± 0.10	0.85± 0.02	0.39± 0.02	18.4	2.4	11.4	···	0.1	1

TABLE 3—*Continued*

ID	ℓ [°]	b [°]	d [kpc]	$F_{70} \pm \Delta F_{70}$ [Jy]	$F_{160} \pm \Delta F_{160}$ [Jy]	$F_{250} \pm \Delta F_{250}$ [Jy]	$F_{350} \pm \Delta F_{350}$ [Jy]	$F_{500} \pm \Delta F_{500}$ [Jy]	r [″]	M [$M_\odot$]	T [K]	F_{22} [Jy]	L_{bol} [$L_\odot$]	unbound/pre-/proto-stellar 0/1/2
617	223.98892	-1.81974	1.1	3.95± 0.09	9.43± 0.18	12.85± 0.31	10.37± 0.01	6.91± 0.01	19.0	50.2	11.6	0.07	13.6	2
618	223.99164	-1.88733	1.1	···	···	2.48± 0.23	1.33± 0.01	0.59± 0.03	25.9	2.4	15.4	···	0.4	1
619	224.00452	-1.73126	1.1	1.53± 0.07	3.67± 0.17	5.26± 0.21	3.20± 0.01	1.91± 0.02	20.5	11.7	12.5	0.12	5.5	2
620	224.01366	-1.68320	1.1	2.45± 0.09	6.35± 0.19	7.87± 0.21	5.00± 0.06	2.85± 0.01	15.0	15.8	12.9	0.06	8.1	2
621	224.01607	-1.71020	1.1	1.77± 0.07	3.00± 0.17	4.40± 0.29	3.31± 0.01	2.51± 0.03	19.9	17.1	11.4	0.72	7.5	2
622	224.01776	-1.64680	1.1	···	···	1.12± 0.07	1.18± 0.00	0.84± 0.02	11.8	13.4	9.2	···	0.3	1
623	224.01990	-1.66953	1.1	···	···	1.20± 0.13	1.21± 0.02	0.81± 0.01	10.7	11.3	9.5	···	0.3	1
624	224.02362	-0.11928	0.9	···	···	0.34± 0.05	0.26± 0.01	0.21± 0.01	16.7	1.6	10.0	···	0.1	1
625	224.02505	-1.16522	0.9	···	···	1.25± 0.13	0.91± 0.02	0.44± 0.03	28.0	2.1	12.4	···	0.2	1
626	224.02553	-1.19359	0.9	···	···	1.53± 0.16	1.42± 0.02	0.79± 0.02	30.4	6.0	10.5	···	0.2	1
627	224.02635	-1.62812	1.1	···	···	1.47± 0.09	1.07± 0.01	0.50± 0.02	22.3	3.4	12.5	···	0.3	1
628	224.05360	-1.19887	0.9	···	···	0.66± 0.12	0.72± 0.02	0.28± 0.03	23.0	1.9	11.2	···	0.1	1
629	224.05435	-1.94756	1.1	···	2.44± 0.20	7.47± 0.37	4.20± 0.03	2.31± 0.03	36.8	22.5	11.1	···	2.4	1
630	224.05940	-1.91428	1.1	···	···	1.90± 0.15	1.27± 0.01	0.62± 0.03	26.2	4.1	12.8	···	0.3	1
631	224.06139	-1.76787	1.1	···	···	2.33± 0.12	1.03± 0.02	0.38± 0.02	33.2	0.9	20.2	···	0.3	0
632	224.07361	-0.17304	0.9	···	···	0.35± 0.05	0.30± 0.01	0.17± 0.01	20.6	1.2	10.8	···	0.1	1
633	224.07870	-1.20919	0.9	···	···	0.67± 0.26	1.93± 0.04	0.42± 0.03	24.5	4.5	9.7	···	0.2	1
634	224.07895	-1.96155	1.1	···	···	2.82± 0.17	2.93± 0.01	2.81± 0.02	23.4	57.6	8.5	···	0.8	1
635	224.08058	-1.98522	1.1	···	···	2.22± 0.28	1.82± 0.01	1.56± 0.02	27.3	21.1	9.5	···	0.5	1
636	224.08095	-1.12886	0.9	···	···	1.84± 0.19	2.30± 0.03	1.82± 0.02	30.1	27.1	8.4	···	0.4	1
637	224.08249	-1.95217	1.1	···	0.84± 0.22	3.37± 0.14	3.10± 0.01	1.49± 0.01	19.2	26.4	9.5	0.04	1.9	2
638	224.08719	-1.96632	1.1	0.24± 0.05	0.45± 0.10	1.26± 0.12	1.27± 0.01	···	14.6	13.3	9.4	···	0.8	2
639	224.09500	-1.87034	1.1	···	···	2.13± 0.19	1.17± 0.02	0.69± 0.06	29.4	3.9	13.1	···	0.3	1
640	224.09650	-1.84404	1.1	···	···	1.53± 0.28	1.18± 0.01	0.70± 0.02	29.3	6.5	11.1	···	0.3	1
641	224.09785	-1.11317	0.9	0.25± 0.03	2.46± 0.11	8.56± 0.44	7.15± 0.01	4.52± 0.03	21.6	47.2	9.5	0.04	2.8	2
642	224.10175	-1.79669	1.1	···	1.15± 0.08	5.50± 0.20	0.97± 0.03	···	33.4	3.3	12.8	0.01	1.6	2
643	224.10960	-1.96574	1.1	4.89± 0.10	8.19± 0.21	9.82± 0.31	6.91± 0.02	2.68± 0.03	16.2	15.7	13.6	0.43	15.3	2
644	224.11028	-1.27501	0.9	···	···	2.72± 0.16	1.94± 0.03	1.04± 0.02	29.4	5.3	11.9	···	0.3	1
645	224.11250	-1.59808	1.5	···	···	0.54± 0.06	0.39± 0.02	0.27± 0.01	15.1	4.1	10.9	···	0.2	1
646	224.11566	-1.52120	1.5	···	···	0.95± 0.06	0.49± 0.02	0.27± 0.04	23.9	2.0	14.3	···	0.2	0
647	224.11861	-1.74453	1.1	···	···	1.36± 0.14	1.39± 0.01	1.01± 0.01	21.2	15.5	9.3	···	0.3	1
648	224.11893	-1.91625	1.1	···	···	2.28± 0.26	1.45± 0.02	0.74± 0.02	28.4	4.7	13.0	···	0.4	1
649	224.11919	-1.10325	0.9	0.71± 0.03	4.33± 0.16	7.48± 0.13	7.91± 0.02	4.72± 0.01	20.6	33.7	10.4	0.11	3.9	2
650	224.12708	-1.08521	0.9	···	···	2.89± 0.10	3.41± 0.01	2.70± 0.02	20.2	36.4	8.6	···	0.6	1
651	224.13164	-1.10598	0.9	1.55± 0.06	1.62± 0.11	3.50± 0.11	2.63± 0.01	···	19.9	10.3	10.8	0.34	3.5	2
652	224.13194	-1.09787	0.9	···	···	2.21± 0.10	2.68± 0.01	1.74± 0.01	17.3	21.1	9.0	···	0.4	1
653	224.13362	-1.75298	1.5	···	1.22± 0.11	3.16± 0.23	2.45± 0.02	1.90± 0.01	19.5	34.7	10.1	0.01	3.0	2
654	224.13771	-1.51432	1.5	···	···	0.61± 0.06	0.31± 0.01	0.16± 0.01	17.8	1.2	14.7	···	0.2	0
655	224.14061	-1.96140	1.1	···	0.42± 0.14	3.12± 0.16	2.92± 0.01	1.91± 0.02	26.0	59.6	8.1	···	1.1	1
656	224.14182	-0.85457	0.8	···	···	0.81± 0.27	0.78± 0.02	0.69± 0.01	20.1	5.4	8.9	···	0.1	1
657	224.14194	-0.34721	0.9	···	···	0.20± 0.04	0.20± 0.01	0.07± 0.01	11.0	0.3	12.2	···	0.0	0
658	224.14420	-1.74118	1.5	0.56± 0.04	1.56± 0.12	5.13± 0.14	4.70± 0.02	1.97± 0.01	21.6	48.7	10.1	0.01	5.0	2
659	224.14648	-1.21325	0.9	···	···	0.40± 0.04	0.38± 0.01	0.20± 0.02	17.7	1.6	10.4	···	0.1	1
660	224.14891	-1.80812	1.1	···	···	6.32± 0.25	4.34± 0.02	2.46± 0.04	30.5	19.2	11.9	···	1.2	1

TABLE 3—*Continued*

ID	ℓ [°]	b [°]	d [kpc]	$F_{70} \pm \Delta F_{70}$ [Jy]	$F_{160} \pm \Delta F_{160}$ [Jy]	$F_{250} \pm \Delta F_{250}$ [Jy]	$F_{350} \pm \Delta F_{350}$ [Jy]	$F_{500} \pm \Delta F_{500}$ [Jy]	r [″]	M [$M_\odot$]	T [K]	F_{22} [Jy]	L_{bol} [$L_\odot$]	unbound/pre-/proto-stellar 0/1/2
661	224.15317	-1.74151	1.5	···	···	4.72± 0.19	5.86± 0.02	3.42± 0.02	26.6	99.9	9.3	···	2.3	1
662	224.15817	-1.74984	1.5	···	···	2.83± 0.13	4.73± 0.01	2.66± 0.01	19.8	109.3	8.5	···	1.7	1
663	224.16173	-1.07454	0.9	···	···	1.63± 0.16	1.63± 0.01	1.36± 0.02	20.2	13.3	8.9	···	0.3	1
664	224.16476	-1.55668	1.5	···	···	1.15± 0.07	0.46± 0.02	0.31± 0.02	22.5	1.8	15.0	···	0.3	0
665	224.16719	-1.76209	1.5	0.11± 0.01	1.33± 0.12	4.96± 0.25	7.55± 0.01	4.53± 0.01	23.1	198.2	8.4	···	4.6	2
666	224.17250	-0.87692	0.8	···	···	1.20± 0.19	0.90± 0.01	0.59± 0.06	31.1	2.7	10.8	···	0.1	1
667	224.17378	-1.97505	1.1	···	···	4.61± 0.42	2.63± 0.02	1.06± 0.04	33.1	4.5	15.6	···	0.7	1
668	224.17648	-1.63467	1.5	···	1.56± 0.06	1.03± 0.06	0.48± 0.02	···	21.0	0.6	20.5	0.04	2.6	2
669	224.17860	-1.76362	1.5	···	···	5.52± 0.22	6.50± 0.02	4.06± 0.02	34.6	117.0	9.2	···	2.6	1
670	224.18361	-0.27953	0.9	···	···	0.45± 0.04	0.40± 0.01	0.22± 0.01	21.6	1.4	10.6	···	0.1	1
671	224.18558	-1.05020	0.9	5.79± 0.10	17.20± 0.24	21.34± 0.28	13.30± 0.01	4.86± 0.02	16.9	15.7	14.1	0.31	12.7	2
672	224.18906	-1.78121	1.5	0.49± 0.07	1.18± 0.08	3.05± 0.23	2.56± 0.01	2.00± 0.04	21.9	41.5	9.8	0.03	3.9	2
673	224.20534	-1.78594	1.5	···	···	2.84± 0.12	2.17± 0.01	1.21± 0.03	24.1	17.8	11.4	···	0.9	1
674	224.20605	-1.50343	1.5	···	···	0.45± 0.07	0.54± 0.01	0.30± 0.01	19.0	8.1	9.5	···	0.2	1
675	224.21378	-1.53713	1.5	···	···	1.09± 0.08	0.64± 0.01	0.30± 0.02	29.3	2.6	14.0	···	0.3	0
676	224.21519	-1.96772	1.1	0.70± 0.05	1.37± 0.13	2.39± 0.19	1.92± 0.01	1.27± 0.03	18.4	11.8	10.9	0.12	2.9	2
677	224.22595	-1.93188	1.1	···	···	3.77± 0.20	2.68± 0.02	1.61± 0.03	31.7	13.9	11.4	···	0.7	1
678	224.22614	-0.86249	0.8	1.54± 0.06	1.15± 0.10	2.05± 0.47	1.32± 0.02	···	19.8	2.6	11.9	0.16	1.8	2
679	224.22694	-1.05284	0.9	11.98± 0.14	26.76± 0.24	28.09± 0.34	14.35± 0.01	6.00± 0.01	19.2	14.8	15.2	0.77	21.8	2
680	224.22977	-1.95120	1.1	···	···	5.91± 0.20	3.15± 0.02	2.43± 0.03	31.4	15.6	11.9	···	1.0	1
681	224.23131	-1.71965	1.5	···	···	3.21± 0.10	1.98± 0.01	1.18± 0.02	25.7	13.2	12.3	···	0.9	1
682	224.23840	-1.09235	0.9	0.77± 0.06	2.58± 0.08	3.60± 0.11	1.76± 0.02	0.63± 0.01	19.4	1.9	14.8	0.18	2.1	2
683	224.23933	-1.96573	1.1	···	1.35± 0.09	3.25± 0.11	1.78± 0.01	···	20.5	9.5	11.4	0.10	2.5	2
684	224.24265	-1.92941	1.1	0.81± 0.04	4.15± 0.11	8.44± 0.37	5.58± 0.01	2.67± 0.05	28.5	24.4	11.7	0.09	5.8	2
685	224.24466	-1.05043	0.9	26.62± 0.19	44.46± 0.40	40.70± 1.02	19.12± 0.02	8.66± 0.01	16.4	21.9	15.2	0.42	36.0	2
686	224.24527	-1.68742	1.5	···	···	0.61± 0.05	0.43± 0.01	0.27± 0.01	16.6	3.8	11.3	···	0.2	1
687	224.24817	-0.92974	0.9	11.60± 0.14	23.87± 0.21	24.01± 0.38	13.16± 0.01	5.43± 0.01	16.8	13.9	15.1	0.94	20.8	2
688	224.25121	-1.66769	1.5	···	···	0.63± 0.12	0.54± 0.03	0.29± 0.02	21.6	4.8	11.0	···	0.2	1
689	224.25194	-1.81851	1.1	···	···	1.45± 0.09	1.52± 0.01	0.91± 0.02	20.2	13.1	9.8	···	0.4	1
690	224.25304	-0.90533	0.9	···	···	3.08± 0.17	3.99± 0.02	3.75± 0.04	28.0	57.7	7.9	···	0.6	1
691	224.25429	-0.84701	0.8	11.27± 0.12	15.20± 0.23	7.27± 0.09	4.52± 0.00	···	8.8	1.6	20.3	0.07	9.9	2
692	224.25441	-0.82933	0.8	1.50± 0.06	6.31± 0.32	11.52± 0.18	7.76± 0.02	···	19.2	16.0	11.7	0.06	3.8	2
693	224.25697	-1.89894	1.1	0.57± 0.05	1.22± 0.11	1.52± 0.09	0.87± 0.02	0.55± 0.02	16.7	3.0	13.0	0.06	2.0	2
694	224.25731	-0.85966	0.8	···	···	12.34± 0.22	14.60± 0.01	11.26± 0.06	26.2	108.9	8.6	···	1.7	1
695	224.25861	-1.14742	0.9	···	···	1.07± 0.07	0.99± 0.01	0.53± 0.02	17.9	3.3	10.6	···	0.1	1
696	224.26027	-1.84953	1.1	···	···	5.15± 0.15	3.81± 0.02	2.51± 0.05	30.4	24.2	10.9	···	1.1	1
697	224.26051	-0.87219	0.8	0.65± 0.02	1.00± 0.09	3.83± 0.24	4.95± 0.01	···	19.8	43.3	8.3	0.06	1.4	2
698	224.26173	-1.08233	0.9	0.65± 0.02	3.27± 0.20	6.31± 0.15	4.34± 0.02	2.35± 0.02	21.0	11.8	11.5	···	2.1	2
699	224.26218	-0.84695	0.8	0.84± 0.04	1.29± 0.11	8.89± 0.14	8.81± 0.01	···	18.0	114.1	7.8	0.24	2.6	2
700	224.26407	-0.82944	0.8	2.91± 0.06	7.01± 0.43	8.83± 0.14	7.43± 0.01	5.65± 0.01	13.9	18.1	11.4	0.06	4.6	2
701	224.26624	-0.20833	0.9	···	···	0.29± 0.05	0.25± 0.01	0.16± 0.01	19.1	1.1	10.3	···	0.0	1
702	224.27173	-0.80352	0.9	0.60± 0.02	1.10± 0.09	2.02± 0.15	3.32± 0.01	1.21± 0.03	15.2	10.9	10.1	0.12	1.7	2
703	224.27226	-1.00414	0.9	···	···	1.06± 0.15	0.84± 0.14	0.45± 0.02	20.0	2.2	11.4	···	0.1	1
704	224.27237	-1.06358	0.9	···	3.98± 0.11	8.80± 0.17	5.49± 0.02	2.63± 0.02	23.3	13.6	11.6	0.02	2.6	2

TABLE 3—*Continued*

ID	ℓ [°]	b [°]	d [kpc]	$F_{70} \pm \Delta F_{70}$ [Jy]	$F_{160} \pm \Delta F_{160}$ [Jy]	$F_{250} \pm \Delta F_{250}$ [Jy]	$F_{350} \pm \Delta F_{350}$ [Jy]	$F_{500} \pm \Delta F_{500}$ [Jy]	r [″]	M [$M_\odot$]	T [K]	F_{22} [Jy]	L_{bol} [$L_\odot$]	unbound/pre-/proto-stellar 0/1/2
705	224.27271	-1.87298	1.1	···	···	2.41± 0.12	2.27± 0.01	1.40± 0.03	23.4	18.5	10.0	···	0.6	1
706	224.27753	-0.83360	0.8	1.43± 0.04	3.25± 0.08	12.29± 0.20	12.73± 0.01	···	20.9	90.5	8.7	0.02	3.5	2
707	224.27759	-1.09282	0.9	0.51± 0.05	2.78± 0.09	5.52± 0.13	3.76± 0.02	2.47± 0.01	17.8	12.2	11.1	0.08	2.2	2
708	224.28355	-1.83463	1.1	···	···	1.21± 0.10	1.12± 0.01	0.84± 0.02	17.9	12.3	9.5	···	0.3	1
709	224.28413	-0.82566	0.9	3.86± 0.06	10.34± 0.24	15.81± 0.19	14.77± 0.01	9.39± 0.02	19.2	55.8	10.9	0.24	10.6	2
710	224.28613	-1.87148	1.1	···	···	3.56± 0.27	3.91± 0.01	1.78± 0.04	26.7	21.7	10.5	···	0.9	1
711	224.28912	-1.95968	1.1	2.16± 0.06	3.70± 0.13	3.98± 0.22	2.58± 0.01	1.16± 0.02	17.8	5.7	13.9	0.16	5.8	2
712	224.28986	-0.78891	0.9	0.50± 0.01	0.53± 0.08	1.36± 0.15	1.09± 0.01	···	10.6	5.6	10.1	0.01	0.8	2
713	224.29196	-1.10102	0.9	···	3.40± 0.12	6.72± 0.17	5.14± 0.01	2.45± 0.01	24.9	13.2	11.4	0.05	2.5	2
714	224.29425	-1.90722	1.1	···	···	2.03± 0.19	1.94± 0.03	1.19± 0.03	23.8	14.0	10.0	···	0.4	1
715	224.29572	-0.87371	0.8	0.32± 0.03	0.80± 0.09	1.20± 0.18	0.91± 0.01	···	11.8	1.7	12.0	···	0.4	2
716	224.29828	-1.07302	0.9	1.12± 0.04	5.65± 0.13	10.23± 0.20	6.18± 0.01	3.63± 0.02	28.7	15.5	11.9	0.12	4.1	2
717	224.30237	-1.09298	0.9	···	3.06± 0.09	5.01± 0.25	2.35± 0.01	···	30.9	3.9	13.4	0.21	2.7	2
718	224.30237	-0.78053	0.9	0.59± 0.03	1.64± 0.09	2.99± 0.19	3.65± 0.02	···	17.4	15.4	10.2	0.02	1.8	2
719	224.30763	-1.03771	0.9	0.70± 0.02	1.33± 0.10	2.16± 0.23	2.32± 0.01	1.10± 0.01	14.8	6.5	10.9	0.09	1.5	2
720	224.30861	-1.85701	1.1	···	···	2.13± 0.58	2.84± 0.59	1.43± 0.05	33.0	22.1	9.4	···	0.6	1
721	224.30872	-0.81765	0.9	7.02± 0.11	7.37± 0.18	9.68± 0.28	8.55± 0.01	···	19.7	19.8	12.0	0.59	11.8	2
722	224.31158	-1.06185	0.9	···	1.07± 0.12	3.29± 0.20	3.18± 0.01	1.25± 0.01	17.1	10.8	10.1	···	0.7	1
723	224.31836	-1.04701	0.9	···	···	6.12± 0.19	6.56± 0.01	4.61± 0.02	30.0	44.0	9.2	···	0.9	1
724	224.32008	-1.97435	1.1	1.19± 0.06	2.18± 0.12	3.06± 0.16	2.04± 0.01	···	15.5	6.1	12.7	0.25	4.1	2
725	224.32224	-0.84937	0.9	4.29± 0.08	6.19± 0.16	8.26± 0.14	5.65± 0.01	···	20.2	11.6	12.8	3.13	13.5	2
726	224.32617	-0.66555	0.9	···	···	0.64± 0.10	0.50± 0.02	0.21± 0.03	21.6	1.0	12.7	···	0.1	0
727	224.32619	-1.06262	0.9	···	1.33± 0.08	5.75± 0.16	4.11± 0.01	2.08± 0.02	26.2	19.6	9.7	0.05	1.6	2
728	224.33194	-0.84212	0.9	···	···	2.19± 0.16	2.82± 0.01	2.28± 0.04	15.5	35.8	8.3	···	0.5	1
729	224.33252	-1.97626	1.1	2.20± 0.07	4.65± 0.16	6.36± 0.20	4.20± 0.02	2.02± 0.04	19.0	15.2	12.3	0.14	6.8	2
730	224.33328	-0.54790	0.7	···	···	3.25± 0.38	2.79± 0.03	2.29± 0.05	35.3	12.4	9.5	···	0.3	1
731	224.33340	-0.74788	0.9	9.19± 0.12	13.25± 0.21	11.07± 0.28	5.30± 0.02	1.74± 0.01	11.0	4.0	17.7	1.04	16.7	2
732	224.33589	-0.64171	0.9	···	···	0.72± 0.11	0.67± 0.02	0.36± 0.03	25.0	2.5	10.7	···	0.1	1
733	224.33864	-0.58645	0.9	···	···	0.87± 0.06	0.97± 0.01	0.63± 0.01	17.3	6.8	9.3	···	0.2	1
734	224.33873	-0.56758	0.7	···	···	1.85± 0.08	1.78± 0.01	1.21± 0.02	24.5	6.7	9.7	···	0.2	1
735	224.34319	-1.02459	0.9	2.36± 0.05	7.07± 0.14	12.90± 0.12	9.17± 0.01	5.28± 0.05	18.7	26.1	11.4	0.36	6.6	2
736	224.34431	-1.03567	0.9	···	0.70± 0.25	7.02± 0.15	6.78± 0.01	3.61± 0.04	22.6	48.8	8.3	···	1.3	1
737	224.34552	-0.60799	0.9	···	···	0.94± 0.17	1.29± 0.01	0.48± 0.50	18.3	3.8	10.5	···	0.2	1
738	224.34567	-0.60120	0.9	···	···	1.21± 0.12	0.60± 0.01	0.50± 0.67	23.7	1.8	12.2	···	0.1	1
739	224.34605	-0.73986	0.9	1.50± 0.04	2.42± 0.12	3.83± 0.23	2.82± 0.01	1.45± 0.01	16.2	7.6	11.9	0.11	3.1	2
740	224.34805	-0.51413	0.7	···	···	0.84± 0.06	0.83± 0.01	0.69± 0.02	23.9	4.3	9.1	···	0.1	1
741	224.34972	-2.01393	1.1	32.38± 0.36	118.75± 0.48	108.75± 0.76	57.16± 0.00	22.34± 0.02	16.5	83.6	15.9	6.40	137.8	2
742	224.35103	-0.97620	0.9	···	···	1.12± 0.11	1.19± 0.01	1.04± 0.02	26.4	11.3	8.6	···	0.2	1
743	224.35159	-0.49287	0.7	···	···	1.89± 0.14	2.40± 0.01	1.41± 0.03	26.8	10.4	9.1	···	0.2	1
744	224.35844	-2.02430	1.1	5.99± 0.13	11.92± 0.29	13.82± 0.33	11.56± 0.00	5.86± 0.01	10.1	35.8	12.4	0.80	19.6	2
745	224.36429	-0.57453	0.9	···	···	0.41± 0.08	0.49± 0.01	0.30± 0.02	13.0	3.3	9.3	···	0.1	1
746	224.36475	-2.05118	1.1	5.41± 0.05	9.82± 0.23	9.97± 0.33	7.22± 0.02	···	21.7	15.2	13.6	0.51	14.5	2
747	224.36488	-2.07441	1.1	···	3.25± 0.11	7.06± 0.19	3.65± 0.01	2.76± 0.09	25.7	18.4	11.4	0.08	4.0	2
748	224.36807	-2.08531	1.1	···	7.08± 0.34	7.74± 0.46	5.82± 0.02	···	31.1	12.3	13.6	0.13	7.0	2

TABLE 3—*Continued*

ID	ℓ [°]	b [°]	d [kpc]	$F_{70} \pm \Delta F_{70}$ [Jy]	$F_{160} \pm \Delta F_{160}$ [Jy]	$F_{250} \pm \Delta F_{250}$ [Jy]	$F_{350} \pm \Delta F_{350}$ [Jy]	$F_{500} \pm \Delta F_{500}$ [Jy]	r [″]	M [$M_\odot$]	T [K]	F_{22} [Jy]	L_{bol} [$L_\odot$]	unbound/pre-/proto-stellar 0/1/2
749	224.36986	-0.72598	0.9	3.91± 0.07	4.59± 0.14	4.32± 0.15	2.35± 0.01	0.94± 0.02	12.2	3.2	15.2	0.06	5.2	2
750	224.36990	-2.02941	1.1	1.05± 0.05	3.91± 0.25	8.63± 0.20	11.05± 0.01	···	17.1	90.1	9.5	0.07	6.2	2
751	224.37210	-1.93678	1.1	···	···	2.75± 1.69	2.58± 0.02	1.89± 0.03	27.9	24.7	9.5	···	0.6	1
752	224.37325	-0.47919	0.7	···	···	0.79± 0.07	0.83± 0.01	0.54± 0.02	25.8	3.3	9.5	···	0.1	1
753	224.37488	-2.04791	1.1	2.99± 0.07	6.37± 0.19	7.57± 0.26	5.13± 0.02	2.52± 0.01	16.1	13.9	13.1	0.24	9.3	2
754	224.37862	-1.92086	1.1	···	···	3.75± 0.16	3.10± 0.01	1.85± 0.04	30.6	15.7	11.1	···	0.7	1
755	224.38319	-1.01548	0.9	2.92± 0.07	5.15± 0.15	5.41± 0.17	2.74± 0.01	1.27± 0.02	12.7	3.2	15.0	0.16	4.7	2
756	224.38483	-0.84225	0.9	···	···	1.48± 0.08	1.34± 0.01	0.73± 0.03	23.0	5.2	10.7	···	0.2	1
757	224.39241	-1.98039	1.1	···	···	1.75± 0.20	1.08± 0.01	0.57± 0.03	21.7	3.2	12.9	···	0.3	1
758	224.39384	-0.70904	0.9	0.86± 0.04	4.91± 0.14	8.59± 0.22	7.04± 0.01	4.33± 0.03	18.1	26.4	11.1	0.03	4.0	2
759	224.39561	-1.95779	1.1	···	···	1.97± 0.11	1.97± 0.01	1.17± 0.01	18.5	14.4	9.9	···	0.4	1
760	224.39606	-0.72510	0.9	4.27± 0.08	5.76± 0.14	6.03± 0.23	3.18± 0.01	1.77± 0.02	12.4	5.2	14.3	0.16	6.7	2
761	224.40646	-0.93984	0.9	0.25± 0.01	···	0.81± 0.07	0.38± 0.02	···	23.4	0.2	19.3	···	0.3	2
762	224.40698	-1.04630	0.9	···	···	1.56± 0.14	0.93± 0.02	0.56± 0.04	24.4	2.0	12.5	···	0.1	1
763	224.40718	-0.69299	0.9	14.90± 0.15	52.22± 0.57	50.50± 0.40	31.53± 0.03	12.87± 0.09	17.7	40.4	14.7	0.15	35.6	2
764	224.40807	-0.73863	0.9	1.13± 0.04	2.77± 0.11	3.25± 0.06	1.55± 0.01	1.00± 0.01	6.9	2.8	14.1	0.01	2.2	2
765	224.41164	-2.09036	1.1	1.73± 0.08	2.18± 0.11	1.53± 0.11	0.75± 0.02	···	13.4	0.8	17.9	0.07	3.5	2
766	224.41360	-1.95621	1.1	···	···	2.20± 0.20	1.91± 0.02	0.90± 0.01	24.2	7.2	11.6	···	0.4	1
767	224.41409	-1.27196	0.9	···	···	0.81± 0.06	0.66± 0.02	0.39± 0.03	20.6	2.6	10.9	···	0.1	1
768	224.42081	-0.69778	0.9	8.15± 0.11	35.00± 0.25	43.61± 0.39	25.01± 0.03	11.42± 0.08	18.0	41.7	13.6	0.71	26.7	2
769	224.42430	-0.55163	0.9	···	···	2.05± 0.35	2.96± 0.02	2.07± 0.04	32.9	33.2	8.3	···	0.5	1
770	224.42996	-2.03730	1.1	0.41± 0.04	1.44± 0.23	2.81± 0.24	3.17± 0.03	···	25.1	20.5	10.1	0.07	2.3	2
771	224.43195	-0.94217	1.0	···	···	0.89± 0.09	0.71± 0.01	0.42± 0.02	27.3	3.4	10.9	···	0.2	1
772	224.43466	-0.78151	0.9	···	···	1.26± 0.13	1.26± 0.01	0.95± 0.04	23.7	9.9	9.2	···	0.2	1
773	224.43645	-0.28002	0.9	···	···	0.66± 0.05	0.58± 0.02	0.28± 0.02	21.6	1.8	11.4	···	0.1	1
774	224.44051	-0.67038	0.9	0.32± 0.02	0.76± 0.07	2.76± 0.21	1.96± 0.01	1.06± 0.03	26.2	10.2	9.9	0.13	1.3	2
775	224.44063	-0.57954	0.9	···	···	1.04± 0.15	1.23± 0.03	0.91± 0.04	27.3	11.7	8.7	···	0.2	1
776	224.44110	-0.60414	0.9	0.39± 0.01	1.24± 0.08	2.66± 0.16	2.41± 0.02	1.03± 0.03	14.9	6.8	11.1	···	1.1	2
777	224.44452	-2.04066	1.1	3.36± 0.06	3.88± 0.12	8.00± 0.39	7.09± 0.05	4.39± 0.01	18.2	44.4	10.4	0.40	9.7	2
778	224.44487	-2.10022	0.9	···	···	1.32± 0.16	1.23± 0.02	0.61± 0.02	24.5	5.4	10.1	···	0.2	1
779	224.44861	-0.31915	1.0	···	···	0.35± 0.05	0.21± 0.01	0.11± 0.04	21.6	0.5	13.2	···	0.0	0
780	224.45079	-0.70513	0.9	0.65± 0.03	1.08± 0.09	2.29± 0.23	1.76± 0.02	1.40± 0.03	20.8	8.7	10.4	0.31	2.1	2
781	224.45212	-2.03425	1.1	···	0.92± 0.10	2.36± 0.20	4.57± 0.04	···	15.5	53.9	8.5	0.08	2.2	2
782	224.45479	-1.99367	1.1	···	···	1.28± 0.08	0.83± 0.01	0.39± 0.01	20.2	1.8	13.6	···	0.2	1
783	224.45528	-1.09919	1.0	···	···	0.75± 0.09	0.33± 0.04	0.20± 0.01	19.8	0.6	14.8	···	0.1	0
784	224.45647	-0.67829	0.9	3.88± 0.08	5.36± 0.14	3.41± 0.19	1.50± 0.01	0.59± 0.02	6.6	1.0	19.2	0.85	7.8	2
785	224.45924	-0.59018	0.9	···	···	1.43± 0.10	1.43± 0.01	0.81± 0.02	29.9	7.0	10.1	···	0.2	1
786	224.46394	-0.49888	1.0	···	···	0.70± 0.07	1.18± 0.01	0.92± 0.02	19.7	21.4	7.8	···	0.2	1
787	224.46959	-2.03874	1.1	···	···	4.00± 0.20	9.95± 0.07	6.52± 0.02	25.8	226.6	7.4	···	1.9	1
788	224.47148	-0.63852	0.9	0.65± 0.04	···	4.83± 0.26	5.55± 0.03	2.31± 0.02	27.8	15.7	11.1	0.04	2.5	2
789	224.47331	-0.69497	0.9	1.95± 0.05	6.00± 0.14	4.68± 0.10	3.83± 0.02	1.09± 0.02	11.7	3.1	15.7	···	3.5	2
790	224.47818	-0.30780	1.0	···	0.20± 0.05	0.50± 0.05	0.35± 0.01	0.17± 0.03	18.6	1.5	10.9	0.01	0.2	2
791	224.48149	-0.62037	0.9	3.71± 0.07	5.65± 0.15	5.61± 0.23	3.30± 0.01	1.99± 0.01	11.4	5.8	13.9	0.12	6.1	2
792	224.48274	-0.63637	0.9	7.04± 0.11	17.11± 0.21	20.96± 0.19	14.92± 0.07	7.45± 0.01	19.3	30.0	12.9	0.84	17.7	2

TABLE 3—*Continued*

ID	ℓ [°]	b [°]	d [kpc]	$F_{70} \pm \Delta F_{70}$ [Jy]	$F_{160} \pm \Delta F_{160}$ [Jy]	$F_{250} \pm \Delta F_{250}$ [Jy]	$F_{350} \pm \Delta F_{350}$ [Jy]	$F_{500} \pm \Delta F_{500}$ [Jy]	r [″]	M [$M_\odot$]	T [K]	F_{22} [Jy]	L_{bol} [$L_\odot$]	unbound/pre-/proto-stellar 0/1/2
793	224.48524	-0.57152	0.9	···	···	1.69± 0.13	1.63± 0.01	1.32± 0.02	19.0	13.7	9.1	···	0.3	1
794	224.48857	-2.04304	1.1	0.61± 0.03	0.82± 0.08	3.29± 0.22	3.20± 0.02	2.51± 0.02	22.0	45.5	8.7	···	1.8	2
795	224.49171	-0.66233	0.9	1.03± 0.04	1.02± 0.09	3.38± 0.14	1.32± 0.06	···	18.2	4.5	11.5	0.31	2.5	2
796	224.49431	-0.66956	0.9	···	···	2.86± 0.17	3.83± 0.07	3.48± 0.01	21.6	48.8	8.3	···	0.7	1
797	224.50319	-1.00619	1.0	3.05± 0.07	3.65± 0.13	3.85± 0.19	2.15± 0.01	0.98± 0.01	16.1	3.9	14.5	0.65	7.8	2
798	224.50848	-2.03491	0.9	···	···	3.44± 0.21	3.13± 0.01	0.98± 0.01	17.0	4.0	13.6	···	0.4	1
799	224.50963	-2.02642	1.1	5.42± 0.07	10.45± 0.19	11.49± 0.55	5.90± 0.01	2.74± 0.01	13.0	11.6	14.7	0.08	13.2	2
800	224.51379	-0.90886	1.0	0.46± 0.02	0.58± 0.07	1.44± 0.11	1.18± 0.01	0.66± 0.02	18.5	6.7	10.4	···	0.8	2
801	224.52808	-2.03471	1.2	1.13± 0.04	2.19± 0.06	8.87± 0.28	7.95± 0.04	5.23± 0.03	29.5	104.3	9.1	0.14	6.5	2
802	224.52951	-0.49673	1.0	···	···	0.58± 0.06	0.57± 0.01	0.31± 0.02	17.1	2.6	10.5	···	0.1	1
803	224.53252	-1.20667	0.9	···	···	0.84± 0.07	0.60± 0.02	0.34± 0.02	26.0	1.8	11.7	···	0.1	1
804	224.53329	-0.93453	1.0	···	···	0.48± 0.09	0.36± 0.01	0.16± 0.02	17.0	1.5	11.1	···	0.1	1
805	224.53442	-1.94454	1.2	···	···	1.12± 0.15	0.56± 0.02	0.31± 0.04	28.4	1.6	14.3	···	0.2	0
806	224.53529	-0.29120	1.0	···	···	0.78± 0.07	0.59± 0.02	0.44± 0.02	25.5	3.6	10.3	···	0.1	1
807	224.54027	-0.85986	1.0	···	···	1.23± 0.10	1.03± 0.02	0.52± 0.03	24.6	3.8	11.6	···	0.2	1
808	224.54694	-0.58687	0.9	···	···	1.94± 0.09	2.50± 0.06	1.65± 0.05	23.0	21.7	8.8	···	0.4	1
809	224.55096	-0.44592	1.0	···	···	0.44± 0.06	0.44± 0.01	0.26± 0.02	17.6	2.5	10.1	···	0.1	1
810	224.55194	-0.57854	0.9	···	···	0.95± 0.07	1.83± 0.05	0.85± 0.03	19.1	13.0	8.6	···	0.2	1
811	224.55296	-0.98574	1.0	1.07± 0.03	1.37± 0.10	1.53± 0.12	0.93± 0.02	0.44± 0.02	13.5	1.3	14.8	0.02	2.0	2
812	224.56255	-0.84683	1.0	···	···	0.37± 0.04	0.35± 0.01	0.27± 0.02	15.1	3.4	9.3	···	0.1	1
813	224.56438	-0.88288	1.0	···	···	0.42± 0.05	0.36± 0.01	0.17± 0.03	21.6	1.2	11.6	···	0.1	0
814	224.56554	-1.82345	1.2	···	···	3.06± 0.13	3.33± 0.01	1.17± 23.36	28.9	12.5	11.7	···	0.8	1
815	224.58261	-0.96758	1.0	···	···	1.62± 0.21	1.80± 0.02	0.80± 0.03	29.5	7.8	10.6	···	0.3	1
816	224.58485	-2.01319	1.0	···	···	0.79± 0.16	0.83± 0.02	0.59± 0.02	23.5	7.6	9.2	···	0.2	1
817	224.58771	-0.55345	1.0	···	···	1.56± 0.10	1.81± 0.02	1.79± 0.02	28.1	32.2	8.1	···	0.4	1
818	224.59193	-1.88837	1.2	···	···	0.34± 0.07	0.48± 0.01	0.33± 0.01	21.4	8.8	8.5	···	0.1	1
819	224.59361	-0.62799	0.9	···	···	0.47± 0.07	0.44± 0.02	0.22± 0.03	20.6	1.4	11.0	···	0.1	1
820	224.59508	-2.08921	1.2	···	···	1.04± 0.12	0.67± 0.01	0.19± 0.04	30.5	0.7	17.6	···	0.2	0
821	224.59752	-0.48059	1.0	···	···	1.03± 0.15	1.10± 0.02	0.86± 0.03	28.0	11.6	8.9	···	0.2	1
822	224.59766	-1.18078	1.1	···	0.24± 0.05	1.12± 0.21	0.87± 0.01	0.50± 0.02	18.6	8.6	9.1	0.01	0.5	2
823	224.60117	-1.82321	1.2	···	0.78± 0.09	1.42± 0.15	1.25± 0.01	···	26.3	7.9	10.9	···	0.7	1
824	224.60210	-0.92914	1.0	···	···	0.94± 0.07	0.89± 0.05	0.53± 0.01	24.2	5.5	10.1	···	0.2	1
825	224.60228	-1.66645	0.9	···	···	0.65± 0.10	0.48± 0.01	0.23± 0.04	23.5	1.0	12.4	···	0.1	0
826	224.60686	-0.90836	1.0	···	···	0.42± 0.09	0.34± 0.01	0.26± 0.01	17.5	3.0	9.7	···	0.1	1
827	224.60736	-1.00611	1.0	165.79± 0.50	103.63± 0.41	57.05± 0.46	23.51± 0.02	10.56± 0.01	16.2	18.4	20.4	28.75	324.2	2
828	224.61028	-0.45717	1.0	···	···	1.01± 0.07	1.19± 0.03	0.47± 0.04	23.2	4.1	10.8	···	0.2	1
829	224.61038	-1.00273	1.0	42.50± 0.25	60.76± 0.24	61.95± 0.62	20.80± 0.02	···	22.7	22.7	17.8	0.44	75.9	2
830	224.61362	-0.49869	1.0	···	···	0.76± 0.12	0.80± 0.02	0.68± 0.03	23.1	9.6	8.7	···	0.2	1
831	224.61528	-1.61775	1.0	···	···	1.16± 0.08	1.23± 0.01	0.77± 0.02	26.0	8.3	9.6	···	0.2	1
832	224.61574	-1.33985	1.1	···	···	0.32± 0.06	0.26± 0.01	0.18± 0.01	18.2	1.8	10.3	···	0.1	1
833	224.61826	-1.13431	1.0	···	···	0.70± 0.08	0.62± 0.01	0.49± 0.01	23.6	5.5	9.5	···	0.1	1
834	224.62444	-2.03529	1.0	···	···	0.57± 0.11	0.42± 0.02	0.20± 0.02	20.8	1.2	12.3	···	0.1	0
835	224.62511	-0.48293	1.0	···	···	1.18± 0.10	1.42± 0.02	1.24± 0.05	24.3	21.8	8.3	···	0.3	1
836	224.62695	-0.44340	1.0	···	···	0.78± 0.12	0.92± 0.01	0.60± 0.02	23.6	8.2	9.1	···	0.2	1

TABLE 3—*Continued*

ID	ℓ [°]	b [°]	d [kpc]	$F_{70} \pm \Delta F_{70}$ [Jy]	$F_{160} \pm \Delta F_{160}$ [Jy]	$F_{250} \pm \Delta F_{250}$ [Jy]	$F_{350} \pm \Delta F_{350}$ [Jy]	$F_{500} \pm \Delta F_{500}$ [Jy]	r [″]	M [$M_\odot$]	T [K]	F_{22} [Jy]	L_{bol} [$L_\odot$]	unbound/pre-/proto-stellar 0/1/2
837	224.62845	-1.61949	1.0	···	···	0.80± 0.16	1.31± 0.03	0.59± 0.02	28.9	8.0	9.2	···	0.2	1
838	224.64122	-0.79287	1.0	···	···	0.52± 0.04	0.42± 0.01	0.24± 0.09	20.2	1.6	11.6	···	0.1	1
839	224.64362	-0.88681	1.0	···	···	0.85± 0.06	0.69± 0.01	0.31± 0.04	24.5	2.1	12.0	···	0.1	1
840	224.64377	-1.60225	1.0	···	···	0.85± 0.09	0.62± 0.02	0.32± 0.02	20.1	1.8	12.0	···	0.1	1
841	224.64528	-1.02545	1.0	···	···	2.19± 0.11	3.06± 0.02	1.11± 0.04	23.8	11.6	10.5	···	0.5	1
842	224.64560	-1.12209	1.0	···	···	0.87± 0.08	0.60± 0.02	0.26± 0.02	25.8	1.3	13.2	···	0.1	0
843	224.64622	-0.80120	1.0	···	···	0.65± 0.05	0.48± 0.01	0.21± 0.11	23.3	1.2	12.8	···	0.1	0
844	224.64824	-0.43994	1.0	···	···	0.68± 0.11	0.83± 0.01	0.67± 0.01	12.1	11.2	8.4	···	0.2	1
845	224.64903	-0.54439	1.0	···	···	0.82± 0.06	0.91± 0.03	0.41± 0.03	26.0	3.7	10.5	···	0.2	1
846	224.65298	-1.58222	1.0	···	···	1.11± 0.07	0.95± 0.01	0.44± 0.03	24.1	2.7	11.7	···	0.2	1
847	224.65338	-1.76353	1.0	···	···	3.16± 0.11	2.76± 0.01	1.60± 0.03	25.1	14.5	10.6	···	0.6	1
848	224.65628	-1.89188	1.2	···	···	0.42± 0.06	0.28± 0.02	0.14± 0.02	17.6	1.0	13.0	···	0.1	0
849	224.65878	-1.78735	1.2	···	···	1.46± 0.10	0.96± 0.02	0.64± 0.02	27.0	6.0	11.4	···	0.3	1
850	224.66942	-1.56488	1.0	···	···	1.00± 0.17	0.91± 0.02	0.48± 0.03	26.2	3.6	10.8	···	0.2	1
851	224.67023	-0.48120	1.0	···	···	0.38± 0.08	0.51± 0.03	0.25± 0.01	17.9	3.1	9.5	···	0.1	1
852	224.67027	-0.39621	1.0	···	···	1.11± 0.14	1.23± 0.01	0.74± 0.04	24.6	8.7	9.5	···	0.2	1
853	224.67284	-1.03862	1.1	···	···	1.23± 0.07	1.06± 0.01	0.65± 0.02	17.9	7.1	10.5	···	0.3	1
854	224.68654	-1.49524	1.0	···	···	0.57± 0.08	0.44± 0.02	0.20± 0.03	25.5	1.1	12.3	···	0.1	0
855	224.69101	-0.99227	1.1	···	···	2.21± 0.19	1.50± 0.03	0.90± 0.04	34.9	6.8	11.7	···	0.4	1
856	224.69597	-1.66223	1.0	···	···	0.93± 0.07	0.49± 0.01	0.37± 0.02	23.3	1.9	12.0	···	0.1	1
857	224.71361	-1.82883	1.2	···	···	1.92± 0.19	1.20± 0.01	0.93± 0.03	31.8	8.3	11.1	···	0.4	1
858	224.71526	-0.99539	1.1	0.78± 0.03	2.68± 0.14	4.98± 0.17	3.61± 0.03	1.59± 0.02	23.4	13.8	11.8	0.13	4.2	2
859	224.72194	-0.99885	1.1	···	···	4.05± 0.11	2.74± 0.01	1.56± 0.02	25.6	12.6	11.7	···	0.7	1
860	224.72362	-0.23369	0.7	···	···	0.33± 0.05	0.23± 0.02	0.13± 0.03	21.6	0.4	11.7	···	0.0	0
861	224.72626	-1.58336	1.0	···	···	0.51± 0.09	0.59± 0.01	0.49± 0.01	14.3	8.6	8.5	···	0.1	1
862	224.73573	-1.82862	1.0	···	···	2.03± 0.10	1.87± 0.05	1.02± 0.04	27.0	10.5	10.1	···	0.4	1
863	224.73793	-0.33488	1.0	···	···	0.51± 0.05	0.35± 0.01	0.17± 0.02	17.3	0.8	12.7	···	0.1	0
864	224.74095	-1.81590	1.0	···	···	2.88± 0.13	2.09± 0.02	1.92± 0.06	28.1	18.4	9.7	···	0.5	1
865	224.75027	-1.56005	1.2	···	···	0.93± 0.14	0.68± 0.02	0.57± 0.02	28.0	6.9	10.1	···	0.2	1
866	224.75464	-1.01729	1.1	···	···	1.78± 0.11	2.77± 0.02	2.06± 0.03	26.0	57.6	8.0	···	0.7	1
867	224.75885	-1.75132	1.0	···	···	3.63± 0.30	5.71± 0.02	3.50± 0.02	28.8	71.1	8.4	···	1.1	1
868	224.76343	-0.20556	1.0	1.22± 0.05	3.29± 0.09	2.86± 0.11	1.38± 0.02	0.54± 0.03	14.6	1.4	16.8	0.05	3.0	2
869	224.76361	-0.48820	1.0	···	···	0.72± 0.06	0.60± 0.01	0.40± 0.01	20.9	3.3	10.2	···	0.1	1
870	224.76541	-1.81522	1.0	0.65± 0.03	3.32± 0.14	5.37± 0.17	3.38± 0.01	2.00± 0.01	14.3	11.9	12.1	···	2.8	2
871	224.76581	-1.49407	1.2	···	···	0.98± 0.17	0.56± 0.01	0.28± 0.03	25.4	1.7	13.8	···	0.2	0
872	224.78360	-1.81372	1.0	···	···	7.36± 0.25	4.62± 0.03	2.38± 0.02	35.7	12.1	13.0	···	1.0	1
873	224.78464	-1.57732	1.2	···	···	0.95± 0.05	0.69± 0.02	0.35± 0.02	22.1	3.1	12.1	···	0.2	1
874	224.79005	-1.69666	1.0	···	···	2.50± 0.09	1.67± 0.01	0.96± 0.01	19.6	6.2	11.7	···	0.4	1
875	224.79051	-1.73547	1.0	56.16± 0.28	68.84± 0.48	42.87± 0.26	20.46± 0.02	8.27± 0.02	21.0	15.7	19.3	6.45	119.7	2
876	224.79312	-0.32209	1.0	···	···	0.58± 0.07	0.54± 0.04	0.28± 0.02	24.8	1.8	11.1	···	0.1	1
877	224.79527	-0.55227	1.0	···	···	0.60± 0.05	0.47± 0.02	0.11± 0.16	24.3	0.3	17.1	···	0.1	0
878	224.79610	-0.39721	1.0	···	···	0.41± 0.05	0.32± 0.01	0.17± 0.02	19.8	1.1	11.3	···	0.1	1
879	224.79659	-1.26037	0.7	···	···	0.23± 0.41	0.21± 0.01	0.13± 0.02	16.1	0.7	10.1	···	0.0	1
880	224.80194	-1.53094	1.2	···	···	0.96± 0.09	0.72± 0.02	0.40± 0.01	23.3	4.0	11.4	···	0.2	1

TABLE 3—*Continued*

ID	ℓ [°]	b [°]	d [kpc]	$F_{70} \pm \Delta F_{70}$ [Jy]	$F_{160} \pm \Delta F_{160}$ [Jy]	$F_{250} \pm \Delta F_{250}$ [Jy]	$F_{350} \pm \Delta F_{350}$ [Jy]	$F_{500} \pm \Delta F_{500}$ [Jy]	r [″]	M [$M_\odot$]	T [K]	F_{22} [Jy]	L_{bol} [$L_\odot$]	unbound/pre-/proto-stellar 0/1/2
881	224.80695	-1.21035	0.7	···	···	0.45± 0.03	0.30± 0.01	0.17± 0.03	20.9	0.5	12.1	···	0.0	0
882	224.80702	-0.62801	1.0	···	···	0.44± 0.04	0.32± 0.02	0.17± 0.02	23.6	1.0	11.9	···	0.1	0
883	224.81694	-1.80619	1.0	···	···	1.07± 0.08	0.78± 0.01	0.61± 0.01	17.3	5.3	10.3	···	0.2	1
884	224.82162	-0.18720	1.0	···	···	0.30± 0.04	0.19± 0.02	0.12± 0.02	19.2	0.6	12.0	···	0.0	0
885	224.83861	-1.79430	1.0	···	···	1.16± 0.08	0.82± 0.02	0.60± 0.03	25.0	4.3	11.1	···	0.2	1
886	224.87282	-1.50561	1.2	···	···	0.37± 0.04	0.31± 0.01	0.25± 0.04	17.1	3.9	9.6	···	0.1	1
887	224.88478	-1.56939	1.2	···	···	0.19± 0.06	0.21± 0.02	0.17± 0.03	17.4	3.9	8.6	···	0.1	1
888	224.89590	-0.47621	1.0	···	···	0.20± 0.08	0.22± 0.01	0.15± 0.02	21.9	2.0	9.1	···	0.0	1
889	224.89636	-1.25150	0.5	5.43± 0.09	11.80± 0.19	10.17± 0.22	5.14± 0.01	2.02± 0.01	10.4	1.4	16.5	0.03	2.6	2
890	224.90585	-1.06103	0.7	0.24± 0.01	0.38± 0.06	0.21± 0.05	0.09± 0.01	···	10.8	0.0	21.9	0.01	0.2	2
891	224.93352	-0.36715	1.0	···	···	0.49± 0.17	0.35± 0.01	0.22± 0.02	26.9	1.4	11.1	···	0.1	1
892	224.96158	-1.17452	0.5	···	···	1.09± 0.07	0.76± 0.02	0.46± 0.04	23.6	0.7	11.5	···	0.0	1
893	224.98445	-0.56287	0.9	···	···	0.94± 0.07	0.75± 0.03	0.64± 0.02	27.7	5.7	9.6	···	0.2	1
894	225.00194	-0.57490	0.9	···	···	0.64± 0.10	0.54± 0.04	0.49± 0.02	24.1	4.8	9.3	···	0.1	1
895	225.01230	-1.59009	1.2	···	···	0.34± 0.03	0.27± 0.01	0.18± 0.01	17.1	2.4	10.1	···	0.1	1
896	225.02200	-0.29787	1.1	···	···	0.30± 0.07	0.29± 0.01	0.17± 0.01	16.8	1.8	10.2	···	0.1	1
897	225.02840	-1.06934	0.7	···	···	0.28± 0.07	0.25± 0.01	0.16± 0.02	12.7	0.7	10.3	···	0.0	1
898	225.03256	-1.09176	0.5	···	···	1.48± 0.08	1.08± 0.01	0.69± 0.02	25.0	1.2	11.0	···	0.1	1
899	225.06194	-1.09620	0.5	···	···	1.20± 0.09	1.03± 0.01	0.45± 0.04	23.1	0.7	11.9	···	0.0	1
900	225.08028	-1.06736	0.8	···	···	0.29± 0.06	0.23± 0.01	0.12± 0.02	13.4	0.5	11.6	···	0.0	0
901	225.08528	-1.03807	0.8	···	···	1.55± 0.08	0.96± 0.03	0.55± 0.04	34.3	1.8	12.5	···	0.1	1
902	225.08731	-0.60464	0.9	···	···	0.73± 0.11	0.78± 0.01	0.70± 0.03	24.2	9.8	8.5	···	0.1	1
903	225.12480	-0.97596	0.8	···	···	0.55± 0.07	0.44± 0.03	0.28± 0.02	24.1	1.5	10.7	···	0.1	1
904	225.14886	-0.97551	0.9	···	···	0.34± 0.07	0.57± 0.01	0.23± 0.01	13.4	2.4	9.5	···	0.1	1
905	225.15724	-0.98628	0.8	···	···	0.96± 0.10	1.15± 0.01	0.64± 0.02	21.2	5.1	9.5	···	0.1	1
906	225.16586	-0.30381	0.9	···	···	1.13± 0.22	0.72± 0.03	0.38± 0.02	37.8	1.5	12.8	···	0.1	0
907	225.17249	-0.89954	0.9	···	···	1.36± 0.23	1.17± 0.01	0.62± 0.04	30.4	3.7	11.0	···	0.2	1
908	225.17525	-0.91053	0.9	···	···	1.09± 0.08	1.19± 0.01	0.57± 0.04	28.4	4.1	10.4	···	0.2	1
909	225.17958	-0.24130	0.9	···	···	0.57± 0.05	0.43± 0.01	0.41± 0.01	17.8	3.0	9.7	···	0.1	1
910	225.19249	-0.84152	0.9	···	···	1.11± 0.17	0.72± 0.02	0.52± 0.02	35.7	2.6	11.1	···	0.1	1
911	225.21861	-0.64243	1.3	···	···	0.43± 0.04	0.23± 0.01	0.14± 0.02	17.6	0.9	13.3	···	0.1	0
912	225.22267	-0.26993	0.9	···	0.58± 0.06	1.07± 0.10	0.83± 0.02	0.29± 0.02	14.3	1.5	12.3	···	0.3	1
913	225.22701	-0.96323	0.9	···	···	0.57± 0.07	0.41± 0.01	0.28± 0.02	25.1	1.6	10.8	···	0.1	1
914	225.24666	-0.23131	1.1	···	···	1.89± 0.10	1.78± 0.01	0.82± 0.09	26.0	7.2	11.2	···	0.4	1
915	225.25230	-0.55593	1.1	···	···	1.31± 0.17	0.92± 0.05	0.47± 0.03	26.4	3.2	12.2	···	0.2	1
916	225.25284	-1.15143	0.8	0.34± 0.01	0.42± 0.03	1.31± 0.06	1.14± 0.01	0.69± 0.02	16.7	5.4	9.7	0.06	0.7	2
917	225.27676	-0.59287	1.1	···	···	0.86± 0.07	0.59± 0.01	0.36± 0.02	26.8	2.8	11.5	···	0.1	1
918	225.29135	-0.58120	1.1	···	···	5.40± 1.27	1.52± 0.06	1.31± 0.06	79.0	1.8	19.4	···	0.6	0
919	225.29695	-0.55935	1.1	···	···	0.84± 0.07	0.62± 0.01	0.32± 0.03	19.9	2.3	12.0	···	0.1	1
920	225.31511	-0.27625	1.1	···	···	0.57± 0.11	0.79± 0.01	0.49± 0.02	15.1	9.3	8.7	···	0.2	1
921	225.31541	-0.57747	1.1	···	···	0.65± 0.12	0.39± 0.01	0.17± 0.01	21.0	0.8	14.2	···	0.1	0
922	225.31949	-1.14295	0.8	···	···	0.99± 0.07	0.69± 0.02	0.41± 0.03	26.0	1.7	11.6	···	0.1	1
923	225.32629	-0.53244	1.1	16.54± 0.15	17.71± 0.25	14.84± 0.07	7.83± 0.02	2.82± 0.03	19.1	9.9	16.7	3.43	44.2	2
924	225.33392	-1.11957	0.8	···	···	0.77± 0.10	0.58± 0.03	0.51± 0.01	25.6	4.1	9.1	···	0.1	1

TABLE 3—*Continued*

ID	ℓ [°]	b [°]	d [kpc]	$F_{70} \pm \Delta F_{70}$ [Jy]	$F_{160} \pm \Delta F_{160}$ [Jy]	$F_{250} \pm \Delta F_{250}$ [Jy]	$F_{350} \pm \Delta F_{350}$ [Jy]	$F_{500} \pm \Delta F_{500}$ [Jy]	r [″]	M [$M_\odot$]	T [K]	F_{22} [Jy]	L_{bol} [$L_\odot$]	unbound/pre-/proto-stellar 0/1/2
925	225.34178	-1.07988	0.8	···	···	0.84± 0.06	0.75± 0.01	0.36± 0.03	23.9	1.9	11.1	···	0.1	1
926	225.34790	-0.27405	1.0	···	···	2.15± 0.10	2.04± 0.02	1.27± 0.03	29.9	11.7	10.0	···	0.4	1
927	225.36028	-0.20453	1.0	···	···	0.34± 0.05	0.24± 0.01	0.20± 0.01	15.1	1.5	10.1	···	0.1	1
928	225.36090	-0.40918	1.1	···	···	0.78± 0.18	0.98± 0.01	0.60± 0.02	23.7	10.4	9.1	···	0.2	1
929	225.36206	-0.22237	1.0	···	···	0.54± 0.10	0.36± 0.01	0.20± 0.02	22.1	1.1	12.0	···	0.1	0
930	225.39027	-0.25121	1.0	···	···	1.88± 37.70	1.63± 0.02	0.90± 0.03	40.8	6.6	10.8	···	0.3	1
931	225.39120	-0.98573	0.6	···	···	0.25± 0.05	0.34± 0.01	0.16± 0.01	12.0	0.6	9.6	···	0.0	1
932	225.39833	-1.02287	0.6	···	···	1.26± 0.06	1.06± 0.02	0.25± 0.05	22.9	0.2	17.0	···	0.1	0
933	225.40114	-0.56134	0.6	4.26± 0.08	4.61± 0.13	4.70± 0.20	2.61± 0.05	1.50± 0.01	15.3	2.1	14.2	0.19	3.1	2
934	225.41173	-0.35974	1.1	···	···	0.34± 0.06	0.44± 0.01	0.27± 0.01	17.9	4.7	9.1	···	0.1	1
935	225.42535	-0.31206	1.0	···	···	0.38± 0.18	0.60± 0.06	0.35± 0.02	20.2	5.8	8.6	···	0.1	1
936	225.43135	-0.39845	1.1	···	0.54± 0.07	1.25± 0.13	0.98± 0.01	0.61± 0.03	20.0	6.6	10.4	0.08	1.2	2
937	225.43605	-0.38709	1.1	···	···	0.89± 0.09	0.81± 0.02	0.66± 0.04	23.6	9.1	9.3	···	0.2	1
938	225.44194	-0.24260	1.0	···	···	0.79± 0.07	0.83± 0.01	0.62± 0.03	22.7	7.6	9.1	···	0.2	1
939	225.45551	-0.40621	1.1	···	···	0.85± 0.12	1.18± 0.01	0.77± 0.05	24.5	16.3	8.6	···	0.3	1
940	225.47861	-0.23307	1.0	···	···	2.50± 0.11	2.86± 0.01	1.40± 0.04	30.4	13.4	10.1	···	0.5	1
941	225.48128	-0.24487	1.0	···	···	1.44± 0.17	1.79± 0.01	1.33± 0.05	31.0	20.2	8.6	···	0.3	1
942	225.48631	-0.32224	1.1	···	···	0.77± 0.13	1.00± 0.01	0.67± 0.02	18.4	13.2	8.7	···	0.2	1
943	225.48694	-0.40187	1.1	···	···	1.07± 0.07	0.92± 0.01	0.47± 0.02	17.3	4.4	11.1	···	0.2	1

REFERENCES

Alves, J., Lombardi, M., & Lada, C. J. 2007, A&A, 462, L17

André, P., Ward-Thompson, D., & Barsony, M. 2000, Protostars and Planets IV, 59

André, P., Men'shchikov, A., Bontemps, S., et al. 2010, A&A, 518, L102

Bergin, E. A., & Tafalla, M. 2007, ARA&A, 45, 339

Bernard, J.-P., Paradis, D., Marshall, D. J., et al. 2010, A&A, 518, L88

Blitz, L., Fich, M., & Stark, A. A. 1982, ApJS, 49, 183

Bolatto, A. D., Leroy, A. K., Rosolowsky, E., Walter, F., & Blitz, L. 2008, ApJ, 686, 948

Bontemps, S., André, P., Könyves, V., et al. 2010, A&A, 518, L85

Brand, J., Cesaroni, R., Palla, F., & Molinari, S. 2001, A&A, 370, 230

Brunt, C. M., Kerton, C. R., & Pomerleau, C. 2003, ApJS, 144, 47

Brunthaler, A., Reid, M. J., Menten, K. M., et al. 2011, Astronomische Nachrichten, 332, 461

Burton, W. B., & te Lintel Hekkert, P. 1986, A&AS, 65, 427

Carlhoff, P., Nguyen Luong, Q., Schilke, P., & et al. submitted, A&A

Carraro, G., Vázquez, R. A., Moitinho, A., & Baume, G. 2005, ApJ, 630, L153

Chabrier, G. 2005, in Astrophysics and Space Science Library, Vol. 327, The Initial Mass Function 50 Years Later, ed. E. Corbelli, F. Palla, & H. Zinnecker, 41

Clariá, J. J. 1974, A&A, 37, 229

Cordes, J. M., & Lazio, T. J. W. 2002, ArXiv Astrophysics e-prints

Dame, T. M., Hartmann, D., & Thaddeus, P. 2001, ApJ, 547, 792

Dobashi, K., Uehara, H., Kandori, R., et al. 2005, PASJ, 57, 1

Egan, M. P., Shipman, R. F., Price, S. D., et al. 1998, ApJ, 494, L199

Elia, D., Massi, F., Strafella, F., et al. 2007, ApJ, 655, 316

Elia, D., Schisano, E., Molinari, S., et al. 2010, A&A, 518, L97

Enoch, M. L., Evans, II, N. J., Sargent, A. I., et al. 2008, ApJ, 684, 1240

Federrath, C., Glover, S. C. O., Klessen, R. S., & Schmidt, W. 2008, Physica Scripta Volume T, 132, 014025

Giannini, T., Elia, D., Lorenzetti, D., et al. 2012, A&A, 539, A156

Gregorio-Hetem, J., Montmerle, T., Rodrigues, C. V., et al. 2009, A&A, 506, 711

Griffin, M. J., Abergel, A., Abreu, A., et al. 2010, A&A, 518, L3

Hennemann, M., Motte, F., Bontemps, S., et al. 2010, A&A, 518, L84

Heyer, M. H., Brunt, C., Snell, R. L., et al. 1998, ApJS, 115, 241

Heyer, M. H., Williams, J. P., & Brunt, C. M. 2006, ApJ, 643, 956

Hildebrand, R. H. 1983, QJRAS, 24, 267

Hill, T., Motte, F., Didelon, P., et al. 2011, A&A, 533, A94

Ikeda, N., Sunada, K., & Kitamura, Y. 2007, ApJ, 665, 1194

Kainulainen, J., Beuther, H., Banerjee, R., Federrath, C., & Henning, T. 2011, A&A, 530, A64

Kauffmann, J., & Pillai, T. 2010, ApJ, 723, L7

Kim, B. G., Kawamura, A., Yonekura, Y., & Fukui, Y. 2004, PASJ, 56, 313

Klessen, R. S. 2000, ApJ, 535, 869

Könyves, V., André, P., Men'shchikov, A., et al. 2010, A&A, 518, L106

Kramer, C., Stutzki, J., Rohrig, R., & Corneliussen, U. 1998, A&A, 329, 249

Kroupa, P. 2001, MNRAS, 322, 231

Krumholz, M. R., & McKee, C. F. 2008, Nature, 451, 1082

Kutner, M. L., & Ulich, B. L. 1981, ApJ, 250, 341

Lada, C. J., Lombardi, M., & Alves, J. F. 2010, ApJ, 724, 687

Larson, R. B. 1981, MNRAS, 194, 809

Lee, Y., Snell, R. L., & Dickman, R. L. 1994, ApJ, 432, 167

Lynds, B. T. 1962, ApJS, 7, 1

Maddalena, R. J., Morris, M., Moscowitz, J., & Thaddeus, P. 1986, ApJ, 303, 375

May, J., Alvarez, H., & Bronfman, L. 1997, A&A, 327, 325

May, J., Bronfman, L., Alvarez, H., Murphy, D. C., & Thaddeus, P. 1993, A&AS, 99, 105

May, J., Murphy, D. C., & Thaddeus, P. 1988, A&AS, 73, 51

Megeath, S. T., Allgaier, E., Young, E., et al. 2009, AJ, 137, 4072

Miyazaki, A., & Tsuboi, M. 2000, ApJ, 536, 357

Mizuno, A., & Fukui, Y. 2004, in Astronomical Society of the Pacific Conference Series, Vol. 317, Milky Way Surveys: The Structure and Evolution of our Galaxy, ed. D. Clemens, R. Shah, & T. Brainerd, 59

Moitinho, A., Vázquez, R. A., Carraro, G., et al. 2006, MNRAS, 368, L77

Molinari, S., Pezzuto, S., Cesaroni, R., et al. 2008, A&A, 481, 345

Molinari, S., Schisano, E., Faustini, F., et al. 2011, A&A, 530, A133

Molinari, S., Swinyard, B., Bally, J., et al. 2010a, A&A, 518, L100

—. 2010b, PASP, 122, 314

Motte, F., & André, P. 2001, A&A, 365, 440

Motte, F., Zavagno, A., Bontemps, S., et al. 2010, A&A, 518, L77

Murray, N. 2011, ApJ, 729, 133

Nakanishi, H., & Sofue, Y. 2006, PASJ, 58, 847

Ogawa, H., Mizuno, A., Ishikawa, H., Fukui, Y., & Hoko, H. 1990, International Journal of Infrared and Millimeter Waves, 11, 717

Olmi, L., Anglés-Alcázar, D., De Luca, M., et al. 2010, ApJ, 723, 1065

Olmi, L., Anglés-Alcázar, D., Elia, D., et al. 2013, A&A, 551, A111

Ott, S. 2010, in Astronomical Society of the Pacific Conference Series, Vol. 434, Astronomical Data Analysis Software and Systems XIX, ed. Y. Mizumoto, K.-I. Morita, & M. Ohishi, 139

Piazzo, L., Ikhenaode, D., Natoli, P., et al. 2012, Image Processing, IEEE Transactions on, 21, 3687

Pilbratt, G. L., Riedinger, J. R., Passvogel, T., et al. 2010, A&A, 518, L1

Pineda, J. E., Caselli, P., & Goodman, A. A. 2008, ApJ, 679, 481

Poglitsch, A., Waelkens, C., Geis, N., et al. 2010, A&A, 518, L2

Preibisch, T., Ossenkopf, V., Yorke, H. W., & Henning, T. 1993, A&A, 279, 577

Reid, M. J., Menten, K. M., Zheng, X. W., et al. 2009, ApJ, 700, 137

Reipurth, B., & Yan, C.-H. 2008, Star Formation and Molecular Clouds towards the Galactic Anti-Center, ed. B. Reipurth, 869

Rosolowsky, E., & Blitz, L. 2005, ApJ, 623, 826

Rosolowsky, E., & Leroy, A. 2006, PASP, 118, 590

Rosolowsky, E., & Leroy, A. 2011, in Astrophysics Source Code Library, record ascl:1102.012, 2012

Ruprecht, J. 1966, IAU Trans. XIIB, 348

Russeil, D., Pestalozzi, M., Mottram, J. C., et al. 2011, A&A, 526, A151

Sadavoy, S. I., di Francesco, J., André, P., et al. 2012, A&A, 540, A10

Saraceno, P., Andre, P., Ceccarelli, C., Griffin, M., & Molinari, S. 1996, A&A, 309, 827

Schneider, N., Csengeri, T., Hennemann, M., et al. 2012, A&A, 540, L11

Sharpless, S. 1959, ApJS, 4, 257

Shetty, R., Glover, S. C., Dullemond, C. P., & Klessen, R. S. 2011, MNRAS, 412, 1686

Simon, R., Jackson, J. M., Clemens, D. P., Bania, T. M., & Heyer, M. H. 2001, ApJ, 551, 747

Solomon, P. M., Downes, D., & Radford, S. J. E. 1992, ApJ, 398, L29

Solomon, P. M., Rivolo, A. R., Barrett, J., & Yahil, A. 1987, ApJ, 319, 730

Tegmark, M. 1997, ApJ, 480, L87

Traficante, A., Calzoletti, L., Veneziani, M., et al. 2011, MNRAS, 416, 2932

Vallée, J. P. 2005, AJ, 130, 569

Vázquez, R. A., May, J., Carraro, G., et al. 2008, ApJ, 672, 930

Veneziani, M., Elia, D., Noriega-Crespo, A., et al. 2013, A&A, 549, A130

Williams, J. P., de Geus, E. J., & Blitz, L. 1994, ApJ, 428, 693

Wouterloot, J. G. A., Brand, J., Burton, W. B., & Kwee, K. K. 1990, A&A, 230, 21

Wright, E. L., Eisenhardt, P. R. M., Mainzer, A. K., et al. 2010, AJ, 140, 1868

Xu, Y., Voronkov, M. A., Pandian, J. D., et al. 2009, A&A, 507, 1117

Yun, J. L., Elia, D., Palmeirim, P. M., Gomes, J. I., & Martins, A. M. 2009, A&A, 500, 833

This 2-column preprint was prepared with the AAS LaTeX macros v5.2.